Università degli Studi di Padova

DIPARTIMENTO DI FISICA E ASTRONOMIA 'GALILEO GALILEI'
Corso di Laurea Magistrale in Fisica

Analisi della pulsar del Granchio ad elevata risoluzione temporale nella banda ottica: studio del ritardo con l'emissione radio

Relatore:
Prof. Luca Zampieri

Laureando:
Giovanni Ceribella

Anno Accademico 2014–2015

A Giacomo,
tra le stelle.

Riassunto

In questo lavoro di tesi si è determinata, attraverso delle osservazioni ottiche ad alta risoluzione temporale, la curva di fase della pulsar del Granchio (PSR B0531+21), nel periodo compreso tra gennaio e ottobre 2012. I dati nella banda visibile sono stati acquisiti a Cima Ekar (Asiago, VI) con lo strumento AQUEYE montato sul telescopio 'Copernico' da 182 cm di diametro dell'INAF Osservatorio Astronomico di Padova. AQUEYE è un contatore di fotoni veloce in grado di rilevare eventi di singolo fotone e di caratterizzare i tempi di arrivo con un'accuratezza temporale di qualche centinaio di picosecondi [1]. Le effemeridi ottiche ottenute sono state confrontate con quelle nella banda radio pubblicate mensilmente dal Jodrell Bank Observatory (Università di Manchester). Si evidenza un ritardo dell'emissione radio rispetto a quella ottica di circa 200 μs: ciò fornisce delle informazioni sulla geometria della regione di emissione della pulsar e può porre un limite ai modelli che tentano di descriverne il meccanismo.

In parallelo all'attività di analisi dei dati, si è preso parte attivamente a delle osservazioni svolte nei periodi di marzo 2013, maggio 2014 e gennaio 2015. Tale attività ha già fornito dei risultati preliminari, pubblicati in [2] e [3].

Nel Capitolo primo, si introducono gli aspetti fondamentali della Fisica delle Stelle di Neutroni e dell'osservazione delle Pulsar. Il capitolo secondo fornisce informazioni su AQUEYE e sulla strumentazione impiegata. Il terzo capitolo illustra i metodi utilizzati nell'analisi dei dati, mentre il quarto presenta i risultati ottenuti. Le possibili implicazioni sono discusse nel capitolo conclusivo.

Abstract

This thesis aims to determine the timing solution for the Crab pulsar (PSR B0531+21) in the period from January to October 2012, using high time resolution optical observations. Optical data have been acquired at Cima Ekar (Asiago, VI) with the AQUEYE instrument at the 182 cm 'Copernico' telescope of the INAF Osservatorio Astronomico di Padova. AQUEYE is a fast photon counter which is able to detect single-photon events and time tag them with an accuracy of a few hundred picoseconds [1]. Pulsar's timing ephemerides at visible wavelengths were produced and compared to the radio ones, published by the Jodrell Bank Observatory (University of Manchester). The radio emission was found to lag by 200 μs the optical one: this gives information upon the emitting region's geometry and may pose constrains on pulsar's emission models.

At the same time, I took part in analogous observations on March 2013, May 2014 and January 2015. Preliminary results of these activities were published in [2] and [3].

In the first chapter of this work, fundamentals of Neutron Star Physics and Pulsar observation are introduced. The second chapter gives information on the AQUEYE detector and instrumentation used in the observations. The third chapter describes data analysis methods, while the fourth presents our final results. Possible implications are discussed in the final chapter.

Contents

Chapter 1

Pulsars

Pulsars are a kind of astronomical source exibiting beacon-like behaviour. They are revealed mainly in the radio domain of the electromagnetic spectrum, but few of them are known to have a visible emission too. After their discovery in 1967, it soon became clear that such a phenomenon could be associated with the existence of *Neutron Stars*, a compact celestial body characterized by very high densities. A complete description of Neutron Star Physics is yet to be reached, requiring the understanding of different and diverse physical phenomena and of their interaction. Neutron stars masses are comparable to that of the Sun, packed in a 10 km radius. Since the Schwarzschild radius for a $1\,\mathrm{M}_\odot$ body is $\simeq 3\,\mathrm{km}$, the gravity of such an object is extremely strong and has to be modelled through General Relativity. Average densities are of the order of the nuclear density ($10^{17}\,\mathrm{kg/m^3}$) and thus both Strong and Weak Interactions have to be accounted to explain the inner structure. Finally, neutron stars have very intense magnetic fields ($B > 10^8\,\mathrm{T}$) which produce an extended plasma Magnetosphere, which ought to be described by Magnetohydrodynamics.

This chapter will introduce some basic concepts of pulsar Physics. To do so, we start with a common description of Degenerate Stars, which is applicable also to the case of White Dwarfs. Later sections present concepts which are related to the observation of pulsars.

1.1 Degenerate Stars

Normal stars support their own gravitational attraction by the power of nuclear fusion reactions taking place in their core. To compute the structure of such stars, a general approach is to write down a *hydrostatic equilibrium* equation[1], which relates the pressure

---

[1] This is usually not sufficient to model stellar envelopes in depth. Some stars, particularly supergiant ones, exibit vaste matter motions in the form of convection. Modelling these features requires a more general Hydrodynamical approach with the inclusion of a thermonuclear reaction network, which can be solved only numerically.

mantained by thermonuclear reactions to the strenght of the gravitational field:

$$\frac{Gm(r)}{r^2} + \frac{1}{\rho(r)}\frac{dP(r)}{dr} = 0 \tag{1.1}$$

As thermonuclear reactions energy outcome varies throughout the star's history, the pressure term in 1.1 varies too and the gravitational term reacts untill a new equilibrium is reached. During the last stages of stellar evolution, fusion reactions eventually stop: gravity is no more balanced by any pressure, the stellar core contract and eventually collapses.

The collapse squeezes the stellar plasma to very high densities and may be halted only if a new source of pressure is found. After the white dwarfs' discovery, this source has been identified in the *degeneracy pressure*, which arises from the fermionic nature of either electrons (for white dwarfs) or neutrons (for neutron stars), for which the Pauli exclusion principle holds.

In Quantum Mechanics, this property is derived from the complete antisymmetric behaviour of many identical fermions states $|\psi\rangle$ under the exchange of any two particles [4]. The many-particle state $|\psi\rangle$ can be derived from single particle states $|\phi^0\rangle \ldots |\phi^N\rangle$ with the aid of a Slater determinat: this approach shows that if any two particle are in the same state $|\phi^i\rangle$ the corresponding $|\psi\rangle$ is zero, i.e. fermionic single-particle states may be unoccupied or occupied by one particle at most. Because of this, in the ground state fermions arrange and occupy states following a bottom-up energy aufbau, with the highest reached energy E_F being named the Fermi energy and corresponding to a Fermi momentum p_F. This property give rise to *non-vanishing ground state pressure*: for such a phenomenon to become relevant, either the temperature has to be very low or the density has to be very high. During the core collapse of a star such high densities are indeed reached: if the progenitor star has a low-mass, this leads to the formation of a white dwarf, a star renmant in which the supporting pressure in 1.1 is supplied by the degeneracy of *electrons* (see Figure 1.2); on the other hand, if the mass of the star is higher a Neutron Star can form, in which supporting fermions are *neutrons*. Finally, if the initial mass is even higher the collapse cannot be stopped and a Black Hole forms.

The dependance of collapse's outcome upon initial mass is caused by several factors, including the relativistic or non-relativistic behaviour of different fermionic species at a certain density ρ. By comparing the star's self-gravitational energy and the average kinetic energy of degenerate fermions, it can be shown that, if fermions are non-relativistic (i.e. $x = p_F/mc \ll 1$), there is always an energy minimum corresponding to a stable equilibrium, i.e. a solution to 1.1. However, it turns out that extremely relativistic fermions cannot grant an energy minimum and a stable hydrostatic equilibrium. As the mass of the star is increased, higher degeneracy pressure would be required to balance gravity, corresponding to higher p_F and x. Over a certain mass limit $\mathcal{M}$ fermions behave like ultra-relativistic particles and no equilibrium can be found. The degeneracy

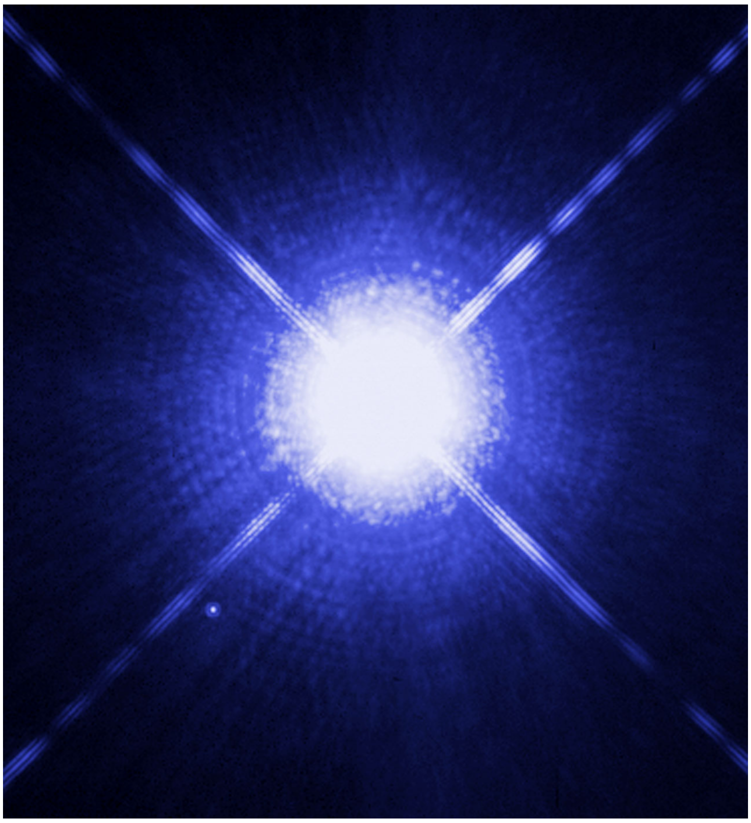

Figure 1.1: Sirius B, the small dot at the bottom-left in the image, is a white dwarf and was among the first discovered degenerate stars. Its mass was first understood to be close to the solar one by observing the fluctuations in the proper motion of Sirius A (big star in the middle). Being the distance of the system known, from apparent luminosity and color an estimate of the star's dimension can be derived: this gives a 12000 km diameter, similar to the terrestrial one. The average density must then be $\rho = 3/4\pi M_\odot/R^3 \simeq 2 \cdot 10^9\,\mathrm{kg/m^3}$. Such high densities can't be supported by ordinary matter, and are proper of degenerate matter. The image, taken by the HST, is 15″ wide. Credit: *NASA, ESA, H. Bond (STScI), and M. Barstow (University of Leicester)*

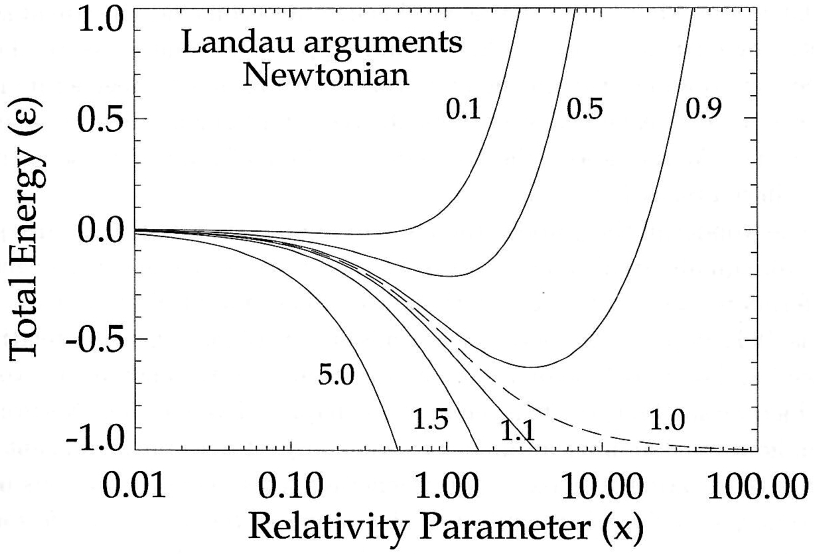

Figure 1.2: Total energy per fermion for a degenerate star, in the uniform-density and classical-gravity approximation (Landau argument). Different curves refer to different white dwarf masses and are labeled by their $M/\mathcal{M}_C$ value. While $M < \mathcal{M}_C$, a minimum energy (stable equilibrium) exists, which moves towards higher relativity parameters x (equivalently to higher densities and pressures) as the mass increases. At the Chandrasekar limit (dashed curve), relativistic electrons cannot provide any energetic minimum: the negative slope of the curve indicates that the system runs to higher and higher relativity parameter x, corresponding to arbitrary high densities: it is the white dwarf's collapse. The figure is from P. Ghosh, *"Rotation and Accretion Powered Pulsars"*, [5].

pressure of these fermions is not able to balance gravity and the collapse goes further.[2] As a result, white dwarfs, which are supported by the electronic degeneracy pressure at average densities of $\rho_{NB} = 10^8\,\mathrm{kg/m^3}$, have an upper mass limit $\mathcal{M}_C = 1.4\,M_\odot$, the Chandrasekar limit. If the collapsing core of a giant star exceedes this limit, or if an already formed white dwarf accretes material and gets over it, electrons cannot supply the pressure to stop the collapse and matter is compressed to even higher densities.

During the collapse of the core of a massive star and depending upon its composition, a critical density $\rho_n = 10^{12} - 10^{13}\,\mathrm{kg/m^3}$ is found at which it becomes energetically favourable for protons and electrons to form neutrons. These phenomena are governed by the Weak Interaction, which drives β processes:

$$\mathrm{n} \;\rightarrow\; \mathrm{p} + \mathrm{e}^- + \bar{\nu}_\mathrm{e} \tag{1.2}$$

$$\mathrm{p} + \mathrm{e}^- \;\rightarrow\; \mathrm{n} + \nu_\mathrm{e} \tag{1.3}$$

The second process (electron capture) may happen at first when the electron's energy

---

[2] A similar argument was first used by Landau within a spherical and uniform density model to derive a limit on white dwarfs' mass, which turned out to be $1.72\,M_\odot$. Later Chandrasekar works, using a more realistic *polytropic* approximation gave the well-known $1.4\,M_\odot$ value.

equals the mass difference between proton and neutron[3], i.e. when $p_\beta = c(\Delta m^2 - m_e^2)^{1/2} \simeq 1.18\,\mathrm{MeV/c}$. This corresponds to a relativistic electron with $x_\beta \simeq 2.3$. On the other hand, the first reaction (β decay) is spontaneous, provided that there is room in the phase space to emit an electron: in a degenerate electron gas, if the Fermi momenum gets over p_β, the β decay process is blocked. This contributes in shifting the equilibrium of β reactions towards neutrons. Since very high densities and hence very high p_F are reached while collapsing, matter undergoes a neutronization process and it is transformed in a bulk of neutrons. Neutrons are much more massive fermions than electrons; hence their degeneracy pressure is capable of supporting much higher gravitational attraction at higher density. The collapse eventually stops and a Neutron Star is formed.

The above stability discussion might be repeated again for neutron stars, hence deriving a neutron-relativistic limit on neutron star masses. In reality a neutron star requires a much more in-depth approach, both because of its general-relativistic character and the complex (and poorly understood) interacitons of neutronized matter. As a result the upper limit $\mathcal{M}_{OV}$ to neutron stars' masses, named after Oppenheimer and Volkov, is at $\simeq 3\,\mathrm{M}_\odot$, while neutrons are still non-relativistic. A great effort has been devoted to describe the neutronized matter Equation of State, i.e. the $P(\rho, T)$ relation inside the Neutron Star. Since the point is still debated, high-resulotion pulsar observations may be useful for understanding the physics of these objects.

Accurate calculations of the Neutron Star Equation of State give in most cases maximum mass upper limits in the range $2.2 - 2.5\,\mathrm{M}_\odot$ [6]. Nowadays, the largest measured Neutron Star masses are those of pulsar PSR J1614-2230, $1.97 \pm 0.04\,\mathrm{M}_\odot$ [7] and PSR J348+0433, $2.01 \pm 0.04\,\mathrm{M}_\odot$, [8].

1.1.1 Mass-radius relation

An estimate of the mass-radius relation for degenerate stars can be derived by assuming that the star is simply a uniform-density sphere. With this rough hypotesis one can compute typical white dwarf and neutron star parameters:

	M	ρ	n	μ	R
WD	$1.0\,\mathrm{M}_\odot$	$10^8\,\mathrm{kg/m^3}$	$10^{34}\,\mathrm{m^{-3}}$	1/2	$7 \cdot 10^3\,\mathrm{km}$
NS	$1.5\,\mathrm{M}_\odot$	$10^{17}\,\mathrm{kg/m^3}$	$10^{43}\,\mathrm{m^{-3}}$	1	$10\,\mathrm{km}$

Table 1.1: Typical White Dwarf and Neutron Star parameters. Mass M, density ρ, fermionic number density n, fermions per nucleon μ, radius R.

---

[3] The tiny neutrino mass is ignored. Also, since the barycenter of the electron+proton system is essentialy coincident with the proton, we can assume that both the proton and the final neutron are at rest.

1.2 Neutron star properties

1.2.1 Internal structure

Models of Neutron Star's inner structure depend on the equation of state of neutronized matter, which is still not well known. Present models predict a stratified structure, made of layers:

1. An *Outer Crust*, ($h \simeq 300\,\mathrm{m}$) made of a crystalline reticule of atomic nuclei embedded in an electron see. Densities are belived to range from terrestrial ones up to $\rho_{drip} = 4 \cdot 10^{14}\,\mathrm{kg/m^3}$. The surface should mostly consist of $^{56}\mathrm{Fe}$, but atomic species vary with depth because high densities shift the Weak Interaction equilibrium towards neutron-rich nuclides.

2. An *Inner Crust*, ($h \simeq 700\,\mathrm{m}$) ranging from $\rho_{drip} = 4 \cdot 10^{14}\,\mathrm{kg/m^3}$ to the nuclear density $\rho_{nucl.} = 3 \cdot 10^{17}\,\mathrm{kg/m^3}$. At ρ_{drip} it becomes energetically favourable for weak interactions to produce free rather than bound neutrons (i.e. the neutrons' chemical potential μ_n equals the neutron mass $m_\mathrm{n}c^2$). This phenomenon is known as "neutron drip". As a result, matter in the inner crust consist of highly neutronized nuclei surrounded by a continuum of neutrons, further immersed in an electron see. It has been speculated that at the lower edge of this zone nuclei with bizarre shapes could be present (plates and rods structures). The crust as a whole is believed to contain a mere 1% of the neutron star's mass.

3. An *Outer Core*, ($\simeq 10\,\mathrm{km}$) where densities are comparable or higher than the nuclear density $\rho_{nucl.}$. This enables Strong Interaction to play a significat role: matter is thought to be in an almost completely neutronized superfluid state.

4. An *Inner Core*, whose composition and size is unknown. It is thought that exotic matter might occur in it. This might come in the form of mesons condensates and/or quark continuum. Recent (July 2015) pentaquark evidence at CERN's LHCb experiment [9] may shed new light on this exotic matter states.

1.2.2 Rotation

Being the final result of a stellar core collapse, neutron stars have very high rotation frequencies. Typical periods range from 1 ms (joung and recycled pulsars, see later) to few seconds (oldest neutron stars). The neutron star loses part of its rotational energy during time, as it will be discussed in the next sections. Rotation can be directly studied when the neutron star is detectable as a pulsar and constitutes the primary way through which information on neutron stars is obtained. More details are given in Section 1.3

1.2.3 Magnetic Field and Magnetosphere

Neutron stars host extremely intense magnetic fields, typical intensities[4] at the star's surface being $B = 10^8$ T. Such high values arise during the formation of the neutron star. The material which the progenitor is made of has a very high electrical conducibility σ. In these conditions a fundamental theorem of Plasma Physics, the *Alfvén Theorem*, states that *the magnetic flux Φ_B across a closed circuit C which moves with the medium is constant* [10]. Let us consider a circuit which lays on the progenitor's surface and is perpendicular to its magnetic axis (a sort of "magnetic equator"). During the collapse, the radius of the circuit shrinks from the initial R_* value to a typical neutron star radius $R_{NS} = 10\,\text{km}$; since the magnetic flux which crosses its surface has to be constant, the magnetic field B_{NS} is roughly determined by:

$$B_{NS}\,R_{NS}^2 = B_*\,R_*^2 \tag{1.4}$$

$$B_{NS} = \left(\frac{R_*}{10\,\text{km}}\right)^2 B_* \tag{1.5}$$

We can use the above equation to compute the field resulting from, say, a progenitor stellar core with $R_* = 10000\,\text{km}$ and $B_* = 100\,\text{T}$. Equation 1.5 gives then $B_{NS} = 10^8$ T.

Electromagnetic braking

Suppose that the neutron star's magnetic field were purely dipolar, so that the magnetic moment μ of the neutron star were misaligned with its rotation axis (as in Figure 1.3) [11], [12], [13]. Because of the star's rotation, a distant observer would detect an oscillating magnetic moment, by which energy is dissipated in the form of electromagnetic radiation. The emitted power can be calculated by using classical varying magnetic dipole far field solutions:

$$\dot{\mathcal{E}} = \frac{2\mu^2\omega^4\sin^2(\alpha)}{3c^3} \tag{1.6}$$

Where ω is the rotational pulsation and α is the misalignment angle. The neutron star thus emits power through electromagnetic radiation. If we suppose energy to be supplied by the neutron stars's rotation, a relation between the pulsation ω and its first derivative can be found:

$$-\dot{\mathcal{E}} = \cancel{\frac{1}{2}\dot{\mathcal{I}}}\omega^2 + \mathcal{I}\omega\dot{\omega} \tag{1.7}$$

$$\dot{\omega} = -\frac{2\mu^2\sin^2(\alpha)}{3\mathcal{I}c^3}\omega^3 \tag{1.8}$$

Where we made use of the fact that the variation of the Neutron Star's moment of inertia $\mathcal{I}$ is usually considered negligible. Equation 1.8 states that a rotational slowdown is rather to be expected. This effect can be studied throughout pulsar observations, and constitutes a major topic of this reseach field. Further details are given in Section 1.3.

---

[4] Some young peculiar Neutron stars, called Magnetars, can reach up to $B = 10^{11}$ T due to dynamos effect in the superfluid core.

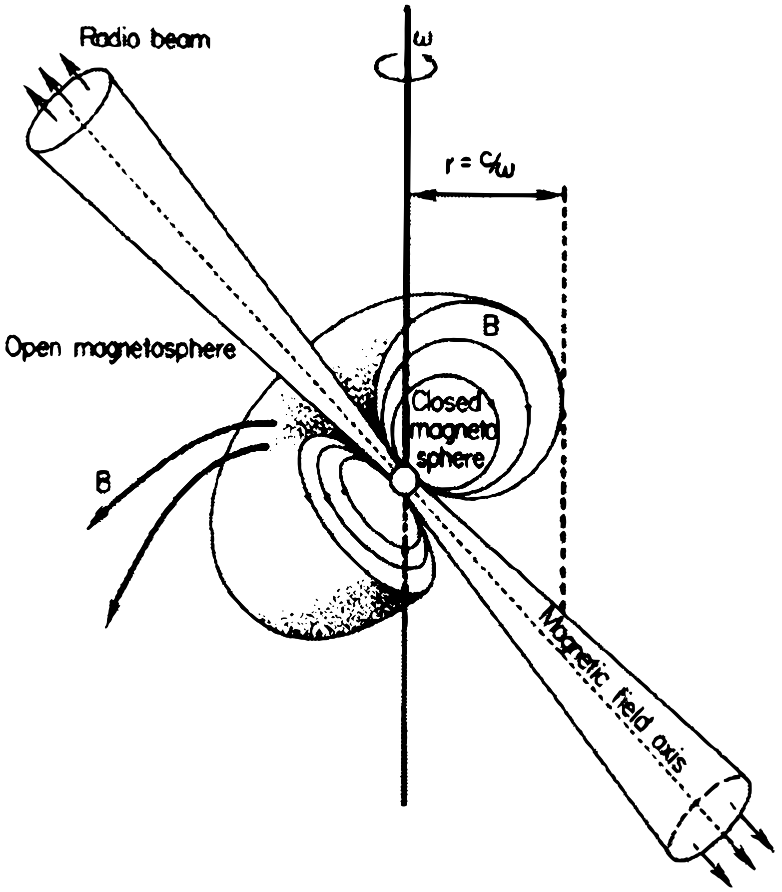

Figure 1.3: Scheme of a Pulsar and of its magnetosphere. The pulsar and its magnetic field rotate around the vertical axis. The magnetic moment is not aligned with the rotation axis. The magnetosphere's plasma is forced to co-rotate with the magnetic field, but as radius increases over $r_L = c/\omega$ (light cilinder) this becomes impossible: the magnetosphere is divided in a closed region at $r \leq r_L$ with closed field lines, and in an open region (radiative fields) which extends beyond r_L. Credit: *IEEE*.

Magnetosphere

The intense magnetic fields just at the surface of a neutron star produce a vaste plasma magnetosphere in the star's surroundings [14]. Being neutron star's matter effectively infinitely conducting ($\sigma \to \infty$), in an equilibrium configuration no charge inside it may experience a net electromagnetic force[5]. As a result, the Lorentz force should be everywhere null inside the star:

$$\vec{E} + \vec{v} \times \vec{B} = 0 \tag{1.9}$$

By using the relation $\vec{v} = \vec{\omega} \times \vec{r}$ one finds:

$$\vec{E} + (\vec{\omega} \times \vec{r}) \times \vec{B} = 0 \tag{1.10}$$

Since the magnetic filed is not null inside the star, the last relation predicts the existence of an electric field inside the star, which depends both on the magnetic field and on star's velocity. By working out equation 1.10 with a dipolar magnetic field $\vec{B}$ and further assuming $\vec{\omega} \parallel \vec{\mu_B}$, one can derive the expression for the electric field just *outside* the neutron star surface, which is found to be *quadrupolar*. Such field has a component $E_{||}$ parallel to the local magnetic field, which is found to be:

$$E_{||} = -2\omega R B_0 \left(\frac{R}{r}\right)^4 \frac{\cos^3(\theta)}{\sqrt{3\cos^2(\theta) + 1}} \tag{1.11}$$

Where B_0 is the magnetic field modulus at either of the neutron star's poles. At the surface just over a pole, the above reduces to:

$$E_{||} = -\omega R B_0 \tag{1.12}$$

By using typical values, one finds $E_{||} \simeq 10^{13}$ V/m. This gives a force on a free electron or proton at the pole which is much greater than the gravitational attraction of the pulsar. As a result, charges are pulled off the surface and form a vaste magnetosphere in which the neutron star is embedded.

Figure 1.3 shows a scheme of a pulsar magnetosphere: the highly conducting plasma is forced to flow along the magnetic field lines, which corotate with the neutron star at pulsation ω. Usually, magnetic field lines rise from a pole and close themselves at the opposite one. However, it exists a radius r_L at which corotation implies a linear velocity $r_L\omega$ equal to the speed of light c. At this distance, the field lines cannot corotate any more with the star and break apart forming *open* magnetic field lines (radiative fields). The plasma flowing along these lines is accelerated up to relativistic velocities (pulsar wind) and ultimately is injected into the pulsar nebula. The region at $r \leq r_L = c/\omega$ is named *light cilinder* of the neutron star.

The argument just scketched stresses that, even for a $\vec{\omega} \parallel \vec{B}$ neutron star, i.e. a *aligned*

---

[5] This is analogous to what happens inside conductors in Elettrostatics.

rotator, these is a form of electromagnetic energy loss. By calculating the power emission associated with the open magnetosphere of an aligned rotator one finds a relation much similar to 1.6 and 1.8, with the same $\dot{\omega} \propto \omega^3$ scaling. In a real neutron star, both effects (misalignment dipole radiation and open magnetic field lines) are thought to contribute to the rotational braking.

1.3 Pulsars Observation

In the previous section, it was assumed that the power radiated by a neutron star is supplied by its rotational energy. This fact is true for a class of objects known as *Rotation powered Pulsars*. A second class, *Accretion powered Pulsars*, are thought to be supported by the gravitational energy of matter being accreted and ultimately falling on the star. Pulsars are a detectable manifestation of neutron stars. Most of them are revealed as radio sources, the signature being an extremely regular short-period signal. This feature is interpreted as generated by the periodic facing towards Earth of a fast spinning neutron star's magnetic pole. As discussed in the previous section, at the poles of such an object the electromagnetic field has enormous intensities: it is thought that an intense and collimated radiation beam emerges from these regions, thus producing a rather sharp increase in radio brightness (see Figure 1.3). Such hypotesis is supported by the signal's polarization signature, which fits very well with predictions by a misaligned rotator model [15].

Depending on the line of sight and on the degree of magnetic and rotation axes misalignment, the shape of the periodic signal, or the pulsar's *pulse* for short, varies too. An almost perfectly aligned rotator would show little or no pulse intensity variation during a cycle; on the other hand, a highly misaligned one viewed from a direction perpendicular to the rotation axis would exibit a significant flux variation during a cycle, the maximum being when a magnetic pole points towards Earth (see Figure 1.4). A variety of different pulse profiles exist, and early pulsar classifications were largely based on their morphology. Finally, a few pulsars are known to have counterparts and show pulsations in the optical band [16]: these are named *Optical Pulsars* and are listed in Table 1.2.

Pulsar	B mag.	Pulsar	B mag.
Crab	17	Geminga	25.5
PSR 0540-69	23	PSR 0656+14	26
Vela	24	PSR 1509-58	25.7

Table 1.2: List of optical pulsars, as from [16]. A more complete list can be find in [17].

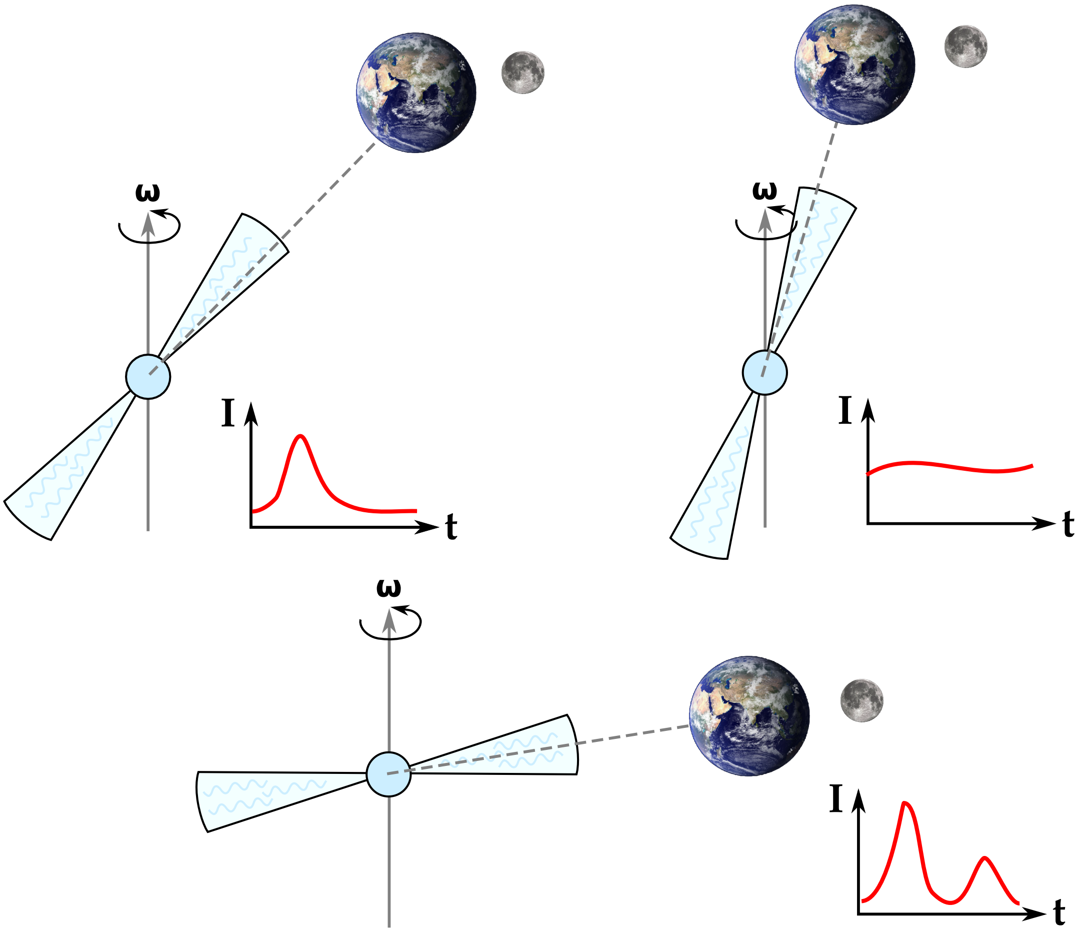

Figure 1.4: Pulsar-Earth alignment, as well as magnetic and rotation axes misalignment determine the pulse shape. The image at the bottom resembles the actual Crab pulsar's configuration.

1.3.1 Timing and Braking Index

By measuring the signal's period T, one effectively determinates the neutron star's rotation period and possibly, its variation. This enables us to use before mentioned formulae for the pulsar's slowdown to estimate the neutron star's physical parameters, such as R, B, etc. Typical orders of magnitude given at the beginning of this chapter reflect average values computed in this way. The study of the periodic signal of pulsars, or *pulsar timing*, is the main way to obtain information on these objects and their Physics.

Equation 1.8, which characterizes the electromagnetic braking of the pulsar's rotation for an oblique electromagnetic dipole rotator in vacuum, predicts $\dot{\omega} = -k\omega^3$. This expression can be generalized for any exponent n on the right-hand side, obtaining a general scaling law:

$$\dot{\omega} = -k\omega^n \tag{1.13}$$

The exponent n is called the pulsar's *braking index* and is usually characteristic for each pulsar [18]. Different emission mechanisms give rise to different braking indices; for instance, the already quoted electromagnetic braking has $n = 3$, while braking due to gravitational waves emission would bring to $n = 5$ and relativistic particles emission would give $n = 1$ [19]. Upon differenciating 1.13, one finds:

$$\begin{aligned} n &= \frac{\ddot{\omega}\omega}{\dot{\omega}^2} = \frac{\ddot{\nu}\nu}{\dot{\nu}^2} \qquad (1.14) \\ &= 2 - \frac{T\ddot{T}}{\dot{T}^2} \qquad (1.15) \end{aligned}$$

Thus the rotational frequency of a pulsar and at least its first and second derivative have to be known to measure the braking index and hence get information on the pulsar braking mechanism.

Pulsar Evolution

By plotting the pulsar period derivative $\dot{T}$ versus the pulsar period T for different pulsars, a $T\dot{T}$ diagram (also called $P\dot{P}$) can be obtained. This diagram proved to be a sort of pulsar analogue of the Herzprung-Russel diagram for Stellar evolution. Figure 1.5 shows a log-log version of the diagram: while single dots represent values from single pulsars, encircled dots represent values from pulsars which are in a binary system. Shown are also costant magnetic field lines (negative slope) and constant characteristic age lines (defined later, positive slope). Two pulsar populations can clearly be identified: a first broad distribution at relatively high periods (0.1 – 1 s) and high B fields and spindown rates, mainly made of single pulsars; a second distribution at very short periods ($\simeq$ 1 ms) and low B fields and slowdown rates, whose constituents are primarily binary pulsars. The first one is interpreted as made by young rotational powered pulsars (high magnetic fields, high spindown rate, low

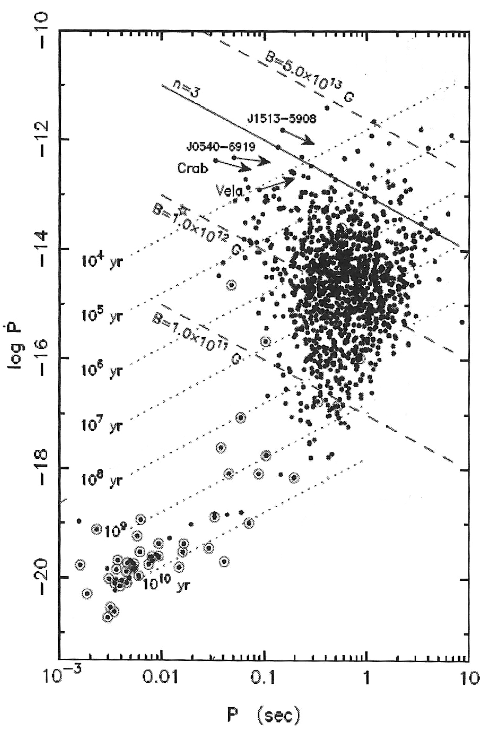

Figure 1.5: $P\dot{P}$ diagram. See text for details. Adapted from: *Tauris and Van den Huevel (2006), Cambridge Univeristy Press.*

characteristic age). The second population is thought to be composed by older pulsars with low magnetic fields, which underwent an accretion phase, gaining angular moment from a companion star (recycled pulsars). This gives a hint on a typical pulsar evolution: pulsars function as Rotation powered Pulsars in their early evolution stages, radiating waves at the expense of rotational energy. As time goes on, their megnetic field and spindown rate lower. However, if the pulsar is part of a binary system, material may be accreted from the companion, once its evolution brought it to the giant stage. Part of the accreting material's energy is radiated away (Accretion powered Pulsar), and part spins up the pulsar again. Once the process has ended, the pulsar rotates very fast but still has low magnetic field and slowdown rate, joining the second distribution in the $P\dot{P}$ diagram.

A simple tool to estimate the pulsar age can be derived from Equation 1.13. By separating variables and integrating it, one finds:

$$\frac{\omega^{1-n} - \omega_0^{1-n}}{n-1} = k\,(t - t_0) \tag{1.16}$$

Where ω_0 is the pulsar rotation at its formation time t_0. Since for young rotation powered pulsar $\omega_0 \gg \omega$, one can neclect it in the above expression ($1 - n$ is negative); by further using $k = -\dot{\omega}/\omega^n$, one finds:

$$t_{ch.} = t - t_0 = \frac{\omega}{\dot{\omega}(n-1)} \tag{1.17}$$

Equation 1.17 defines the characteristic age of a (rotational-powered) pulsar. Values range from 10^3 y (Crab Pulsar) to 10^8 y (older pulsars). Since the age of the Crab Pulsar is accurately known, formula 1.17 can be checked for consistency: the calculated value ($\simeq 1200$ y) is in reasonable agreement with the actual one ($\simeq 961$ y, as of 2015).

1.3.2 Timing irregularities

The timing of a pulsar, that is the evolution of its rotational properties, is not always regular. Sources of timing noise are present, and major events producing vaste irregularities might also take place. These events are called *Glitches* and consist in a sudden spinup of the pulsar, followed by a relaxation period during which the period T returns to values similar to the pre-glitch phase. The timescale of the relaxation period varies among pulsars, and can reach up to $\simeq 100$ d. During a glitch, the period first derivative $\dot{T}$ usually exibit sudden variations too. These phenomena are tought to be caused by interactions between the pulsar crust and the underlying superfluid core, their causes being still debated. While studying a pulsar, it is important to know if it recently had glitches, since its timing solution is likely going to be affected by it.

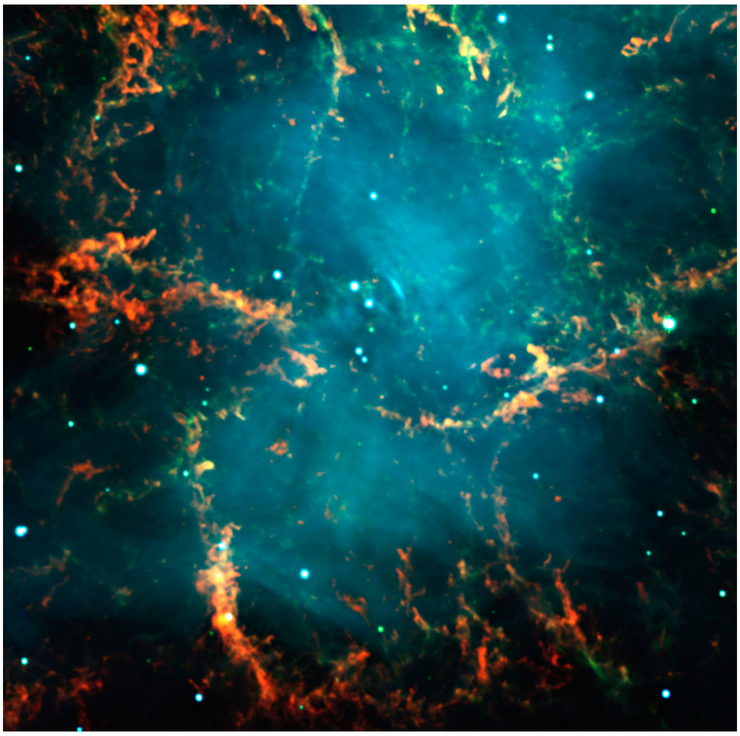

Figure 1.6: The Crab Pulsar, the object studied in this work, is a Neutron Star embedded in the Crab Nebula supernova renmant. The pulsar is the bright source up-center in the image, centered on a sort of circular "bubble". The progenitor star exploded as a type II Supernova in 1054 A.D., and was recorded as a bright "guest star" by Chinese astronomers. The surrounding nebula's emission is powered by the pulsar's radiation: exited ionized gases (Hα, OIII, SII) shine at characteristic wavelengths (orage-greenish features), while a diffuse azure glow is due to synchrotron radiation from accelerated electrons. Adapted from a ESO image. Credit: *ESO*.

1.4 The Crab Pulsar

This work studies the optical timing of the Crab Pulsar (V* CM Tauri, PSR B0532+21, PSR J0534+2200), a young and bright rotation powered pulsar, which is embedded in a large Supernova Renmant, the Crab Nebula (M1). The progenitor star exploded in 1054 A.D. as a type II supernova. Historical records from Chinese observers state that it appeared as a "new star" which outshined Venus and was visible in full daylight too. Nowadays, the pulsar is visible as a 17 mag star. Its distance from Earth is $\simeq 6523$ ly [20].

The Crab pulsar's rotational frequency is about $\nu = 30\,\text{Hz}$, the period being $T = 33\,\text{ms}$. The period increases by about $4 \cdot 10^{-13}$ s/s and the braking index which one measures far from glitches is $n = 2.5$ [16]. The Crab pulsar has been observed all the way from radio frequencies up to VHE γ rays ($\geq 100\,\text{GeV}$), [21]. The pulsar's pulse shape varies considerably with the observing frequency, but a typical double peaked morphology is observed. The signal consists of a sharp peak (main pulse) followed by a less intense

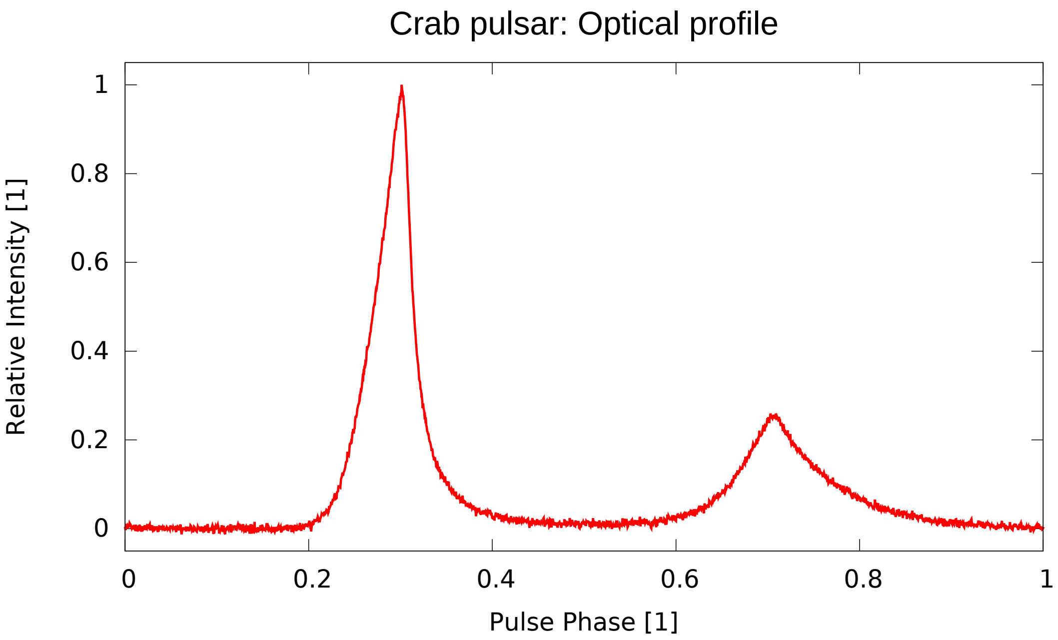

Figure 1.7: The Crab pulsar's optical pulse profile. The first peak is the main pulse, while the second weaker one is the interpulse. Obtained by integrating AQUEYE observation data spanning 200′.

one (interpulse) delayed by 0.4 in phase. Figure 1.7 shows a typical Crab pulsar's optical profile, obtained by integrating $\simeq 200'$ of optical data. In the radio band the Crab pulsar is known to exibit "Giant Pulses", i.e. single pulses which are $\simeq 1000$ times more intense than the average pulse intensities. When such a giant pulse occurs, simultaneous optical emission enhancements of the order of 3% were observed [22]. The mechanism responsible for such giant pulses is still unknown.

1.5 Emission mechanisms

Although pulsars have been studied for 50 years, a model describing how the broadband electromagnetic emission is actually produced is still missing. While many facts are still unclear, some circumstances are widely accepted, namely that the radio pulse must arise from a coherent emitter, whereas the IR-Optical and X-γ pulses are non-coherent emission. Most models identify the source of the radio pulsed emission in *plasma instabilities* in the relativistic plasma somewhere inside the light-cilinder, while higher energy radiation ougth to result from *synchrotron* and *curvature* radiation due to the intense magnetic fields. Extremely energetic γ rays ($\geq 100\,\text{GeV}$) are believed to result from the inverse Compton effect between synchrotron photons and relativistic electrons [21]. Multiwavelength observations, such as the ones presented in this work, may have a key role in clarifying details of these long sought emission processes and the geometry of the emission region [23], [24].

Chapter 2

Instruments

This chapter describes the ultra-fast photometer AQUEYE, which was used to aquire Crab pulsar's observations. The instrument's operating principles and design are briefly discussed; we refer the reader to specific publications for further details [1], [25]. A final section is devoted to the 182 cm 'Copernico' telescope of the Asiago Astrophysical Observatory[1] at Cima Ekar.

2.1 AQUEYE

AQUEYE (*Asiago Quantum Eye*) is an ultrafast photometer for astronomical observations, designed for very high resolution timing of variable phenomena. It features a sub-nanosecond relative timing accuracy and a dynamic range starting at $\simeq 1$ Hz which can extend up to $\simeq$ 8MHz, [1]. The very first AQUEYE setup was build in 2007 [26], [27] as a prototype for a truly "Quantum Photometer" to be used with the next generation 40 m – class telescopes (ELT). First Crab pulsar observations were made as early as of 2008 [28] and intended also to test the instrument on actual data. In 2009 a twin instrument was build, IQUEYE (*Italian Quantum Eye*), [29] with similar optomechanical design, to be used with 3.5 m – class telescopes such as the ESO NTT (La Silla, Chile) and the Italian TNG (La Palma, Canary Islands, Spain). Finally, in 2014 AQUEYE was also upgraded with improved mechanics and new optical components [3].

The aim of the whole project is to build an instrument for next generation telescopes, capable of pushing astronomic optical photometry to the realm of photonics, by measuring single photons' times of arrival. The exploration of quantum properties of light from astronomical sources (intensity interferometry, photon correlation spectroscopy) could open new perspectives in Astrophysics, shedding light on still debated phenomena, such as Pulsar emission. Furthermore, the ability of detecting light signals at very high frequencies may prove very useful for studying transient phenomena. These include

---

[1] The Astrophysical Observatory in Asiago is operated by OAPD (*"Osservatorio Astronomico di Padova"*), which is part of INAF (*"Istituto Nazionale di Astrofisica"*), the Italian national Astrophysics research institute.

both very energetic phenomena (early supernova stages, etc.) and planetary events (exoplanet transits, occultations).

2.1.1 Optical Design

The opto-mechanical design of AQUEYE, after its last 2014 upgrade, is scketched in Figure 2.1, while a scheme of the light path is visibile in Figure 2.2 (whole instrument) and Figure 2.3 (detector "head"). To describe the optical path inside the instrument, we refer to labels in Figure 2.1.

Two plane mirrors ① are first encountered by the beam from the telescope. These two mirrors are used to convey part of the light to a field camera ② and a sky background monitoring detector ⑦. The camera mirror has a slit on it, which is placed at the telescope focus. The light from a star goes through the slit and passes over in the focal reducer block. At this stage it is planned the insertion of an Adaptive Optics module Ⓐ, which has not been implemented yet. The beam then encounters a sliding dichroic mirror ③: this is used both to separate starlight of a certain wavelenght and to convey it to an optical vorticity coronographic module Ⓑ or to insert a signal from a stable led source ④ into the beam, for calibration purposes. The coronographic module is being built and is not yet operational. Next, the main beam passes through two filter wheels ⑤ which hold different filters, and finally reaches the AQUEYE head ⑥, where the main detectors are located.

Just before entering the instrument's head, the ray is focused by a lens on a pinhole, which ultimately crops the Field of View around the object of interest, masking undesiderable backgound and other sources' contamination. Different pinholes can be used, with sizes ranging from $3.5''$ to $8.7''$. Among variables influencing the pinhole choice, astronomical seeing (Point-Spread-Function FWHM) is of primary importance. The AQUEYE active detector is made up by four indipendent SPADs which operate in parallel. A SPAD (*Single Photon Avalanche Diode*) is a semiconductor device capable of detecting and time-tagging a single photon with great precision (see later). A single SPAD would not be sufficient for the intended purposes, mainly because of the high count rates from bright celestial objects and due to internal post-detection dead times. After the pinhole, light reaches a central mirror pyramid, which splits the incoming ray in four similar beams (see Figure 2.3). Each beam feeds a different SPAD: different filters can be inserted indipendently at each of AQUEYE's arms to achieve simultaneous multi-colour and/or polarimetric observation. A careful alignment procedure of the system has to be made in order to guarantee good optical efficiency. This is found to be $\simeq 85\%$ in the wavelength range $400 - 800\,\text{nm}$.

The SPAD

Each of the four signal detectors (plus the fifth one monitoring the sky background variation) is a SPAD manufactured by the Italian company MPD (Micro Photon Devices,

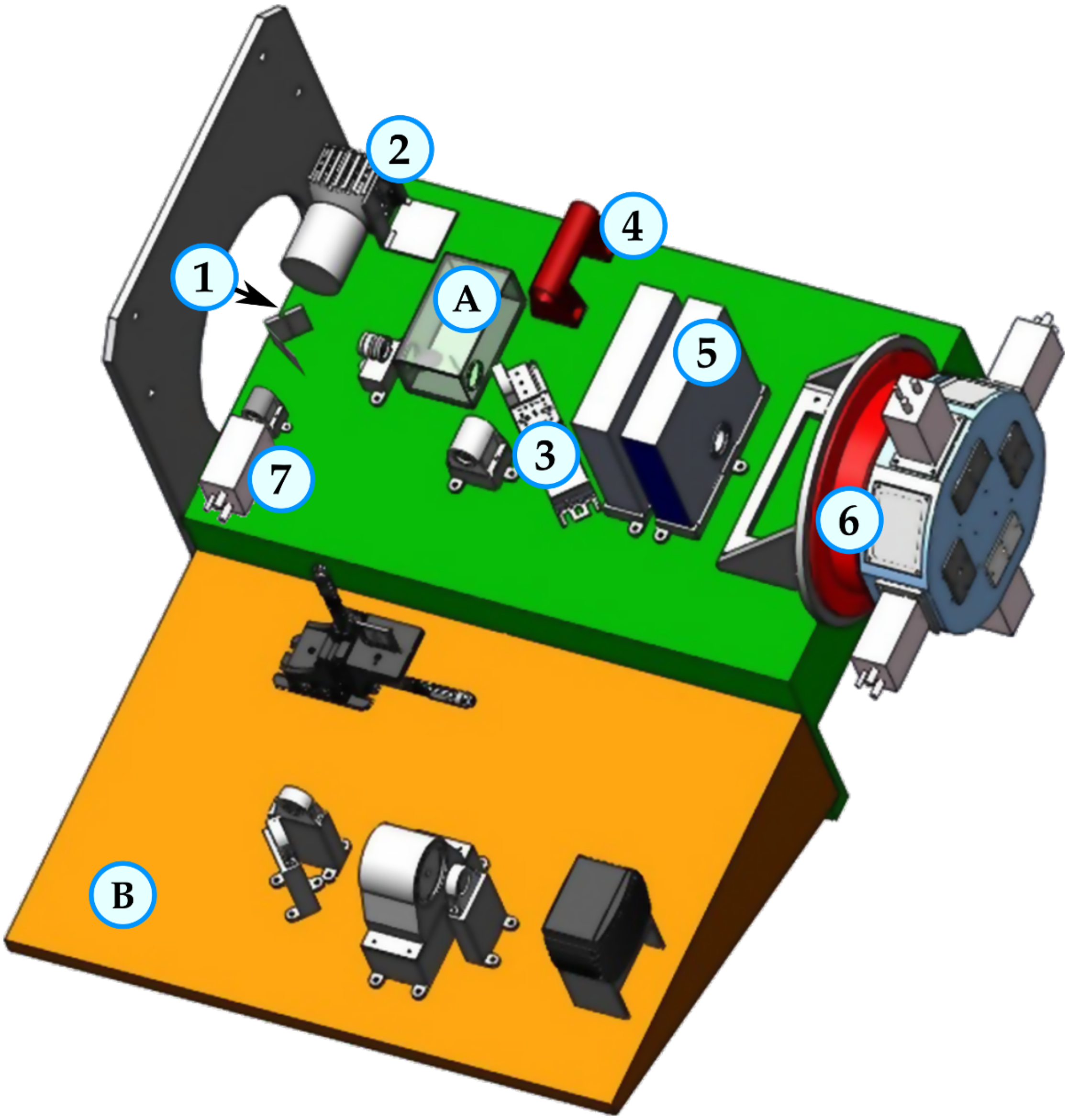

Figure 2.1: AQUEYE optomechanical scheme: ① Slit mirror (top) and sky plane mirror (bottom). ② Field camera. ③ Sliding dichroic mirror. ④ Calibration LED. ⑤ Global filter wheels. ⑥ Detectors (AQUEYE head). ⑦ Sky background monitoring detector. Ⓐ Adaptive Optics module (not yet implemented). Ⓑ Optical Vorticity Coronograph (currently not operational).

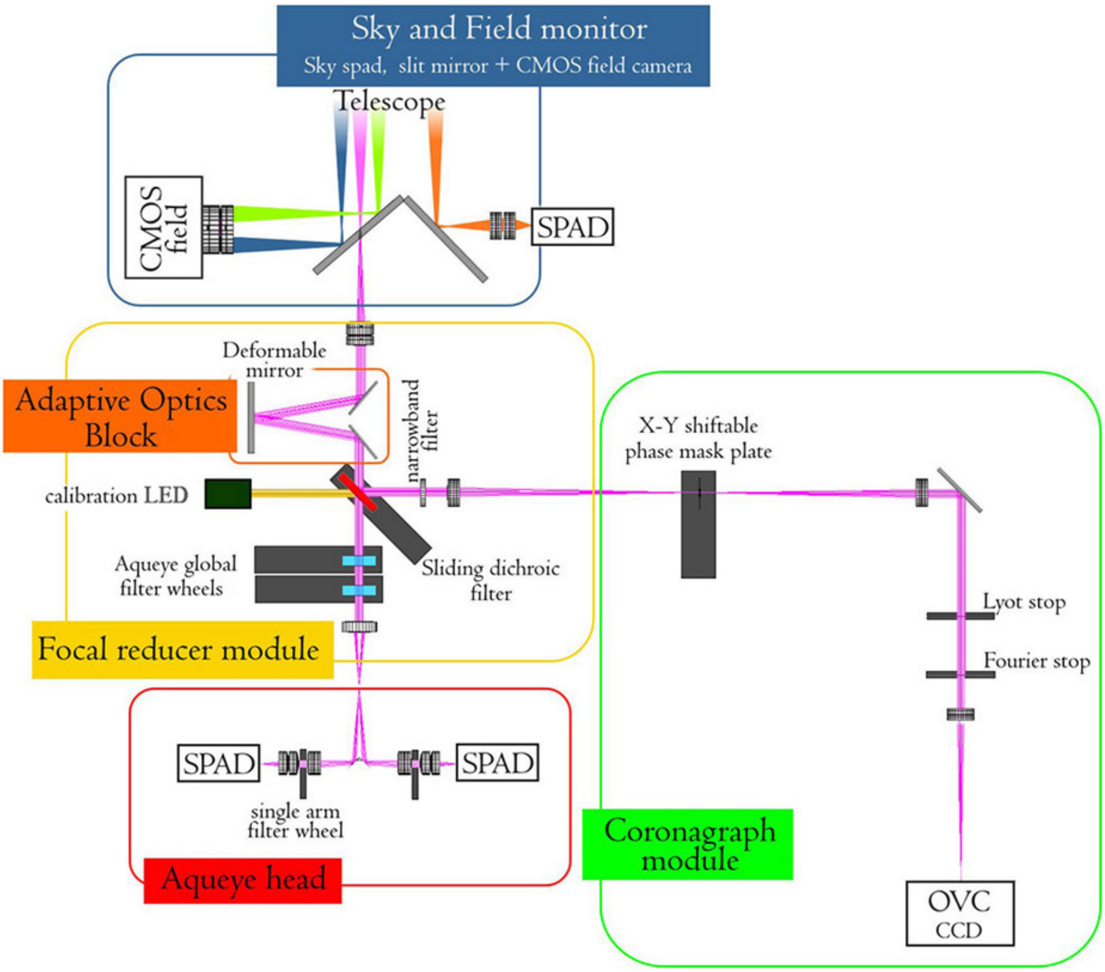

Figure 2.2: Light path across AQUEYE. The Coronograph and Adaptive Optics modules are not implemented at the moment. From [3].

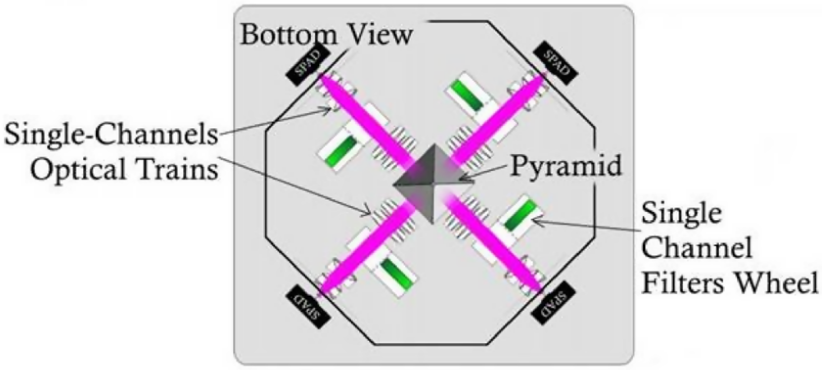

Figure 2.3: AQUEYE head (detector) scheme. Adapted from [3].

Figure 2.4: An MPD SPAD.

`http://www.micro-photon-devices.com/`). These detectors are essentially semiconductor diodes with a reverse bias higher than their breakup voltage, so that even a single photon-produced electron-hole pair in the depletion zone can ignite a cascade of ionizations and lead to a mA-regime detectable current. After breakup the detector needs to be *quenched* (the reverse bias current has to be stopped) and its reverse bias voltage needs to be restored to the initial over-breakup value. In MPD SPADs, this is achieved by active quenching circuits which recognize the reverse bias current, produce the time tag output signals, lower the voltage bias to stop the brackup current and then reset the diode to initial condition. This procedure takes about 75 ns, during which the SPAD is effectively blind (dead time). The use of more parallel and indipendent SPADs (as in AQUEYE) allow for a partial recover of this dead time.

The MPD SPADs used in AQUEYE have a 50 μm diameter active area, sealed by a flat BK7 glass window. Tests carried by the AQUEYE team at early development stages shown that the dark count rate (thermal noise) for each SPAD is generally lower than 100 Hz [1]. A peak quantum efficiency of $\simeq$ 60% at 550 nm was measured.

The MPD SPADs contain an integrated time circuit. The output can be obtained both as a TTL and NIM standard signal. While the former has a broader dynamic range (extending up to 12 MHz, versus the 2 MHz of the NIM signal), the time jitter on the NIM signal is much better than the TTL one(250 ps TTL versus 35 ps NIM) [29]. Since very high time accuracy is required for astrophysical timing analysis and for quantum-Astronomy applications, the narrower band NIM channel is used as signal carrier.

Recently, SPAD arrays have been developed and start being selled. The use of such a bi-dimensional device would greatly simplify the overall optomechanical design of an instrument like AQUEYE. This could be a good choice for a future new generation ultrafast photometer.

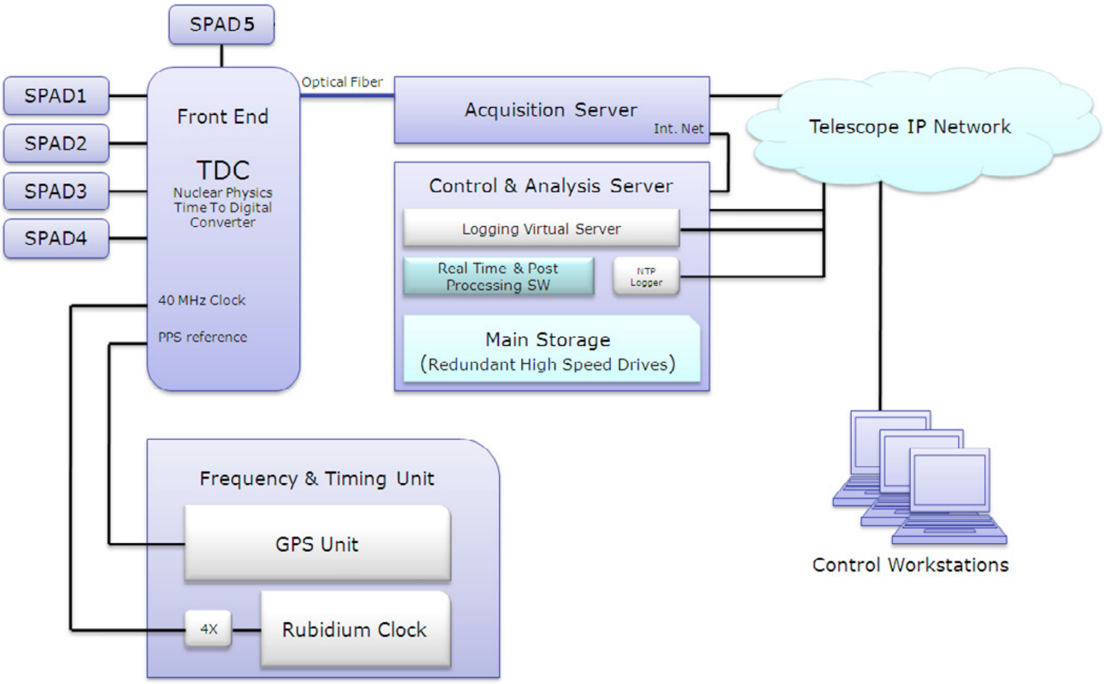

Figure 2.5: AQUEYE+ Aquisition System.

2.1.2 Data Acquisition

The data aquisition system is summarized in Figure 2.5. The five SPAD signals (four on source SPADs and the backgound monitoring one) are carried by equal length coaxial cables to a standard CAEN board with a TDC module. The TDC module has an internal quartz oscillator for timing accuracy, but this is not sufficient for the intended purposes: the module is thus locked with an external Rubidium Clock which ensures a very accurate reference frequency. In addition, a PPS (Pulse per Second) signal from a GPS receiver is fed to the TDC, to give an UTC reference signal. The GPS signal grants a 15 ns accuracy on each UTC PPS: this allows to stabilize the timing system against atomic clock's drifts. The overall accuracy for an absolute UTC tagged event provided by this system is $\simeq 0.5$ ns [29].

The TDC front end outputs raw data as a string of time tags, which are transferred through a fast optical fiber cable to the acquisition server, and ultimately to the storage system. Since very high count rate are registered for bright objects (see next section) and a time tagging string is given to each event, a typical observating night may use up to several Gb of HDD memory.

2.1.3 Current limitations

AQUEYE's timing capabilities are currently limited in the dynamic range at small scale by the SPAD noise of 100 Hz and at high scales by the maximum frequency of the NIM signal 2 MHz. Even using the less-accurate TTL signal, the acquisition system can reach no more than 8 MHz rates in the linear regime. In practise, the lower limit is irrilevant for observations from Asiago, since the sky brightness at Cima Ekar casts a much higher limit than the 100 Hz due to SPAD noise counts. Thus, while the faintest observable objects with AQUEYE at Asiago are at around 17.3 mag, the brighest ones are at about 5 mag. The Crab pulsar lay at the fainter side of this range at 16 mag, but its signal is strong enough to be detectable and scientifically usable.

2.2 182 cm 'Copernico' Telescope

The observations used in this work were acquired with the 182 cm telescope at the Asiago Astrophysical Observatory (observatory code 098), on the 1370 m high peak of Monte Ekar, at 45° 50′ 55″ N 11° 34′ 08″ E. The telescope was completed in 1973 and dedicated to Copernicus, but since then it received continuous upgrades. Its

Figure 2.6: The 182 cm 'Copernico' telescope at Cima Ekar (Asiago, VI).

primary mirror (M1) has a parabolic shape and a focal length of 5.393 m, while the secondary mirror (M2) is hyperbolic (⌀ 58 cm) and is 3.855 m away from M1. Both the mirrors are frequently alluminated. The optimum focus is reached by moving M2 in the three orthogonal directions; instruments are normally mounted at the posterior Cassegrain focus. Generally speaking, the optics performance is good, ensuring an average efficiency of 90% all the way from near UV to near IR. Recently, the telescope has been completely automated, and its operation can be remotely controlled from the Asiago Observatory main buildings (5 km away, nearby the city).

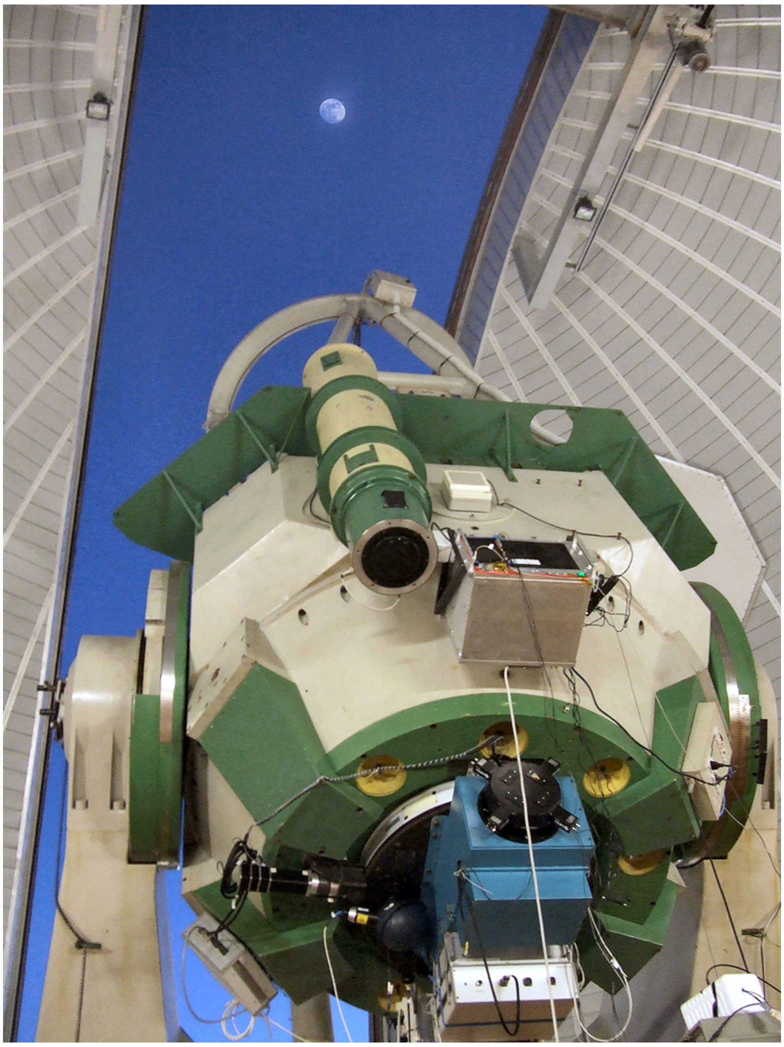

Figure 2.7: The 'Copernico' telescope at dusk. The AQUEYE head is mounted on AFOSC, the *Asiago Faint Object Spectrograph and Camera*.

Chapter 3

Data Analysis

In this chapter conceptual and operational details of the data analysis are presented. The main part concerns *phase analysis* and is presented in section 3.3. Some more in-depht technical details are given in appendix C. Actual data and results are presented in the next chapter.

3.1 AQUEYE's data

As discussed in the previous chapter, AQUEYE is a fast photometer with a very high ($\approx$ 100 ps) relative time accuracy [1], [29]. Its native output is a *Time Series* (TS), i.e. a list of ordered time-tags which a photon has been detected at. The long term stability is granted by a GPS signal, while time accuracy is ensured by a local Rubidium atomic clock. Some operations need to be performed on data before making them available for further analysis.

3.1.1 Post-acquisition operations

The raw data produced by AQUEYE is not an already usable TS, but is rather an output in the electronic's internal time representation (see section 2.1.2). Time-tags events are marked using the number of counts from the beginning of a voltage ramp which starts every $\simeq 52\,\mu$s. Each ramp is labeled by a reference signal which acts as a ramp counter, and every second a signal from the GPS ensures a local time reference. The first operation to be done is to regenerate pure UTC-referenced tags from these data. This reduction procedure, named *derollover*, is automatically accomplished by a dedicated software package developed for AQUEYE, and usually takes a few days to be performed.

3.1.2 Baricentring

A pulsar may be regarded as a very precise clock: the measure of its drifts must thus involve very precise time analysis. The time measured by a certain observer is affected by several effects, which depend on the observer's position on Earth, the time of the year, and the location of the source. To compare and relate different observations, but also to avoid spurious timing variabilities, a common reference frame is needed, and one indeed which is not subject to effects that generate timing variations. We are essentially seeking what best approximates an *Inertial System*: such a reference frame does not exist on Earth, being each point of it accelerated, neither on any single object of the Solar System. Since external gravitational forces acting on the Solar System's bodies are small compared to those acting internally, it seems reasonable for the nearest best inertial frame to be located at the *Solar System's Barycenter* (SSB). In fact, only the time coordinate is of interest for this work. The procedure which converts UTC times and local observer parameters to SSB times is called *barycentering*. Dedicated software exist to accomplish barycentering and the automated algorithms involved in the task have to account for different effects, as outlined below. [30], [31], [32].

1. **Geometry related effects**: delays caused by the relative position of the observer and the SSB.

    - **Rømer delay** ($\simeq 8'$ across the year): it accounts for the delay between the arrival of the same wavefront at the observatory and at the Solar System baricenter. It varies during the day and along the year, as the observer rotates and moves with Earth, and also on longer timescales, as the mutual position of the Sun and planets varies. Secular motions like the precession of equinoxes affect this term.

2. **Special-relativistic effects**: these delays depend on Special Relativity:

    - **Time dilation** ($\simeq 10^{-8}$ s): as Earth moves with respect to the SSB, a time dilation will be present between the two frames, its magnitude being dependent on the relative velocity between them. Since the Solar System Barycenter is always very close to the Sun, the motion of Earth is always almost perpendicular to the direction linking them. Time dilation, as the transverse Doppler effect to which it is related, is a second order effect, i.e. it grows with $\frac{v^2}{c^2}$, where v is the magnitude of the relative velocity.

3. **General-relativistic effects**: these timing differences arise from the curved nature of the spacetime inside the Solar System. They are mostly caused by the Sun, but also major planets (Jupiter and Saturn) should be taken into account [33].

    - **Gravitational redshift** ($\simeq 10^{-8}$ s): these delays arise because of the position of the Earth inside the Sun's gravitatinally curved spacetime. They depend on the Earth-Sun distance and the Barycenter-Sun distance as well.
    - **Shapiro delay** ($\leq 10^{-4}$ s): the Shapiro delay depends upon bending of light geodesics in a curved spacetime. The delay caused by both the Sun and the gaseous giant planets must be taken into account.

4. **Minor effects**:
    - **Optical dispersion effects**: they are caused by frequency-dependence in the optical propetries of the media which the electromagnetic waves from the pulsar travel across (interstellar medium, interplanetary medium, Earth atmosphere). These delays are largely negligible at optical wavelegths, but are significant in the radio band.
    - **Sovra-secular motions effects**: these are caused by Earth motions on very long timescales and by stochastic Earth movements (e.g. polar motion).

Two packages, which are largely employed in pulsar Astronomy, are available for baricentring: TEMPO and TEMPO2. TEMPO2 is a newer and rewritten version of TEMPO which accounts for additional minor effects and adopts different time coordinates. Although TEMPO2 is more accurate, since radio ephemerides are calculated using TEMPO and our aim is to compare optical data with them, in this work TEMPO has been used too.

3.2 Preliminary analysis

Once the time series from AQUEYE is reduced and baricentered, a first preliminary analysis must be carried on. The goal of this step is to characterize the overall data quality, to determine whether single observations are suitable for further analysis and to look for aquisition problems or failures. Observation logs have to be carefully inspected to check seeing, weather and general conditions: as the Crab pulsar lays a mere 1° off the ecliptic, the angular distance from the Moon is a constraining parameter and can drammatically affect the observations.

The analysis involves both time and frequency-domain approaches, the former being better suited for global quality check on long ($> 1\,\mathrm{s}$) timescales and the latter for signal analysis on short ($< 1\,\mathrm{s}$) timescales.

3.2.1 Light-curves

A time series can be binned over a fixed time interval δt to generate a light-curve (LC), which represents the photon flux versus time (time-domain analysis). LCs are useful to evaluate, by means of simple visualisation, global properties and long-term variability of the data set. It follows from definition that no variability shorter than δt can be studied this way. On the other hand, LCs with very small time bins may suffer from low statistics; short-scale variabilities are thus better studied in the frequency domain.

Figure 3.1 shows a typical Crab pulsar's LC from AQUEYE, with a binning time $\delta t = 1\,\mathrm{s}$ and covering 1 h of total observing time. In an ideal constant-flux source LC, points should fluctuate around an almost constant value, this value being the averaged flux of the detector's FOV: in reality a slowly rising or lowering trend might be present, mainly due to varying weather conditions and airmass changes[1].

If sky conditions are very variable, e.g mist veils pass inside the FOV, an LC might show irregularities, such as rapid changes or 'jumps' of the flux (see figure 3.2a). As long as the sky stays clear, jumps do not affect the signal too much, their effect being mainly an increase to the background (see section 3.3). If clouds start to cover the object, a rapid flux decrease will be registered[2]. During such a period, the detector is effectively blinded and registering only background: if these periods amount to a significant fraction of total observing time, corresponding to long intervals with low counts in the LC, the observation is likely to be of low quality or unusable.

As a first analysis step, LCs of each observation are carefully inspected. Irregularities, if any, are noted and traced back to possible causes. Datasets with very irregular LCs are

---

[1] **Airmass** is a measure of the optical thickness of the atmosphere which light from a source must go through to reach an observer. It is assumed to be 1 at zenith for an observer at sea level, and varies roughly as $\sec z$, where z denotes the angle from zenith to source.

[2] If the Moon has risen, a rapid increase is in fact to be expected, due to reflection on clouds.

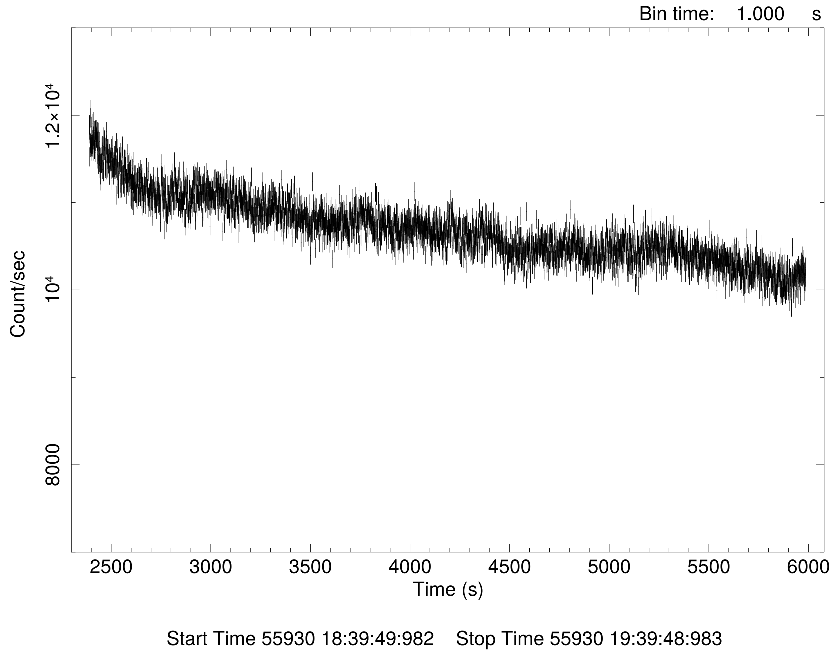

Figure 3.1: A typical light-curve plot: the flux on the detector is given as the photon count rate (ph./s = Hz) versus time. As a result of atmosphere turbulence and photon counting statistics, the LC show fluctuations. The global trend is determined by long-term variabilities in observing conditions, e.g. airmass variations due to changing elevation. These properties can be studied via the mean count rate F, standard deviation σ_F and root-mean-square variability RMS.

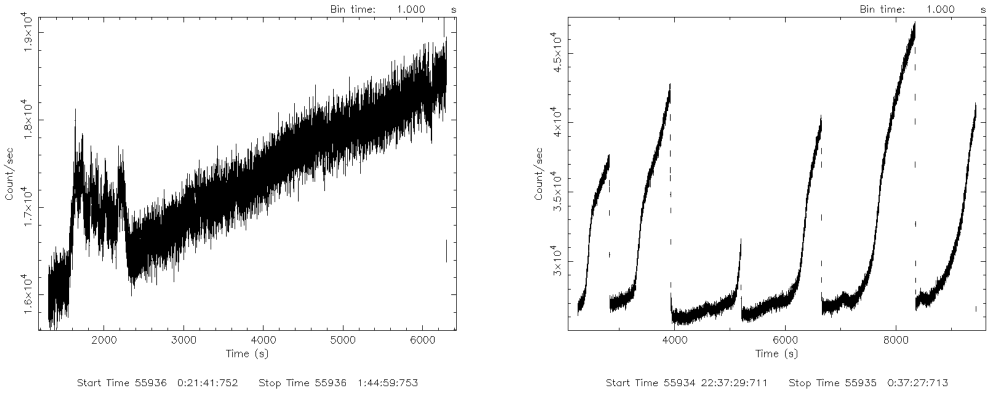

(a) LC with a 'jump' at the beginning. **(b)** Dome moonlight reflection peaks.

Figure 3.2: Different possible LC irregularities. Panel (a) shows a an increase in flux ('jump') due to passing mists. The LC in panel (b) presents quasi-periodic peaks, which were later understood to be caused by a reflection of moolight on the dome, modulated by the tracking movements.

less likely to contains good signal. Among the variables which are used to characterize the LCs, these are particulary notable:

- Mean flux $\boldsymbol{F}$ and variance $\boldsymbol{\sigma}$. If F differs much among observations taken on the same night, wheather is likely to have been very variable. Typical order of magnitude for the Crab pulsar is $F \simeq 10^4$ ph./s per spad.
- Constant-hypotesis reduced chisquare $\boldsymbol{\chi^2_{0,red.} = \chi^2_0/NDF}$. NDF is the number of degrees of freedom, usually equal to the number of points minus one. This is a measure of how good the data are represented by a constant. Very high values indicate that the LC has a significant slope.
- Linear fit reduced chisquare $\boldsymbol{\chi^2_{fit,red.}}$. A linear fit might be performed over the LC: if data doesn't follow a linear trend (e.g. broad 'bumps' are present), the reduced χ^2 value will be high.

3.2.2 Power-spectra

Short-time variabilities, those with a timescale less than 1 s, must be studied with an alternative method: since fluctuations in LCs with very small time bins may be big enough to overcome the signal, a better approach is to study its periodic components in the frequency domain. Basic Fourier Analysis notions are give in appendix A: here we recall only some important concepts.

The *Parseval Theorem* can be used to relate the sum of squared values of the signal to the analogous sum of squared values *of the Fourier transform*. In a discrete Fourier transform representation with N points, the theorem states that:

$$\sum_{i=0}^{N-1} |x_n|^2 = \frac{1}{N} \sum_{i=0}^{N-1} |X_n|^2 \tag{3.1}$$

Where x_n is the n-th signal entry, and X_n the n-th Fourier transform entry. Being the sum of squared values proportional to the total power P of the signal, a physical significance can therefore be attributed to the sequence $\left\{|X_n|^2\right\}$, their components being representative of *power separately emitted by each single Fourier component*. This sequence is called the signal's *power spectrum* P_n.

$$\begin{aligned} P_n &\propto |X_n|^2 \\ &\propto X_n^* X_n \end{aligned} \tag{3.2}$$

A convenient normalisation may be chosen for the power spectrum (PS). In this thesis the Leahy normalisation [34] is used:

$$P_n = \frac{2}{N} X_n^* X_n \tag{3.3}$$

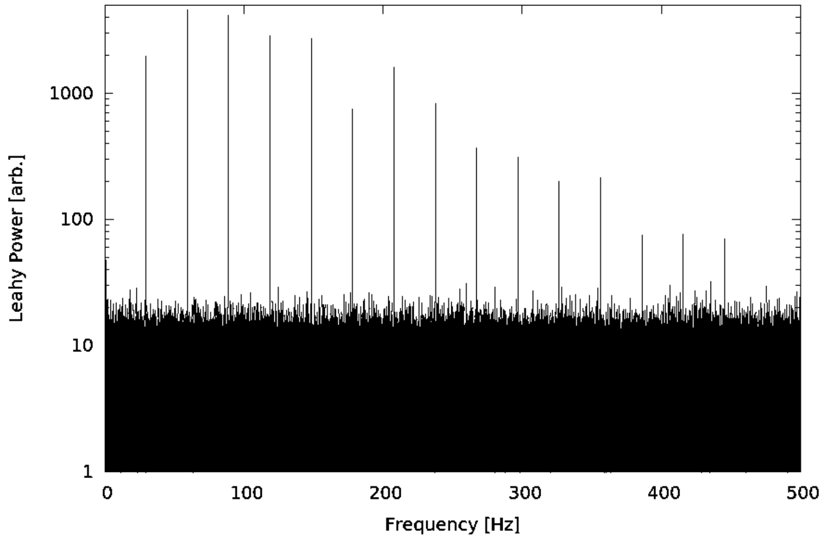

Figure 3.3: Power spectrum of the Crab pulsar (data taken with AQUEYE). Up to 15 lines (i.e. signal components) are clearly visible; white noise produces fluctuations at lower power levels. The leftmost line, at $\simeq 29.7\,\mathrm{Hz}$, is the fundamental frequency of the Crab pulsar, i.e. the reciprocal of its rotational period.

It can be shown that, with such a choice, the components of a pure white noise power spectrum will follow a χ^2 distribution with $k = 2$ degrees of freedom and will thus have an average value of 2. This is indeed a useful property, since it allows to directly compare spectra with different signal to noise ratios on similar scales. The probability $Q(w > P)$ that white noise power w alone can be larger than P is given by the χ^2 cumulative distribution, which is particulary simple in the $k = 2$ case:

$$Q(w > P) = e^{-\frac{P}{2}} \tag{3.4}$$

This can be used to evaluate the significance of a "line", i.e. a signal's spectral component. Given its power P, the smaller the white noise probability $Q(w > P)$ is, the more likely is that the line itself is a genuine signal.

The *Nyquist Sampling theorem* states that if a signal is sampled with frequency ν_S, corresponding to a sampling time $t_S = 1/\nu_S$, then the component with the maximum frequency which can be detected is the one which corresponds to the *Nyquist frequency* $\nu_N = \nu_S/2$ (see Appendix A). If present, a higher frequency component with $\nu \geq \nu_N$ will be *aliased*, that means detected a different frequency ν_A: direct calculation shows that ν_A varies with increasing ν as if it was *reflected back and forth* in the $(0 - \nu_N)$ interval. Therefore, studying a signal with frequency components up to ν, requires a minimum sampling frequency of 2ν, in order to avoid aliasing.
The workflow for signal analysis can thus be summarized as follows:

1. The time series is binned to an LC with a suitably short binning time. The

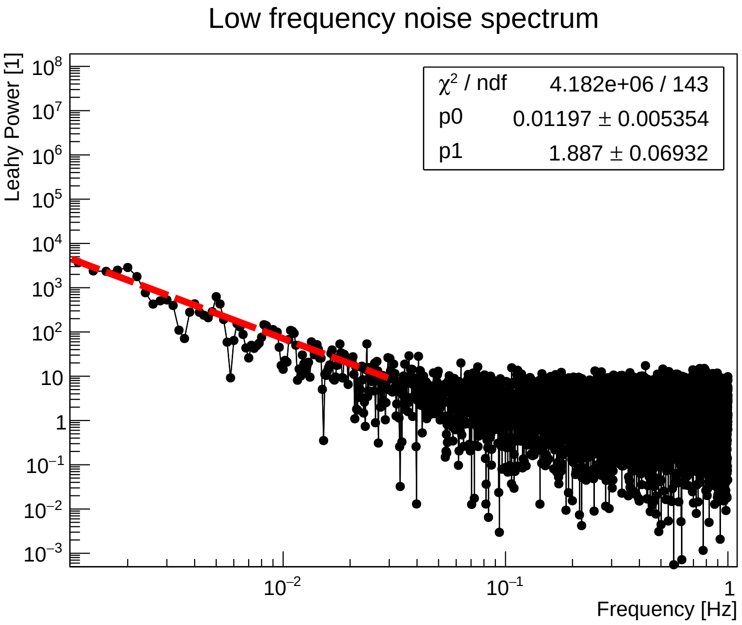

Figure 3.4: Low frequency noise spectrum. The leftmost part has been fitted with a power law $P = p_0 \cdot (\nu/1\,\mathrm{Hz})^{-p_1}$. The resulting value for p_1 is $p_1 = 1.89 \pm 0.07$, which is consistent with red noise.

binning time must guarantee a confortable inspection of the signal's fundamental harmonic and of higher harmonics too: for the Crab pulsar $\nu_0 \simeq 30\,\mathrm{Hz}$ and a sampling time $t_S = 1\,\mathrm{ms}$ ($\nu_N = 500\,\mathrm{Hz}$) may be a good starting value.

2. A forward Fast Fourier Transform (FFT) algorithm is used to compute the signal's Fourier transform. Being the signal always real, the Fourier transform obeys the relation $\mathcal{F}(-\nu) = \mathcal{F}(\nu)^*$. The PS is calculated with $P_\nu = \mathcal{F}(\nu)\mathcal{F}(\nu)^* = \Re[\mathcal{F}(\nu)]^2 + \Im[\mathcal{F}(\nu)]^2$.

3. The PS is inspected for lines and features. The spectral range $[0 - 1\,\mathrm{Hz}]$ is usually dominated by strong red-noise[3], which is tought to be caused by air turbulence and seeing. Since the $\nu < 1\,\mathrm{Hz}$ interval can be studied also in the time domain, the frequency analysis can be restricted to $\nu > 1\,\mathrm{Hz}$, where the spectrum isn't affected by red noise. The region around 30 Hz is carefully analised to search for the fundamental frequency. The total number of lines L and the power of the fundamental line P_1 are recorded, along with the white-noise shot probability for the fundamental frequency $Q(w \geq P_1)$ and the maximum power and its frequency ν_{max}, p_{max}. Usually ν_{max} is equal to the frequency of the second harmonic, $\nu_{max} = \nu_2 = 2\nu_1$.

---

[3] **Red noise** (see figure 3.4) is a form of frequency noise $\mathcal{N}(\nu)$ whose power decreases with ν^{-2}. It can be caused by several different physical effects

3.3 Phase analysis

3.3.1 Basic concepts

The goal of phase analysis is to track the rotation of the pulsar and to compute precise ephemerides for the occurrence of luminosity pulses: this can only be achieved by observing the pulsar for a suitably long time and recording the times which the pulses arrive at. The pulsar's phase can be defined as:

$$\varphi\left(t\right) = \varphi_0 + \nu\left(t - t_0\right) + \frac{1}{2}\dot{\nu}\left(t - t_0\right)^2 + ... \tag{3.5}$$

where φ_0 is the value of the phase at $t = t_0$ and (ν, $\dot{\nu}$, ...) are the pulsar's rotation frequency and its derivatives at t_0. If the pulsar were a pure uniform rotator with period T and frequency $\nu = 1/T$, the phase would increase by 1 as time increases by T, being:

$$\varphi\left(t\right) = \varphi_0 + \nu\left(t - t_0\right) \tag{3.6}$$

The phase acts as a counter for pulsar's turns since a given time. The choice of φ_0 is arbitrary, but it is customary to set it according to these rules:

1. The *fractional part of* φ_0, $\psi_0 = \mathrm{frac}(\varphi_0)$ accounts for the "rotational" degree of freedom, i.e. the choice of the moment which a new turn starts at. This is set so that a turn begins when the pulsar's main pulse is revealed, ensuring that main pulses correspond to integer phase values.

2. The *integer part of* φ_0, $\Phi_0 = \mathrm{int}(\varphi_0)$, accounts for the "time translational" degree of freedom, i.e. the choice of rotation number 0. This lesser important parameter is usually set to be 0.[4]

Once the *phase curve* has been determined, it can be used to study how the rotation of the pulsar varies with time, and hence to determine propetries of interest in pulsar Physics (e.g. the braking index n). Different timing solutions can be compared to check which is more in agreement with the data: multiwaveleght ephemerides can be studied to determine if there might be any wavelength dependent phase shift.

It is usually more convenient to operate with the phase drift $\psi\left(t - t_0\right)$, which accounts for the deviation between the actual phase and that of a reference uniform rotator with

---

[4] Splitting fractional and integer parts of φ_0 makes sense since phase is later determined with a global least-squares fit of main pulses arrival times (see section 3.3.3). The fit has ψ_0 as a parameter, while being completely unsensitive to Φ_0.

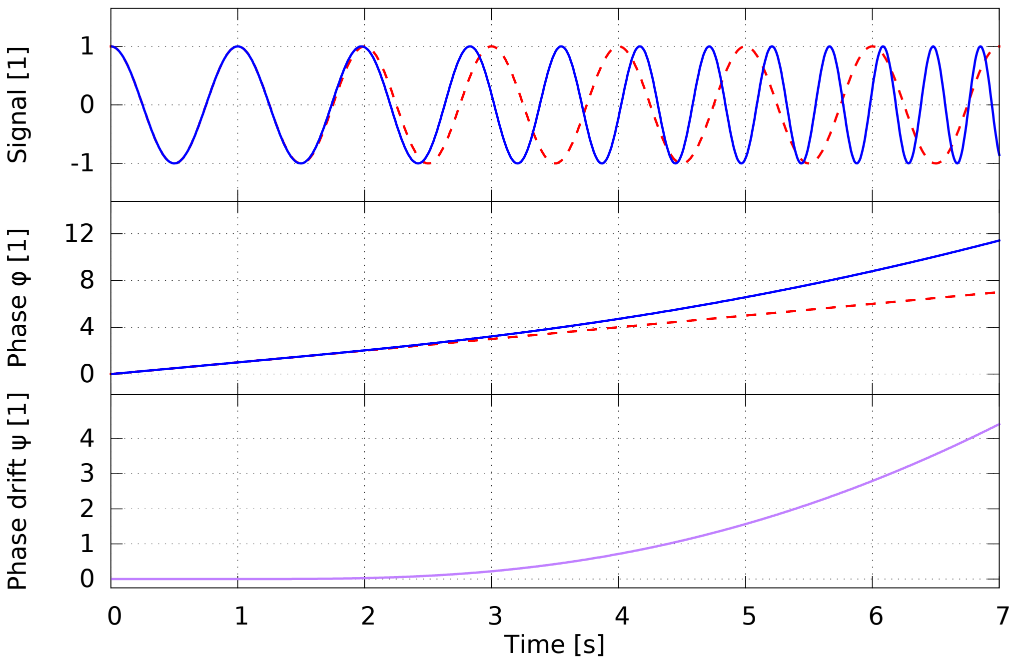

Figure 3.5: Graphical explanation of concepts in paragraph 3.3.1. The upper panel shows a signal (blue curve) and a reference rotator (red dashed curve). The temporal gauge (t_0,ν_0) is chosen such that as $t = 0$ s the signal and reference are on phase and both at a maximum.
The mid panel shows corresponding phases φ: each of them gains a +1 difference every time a cycle is completed (i.e. when a maximum is reached again); the phase for the uniform rotator is simply a straight line.
As time increases, the signal develops a phase shift with respect to reference, due to varying frequency: this can be seen in the lower panel, which plots the difference between signal's and reference's phases, the phase drift ψ. When the two signals reach again an istantaneous on-phase condition, ψ is an integer. In this example the signal's frequency increases with time, as if the rotation was speeding up; in the actual Crab pulsar's case, the rotation is slowing down and so the sign of ψ is expected to be negative.

period T_0 and frequency ν_0:

$$\begin{aligned}
\psi\left(t' = t - t_0\right) &= \underbrace{\varphi\left(t\right)}_{\text{Proper phase}} - \underbrace{\left[\Phi_0 + \nu_0\left(t - t_0\right)\right]}_{\text{Reference rotator}} \\
&= \psi_0 + \left(\nu - \nu_0\right)\left(t - t_0\right) + \frac{1}{2}\dot{\nu}\left(t - t_0\right)^2 + \ldots \qquad (3.7) \\
&= \psi_0 + \left(\nu - \nu_0\right)t' + \frac{1}{2}\dot{\nu}t'^2 + \ldots \qquad (3.8)
\end{aligned}$$

For observations covering a long time interval, higher orders in equation 3.5 become more and more important, causing a drift between the pulsar's phase and that of the uniform rotator, i.e. a variation of ψ. Such a variation equals an integer N when the two signals are again in phase after a shift of N reference periods T_0. A graphical explanation can be viewed in Figure 3.5.

The relation between $\psi\left(t'\right)$ and $\phi\left(t\right)$ is completely specified by the parameters t_0, Φ_0 and ν_0, namely:

$$\varphi\left(t\right) = \Phi_0 + \nu_0\left(t - t_0\right) + \psi\left(t - t_0\right) \qquad (3.9)$$

The set $\{t_0, \Phi_0, \nu_0\}$ will be called a "temporal gauge" throughout this document. Occasionally also the expressions $\{t_0, \Phi_0, T_0\}$, where T_0 is the period reciprocal to ν_0, and $\{t_0, \nu_0\} = \{t_0, 0, \nu_0\}$ will be used. Transformations from a temporal gauge to another are treated in Appendix B.

3.3.2 Folding

In order to track the phase, one has to identify times at which main pulses arrive; in principle, this could be done by generating a lightcurve with a sufficient number of bins to solve the pulse's profile and cross-correlate it with the signal. However this approach is usually not reliable, because such a short time-binned LC is noise-dominated and results in too a low statistics.
It is then necessary to employ *folding* techniques on a longer period of time to improve the signal to noise ratio and make the main pulse profile cleary resolvable. The idea of folding derives from observing that the pulsar's signal is periodic (at least on short time-scales), while noise is completely random. If the signal's period T were known, a longer observation (say lasting $N \times T$) could be used to make a better estimate of the pulse profile, since the signal at time t is in phase with the one at $t + n \cdot T$.

Figure 3.6 presents a graphical scheme describing folding: a short time-binned LC[5]

---

[5] In fact, it is not necessary to generate a lightcurve; folding can be applied directly on a time-series, mapping the arrival-time t into t modulo T:

$$(t) \rightarrow (t \bmod T)$$

and generating a lightcurve only after the procedure is completed. This approach was used during the actual analysis.

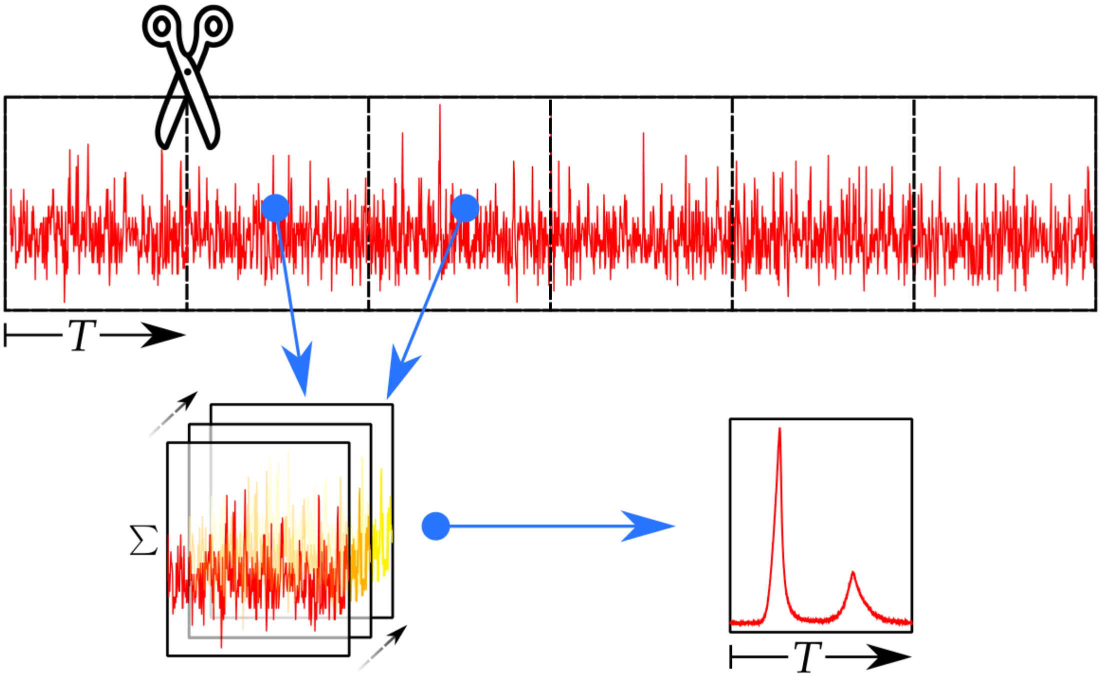

Figure 3.6: Folding scheme. **1.** A lightcurve is divided into segments which last exaclty 1 signal's period. **2.** All segments are stacked together, values of corresponding bins being summed together. **3.** Resulting LC has a much higher signal to noise ratio.

with a duration t_{fold} is divided into slices lasting exactly one period T. These slices are then stacked, the values of corresponding bins being summed. The resulting LC lasts only one period, but has a higher statistics; if noise is Poisson-distributed, the S/N ratio is on average $\sqrt{t_{fold}/T}$ times higher then the one of the unfolded curve. For further phase-analysis, the folded LC is referenced to the mid-point of the original time interval.

Epoch Folding period Search It is evident that a very precise determination of T is needed to perform a succesful folding. Such high precision mesure can be obtained for a long exposure ($t \simeq 30'$, depending upon observation quality) with a χ^2 maximization technique (EFS, *Epoch Folding period Search*) which works as follows:

1. Trial values of the period T_i ($i = 1, ..., N$) are used to fold the whole data into N different folded LCs;

2. The RMS of the residuals of each LC from its average value is computed. This value is equal to the chi-square computer assuming a constant rate, χ^2_i. The couples (T_i, χ^2_i) are stored.

3. If the period T_i is close to the true period T, its χ^2 is likely to be high, since a long exposure folding grants very high statistics on the pulse profile and the resulting

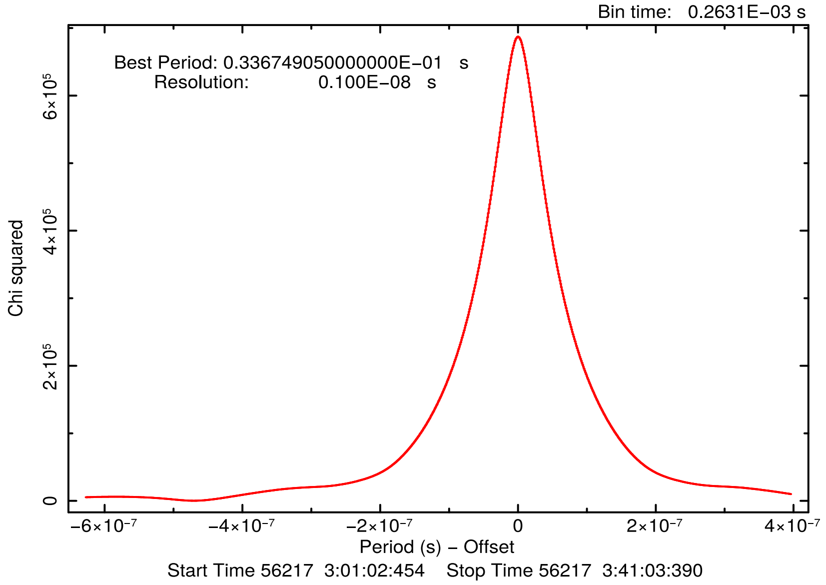

Figure 3.7: EFS curve. $N = 1024$ different trial periods separated by a step of 1 ns have been used to fold a $40'$ long observation of the Crab pulsar; an initial guess for the period was obtained from the power spectrum's fundamental harmonic. A second narrower EFS with 10 ps step and a parabolic fit were later used to determine the period with a ∼ 1 ps resolution. The curve's shape is related to the power spectrum's structure and to the observation's duration (see appendix E for an analitic approach).

lightcurve will be far from being constant.[6]
On the other hand, if the period T_i is far from the actual one, folding a long-duration dataset will result in signal continuosly keeping off-phase in each following T_i segment; the final sum will thus average out any profile shape giving an almost constant LC: in this case the corresponding χ^2 will be low.

4. Finally, the data set (T_i, χ_i^2) is fitted around its maximum with a parabola to determine an even more accurate value of T.

A plot of an EFS is visible in figure 3.7.

---

[6] An interesting anlogy can be drawn with the well known algebraic relation:

$$\frac{1}{2\pi}\int_0^{2\pi} e^{i(k-k')t}\,dt = \begin{cases} 0 & k \neq k' \\ 1 & k = k' \end{cases} \tag{3.10}$$

Where k can be associated with the real period T and k' with the trial one. In fact folding involves a periodic summation which is analogous to the integral in 3.10.

3.3.3 Phase tracking

Since we are interested in studying how phase evolves with time, but we are bound to fold data to actually measure the phase, we will proceed as follows:

1. An observation lasting t_{obs} is divided into k folding segments S_i lasting t_{fold} each, whose mid-times are $t_{1/2,\,i}$.
2. Each segment is folded with the EFS period T_0 of the observation.
3. The resulting k folded LCs, with their associated measurements of the phase of the main pulse, are then referenced to their mid-time $t_{1/2,\,i}$.

The principal drawback of this procedure is the loss of information on the integer part of the phase. Next paragraphs cover more in detail this topic, its problems and solutions.

Peak shift δ

Data folded with the method described above have a tight relation with the phase drift ψ defined in equation 3.9.

Imagine the pulsar were a uniform rotator with period T_0: after folding its signal as just described with the exact same period T_0, we would end up with a certain number of folded LCs, each of them being in-phase with the others. As the reference time t_0 may not necessary be the time of arrival of a main pulse, these lightcurves would show a constant shift δ between their beginning and the peak itself. Recall that the phase drift ψ (equation 3.8) for a reference frequency ν_0 equal to the actual frequency of the rotator would also be constant and equal to ψ_0.

Suppose now the rotation isn't uniform and varies slowly. As the period $T = T_0 + dT$ of the signal changes from the initial value T_0, a phase drift $\psi(t)$ develops, such as the one in figure 3.5. Conversely, as folding still proceeds with the period T_0, being the signal slightly off that periodicity, at each rotation it accumulates a tiny[7] dT/T_0 delay that builds up a varying peak shift $\delta(t)$. It is quite simple to realize that these two descriptions are equivalent. A growing $\psi(t)$ (period decreases, frequency increase) corresponds to a backward-shifting peak in folded lightcurves (δ decreases), whereas a waning $\psi(t)$ (period increases, frequency falls) corresponds to forward-shifting peak (δ grows). The correlation between ψ and δ must then be of the type $\psi \propto -\delta$.

As the folded LC peak is reaching $\delta = 1$, another image of it is entering the LC from the opposite side, near $\delta = 0$: when the first image finally moves out of the LC, the second one steps in, eventually reaching the initial peak position at $\delta = \delta_0$, corresponding to a phase drift of $\psi = \psi_0 \pm 1$. This settles a linear relation between δ and ψ, but for integer

---

[7] See next paragraph for a discussion on the actual magnitude of this term and on its effects.

shifts in δ, since $0 \leq \delta \leq 1$. Noting that $\psi \propto -\delta$ from the previous paragraph, we finally deduce that the equation bounding δ and ψ is:

$$\delta(t) = \mathfrak{F}\{1 - \psi(t)\} \tag{3.11}$$

where $\mathfrak{F}\{\cdot\}$ stands for *the fractional part*. δ and ψ are explementary phases, i.e. they sum up to an integer number. We choose this number to be 1, other choices adding a mere integer shift to ψ.

It has been shown that there exist a correspondence between data folded starting at t_0 with period T_0 and the phase drift ψ relative to the temporal gauge $\{t_0, T_0\}$. The phase analysis can be thus accomplished by folding the data, using then equation 3.11 to derive the phase drift and finally employing equation 3.9 with the proper gauge to derive the phase $\varphi(t)$. The core and most critical part of the task is the transformation of δ to ψ, because only its fractional part can be derived from equation 3.11, while the integer one has to be reconstructed a posteriori (see next section).

Folding limits

The method presented above is applicable only if the folding period is very close to the real period for the whole duration of the observations. Indeed, during the folding interval t_{fold} the peak position δ varies too, because of two effects:

1. The period itself T varies during the folding interval t_{fold}.
2. A yet present period offset $\Delta T = T - T_0$ is amplified by the cycles rolling during the folding interval.

The second effect is by far dominant, but it requires first a small initial period offset to be present. Magnitudes for both the effects can be easily calculated for the ideal case of a rotator whose period varies linearly with time (see below and appendix D).

These drifts affect the shape of the folded lightcurve. If the variation of the peak shift δ which develops during the folding time is significant, the folded LC will sum up different phase determinations, the resulting profile being smoothed. The phenomenon is just the same as the one explained in section 3.3.2 for the EFS technique (see also appendix E). In order to have valid results, one has to try and reduce this effects under a significance threshold. Since variations shorter than a phase bin are already wiped out while building the bin content, the bin-width itself may be chosen as threshold.

If we plan to fold data spanning for a period t on a folding base segment t_{fold} and using N_ϕ bins per lightcurve, we ought to check that the $\Delta\psi$ developed in t_{fold} is always shorter than $1/N_\phi$ over the whole interval t. If, as customary, the folding period is taken near the reference time t_0 for the observations, assuming a linear varying period

$T = T_0 + kt$ leads to:

$$\psi(t) = -\frac{k}{2}\frac{t^2}{T_0^2} \tag{3.12}$$

$$\Delta\psi_t(t_{fold}) = -\frac{k}{T_0^2} t \cdot t_{fold} \tag{3.13}$$

The first equation being associated with effect number 1, and the second with effect number 2. Since the second one is dominant, it is possible to set an upper limit to the number of phase bins as:

$$N_\phi(t, t_{fold}) \leq \frac{1}{k}\frac{T_0^2}{t \cdot t_{fold}} \tag{3.14}$$

Detailed calculation for the Crab pulsar are listed in appendix D. It should be noted that a minimum number of $\simeq 100$ bins is required to adeguately resolve the pulse shape. If N_ϕ falls below such limit at some t, it is impossible to resolve the peak. In such cases, it is necessary to fold part of the data with a different reference time t'_0 and folding period T'_0 (i.e. within a different temporal gauge G'); it is then possible to transform these values back to the first gauge using temporal gauge transformations. This is the procedure to follow to globally fold very distant observations, such as the October and January ones (see section 3.3.4 and appendix B).

Workflow

Steps followed to determine $\delta(t)$ are thus:

- The observations are divided in groups (usually an observing session) which can be analized together. A reference period is determined with an EFS procedure on the initial data of each group. For each group the folding parameters N_ϕ, t_{fold} are chosen to satisfy condition 3.14 and to allow the best possible statistics. In our case, there were two groups, one covering the January observations and another for the October ones.
- The data in each group are divided in segments lasting t_{fold} and folded with the proper folding period. A set of folded lighcurves is produced at this case.
- The pulse profile in each LC is fitted with an analytical template[8] [24] to determine with high accuracy the peak shift δ. The analysis has actually been performed twice with two different fitting softwares[9] to test its stability against the fitting algorithm.
- Finally, the values (t_i, δ_i, σ_{δ_i}) as well as the two control values $\chi^2_{const.}$ and χ^2_{fit} (the chi-square values with respect to a flat and pulse-like profile, respectively) are saved in a file for later use.

---

[8] The template was build by modeling actual data with a set of 16 Lorentz curves. See appendix F.

[9] See appendix C for computational details

3.3.4 Phase curve

In this last section we present the steps to reconstruct $\psi(t)$ and $\varphi(t)$ from the data $(t_i, \delta_i, \sigma_{\delta_i})$. To do this, it is useful to recast the phase drift Taylor expansion 3.8 in the form:

$$1 - \psi(t') = p_0 + p_1 t' + p_2 t'^2 + ... \tag{3.15}$$

We recall that δ is only related to the *fractional part* of ψ, being $\delta = \mathfrak{F}\{1 - \psi\}$. If the peak shift δ crosses the value 1 while folding, this will result in an abrupt discontinuity in the data, the following point being near phase 0. It is straightforward to recover such discontinuities simply by means of translating all following data by +1.

But what if a phase 1 crossing happens at a time when no observation is being done? This can happen at times between different acquisitions or also during daytime. There is no direct way of knowing precisely how many turns have been completed during such a period: it is only possible to derive the shift occuring during the gap by studying how previous and following data vary.

Data cleaning

Sometimes, if the quality of the observations is very poor, (t, δ) data need to be cleaned up by misleading points (outliers) produced by wrong or failed LC fits. To accomplish this, a dedicated procedure has been developed, based on both a goodness of fit and a phase continuity criterion:

- As mentioned before, the fit algorithm produces also the values $\chi^2_{const.}$ and χ^2_{fit}, the residuals' RMSs of fitted data from their mean value and the fitted profile, respectively. If the template fits the data well, the corresponding χ^2_{fit} should be small; conversely, if the fit is successful it is likely that most prominent features such as the main pulse and the interpulse are clearly resolved, and the $\chi^2_{const.}$ with respect to a constant will not be be good, since residuals from the mean are not randomly distributed. The ratio:

  $$r_\chi = \frac{\chi^2_{fit}}{\chi^2_{const.}} \tag{3.16}$$

  is thus likely to be smaller than 1. On the other hand, if the fit fails in detecting the correct main pulse shift δ, it is rather probable that the folded LC statistic is not even sufficient to solve the main pulse. In this case χ^2_{fit}, would be bad, while $\chi^2_{const.}$ would probably be good (if no signal can be detected, the LC is likely to be flat). The ratio r_χ will, in such a case, be greater that 1.

  Therefore, a first criterion for evaluating the significance of δ is the inspection of the ratio r_χ.

- A second criterion that is used to evaluate the significance of a point is based on an approach a posteriori. The basic idea is that, apart from the +1 phase jumps described above, the $\delta(t)$ function should be continuous, since $\psi(t)$ (a polynomial) is continuous. It is possible to check how a single point behaves with respect to the local trend defined by nearby points by discrete convolving the values δ_i with a rectangular-like function:

  $$\mathrm{med}_N(\delta_i) = \mathrm{median}(\delta_{i-N}, \delta_{i-M+1}, ..., \delta_i, ..., \delta_{i+N-1}, \delta_{i+N}) \tag{3.17}$$

  The median is preferred over the aritmetic mean because it is much less sensitive to outliers with low sample numbers[10]. We can then compute the compatibility between these two values, namely:

  $$\mathrm{comp}_N(\delta_i) = \frac{|\delta_i - \mathrm{med}_N(\delta_i)|}{\sigma_{\delta_i}} \tag{3.18}$$

  If δ_i is on the same trend defined by surronding points, $\mathrm{comp}_N(\delta_i)$ is likely to be very small, since in that case $\mathrm{med}_N(\delta_i) \simeq \delta_i$. On the other hand, if δ_i is an outlayer, being the median rather unsensitive to it, the value $\mathrm{med}_N(\delta_i)$ will lay anyhow on the surronding's trend and $\mathrm{comp}_N(\delta_i)$ will be very high. If δ_i is a value next to an outlier, the median clips the outlayer and the comp_N is small anyway.

---

[10] In CCD imaging, it is a standard procedure to use the median of a small set of frames to remove stochastic noise such as the one originated by cosmic rays.

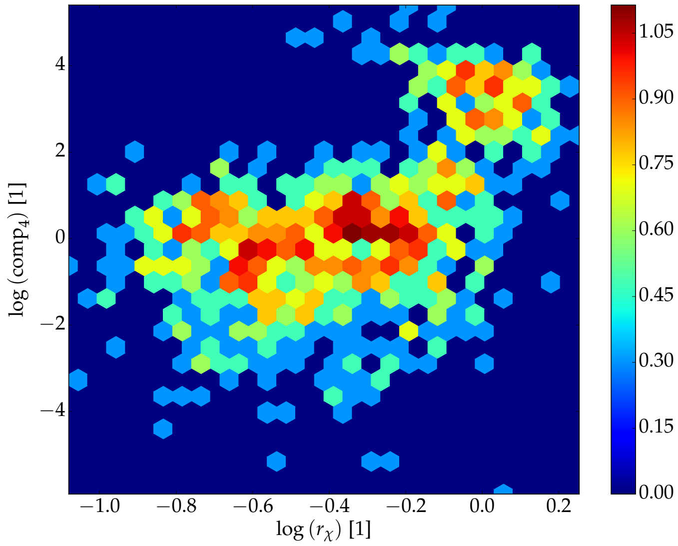

Figure 3.8: (r_χ, comp_4) scatterplot; colour gives relative point density. See text for details

Figure 3.8 presents a log-log scatteplot of $(r_\chi,\ \mathrm{comp}_4)$ values for roughly 1300 points. The point population is splitted in two distributons: a low compatibility broad distribution at $r_\chi < 1$ and a "satellite" distribution at $r_\chi \simeq 1$ with very high compatibility ($> 10^2$). The distributions are weakly separated by a "canal" at $(\log r_\chi,\ \log \mathrm{comp}_4) = (0, 2)$, which is slightly oblique and corresponds to a power law:

$$r_\chi \cdot \mathrm{comp}_4 \ = \ 2 \tag{3.19}$$

This analisys suggests that the larger distribution contains significant points, whether the satellite one is mainly filled with wrong peak identifications or failed fits. Indeed, selecting only points which fall in the main distribution, i.e. applying the criterion $r_\chi \cdot \mathrm{comp}_4 \ \leq \ 2$, results in removing almost all outliers, essentially leaving regular data untouched. The rejection accuracy is around 99%, leaving even the points close to a phase jump untouched (their median compatibility is huge, but r_χ stays small).

Of course, relation 3.19 may be different for diverse datasets. Since only one observations' group (the January one) was affected by low statistics and noisy signal, this could not be tested. Indeed, it appears that applying such a procedure on poor quality data could greatly improve the final results.

Polynomial χ^2 minimization and local rephasing

The final step is to regenerate the phase drift ψ from δ. To do so, one has to guess the correct integer shifts I_1, I_2, ..., I_n that occur among different data acquisions.

Figures 3.9 and 3.10 on next pages depict how this task is accomplished. The procedure is concepually simple: trial values of the shifts are used to translate data, which are later fitted with a polynomial of the form 3.15 (usually a parabola or a cubic function). The shifts or indices $\mathcal{I} = (I_1, I_2, ..., I_n)$ that produce the fit with the best reduced chi-square χ^2_{red} are the most likely correct ones.

Generally speaking, the n-tuple of the indices I define a point $\mathcal{I}$ in an n-dimensional indices space. If L trial values are going to be tested for each index, the "volume" of the n-D search-box is L^n. The total number of possibilities grows then as the n-th power of L and exponentially with n. This means that even an approximate hint on the actual values in $\mathcal{I}$ is important to make the process feasible; such a hint can be obtained, for example, by the slopes of data in previous runs. Luckily, since the polynomial form 3.15 is linear in the parameters p_0, $p_1, ...$ a considerably faster linear regression of grade n can be performed. More detailed information on the computing part can be found in appendix C.

The seeked χ^2 minimum is usually a very deep one: figure 3.10 shows a minimum in a bidimensional indices space which is 10^3 times smaller than any other value. It is a good idea to proceed in fitting with low grade polynomials first, and moving to

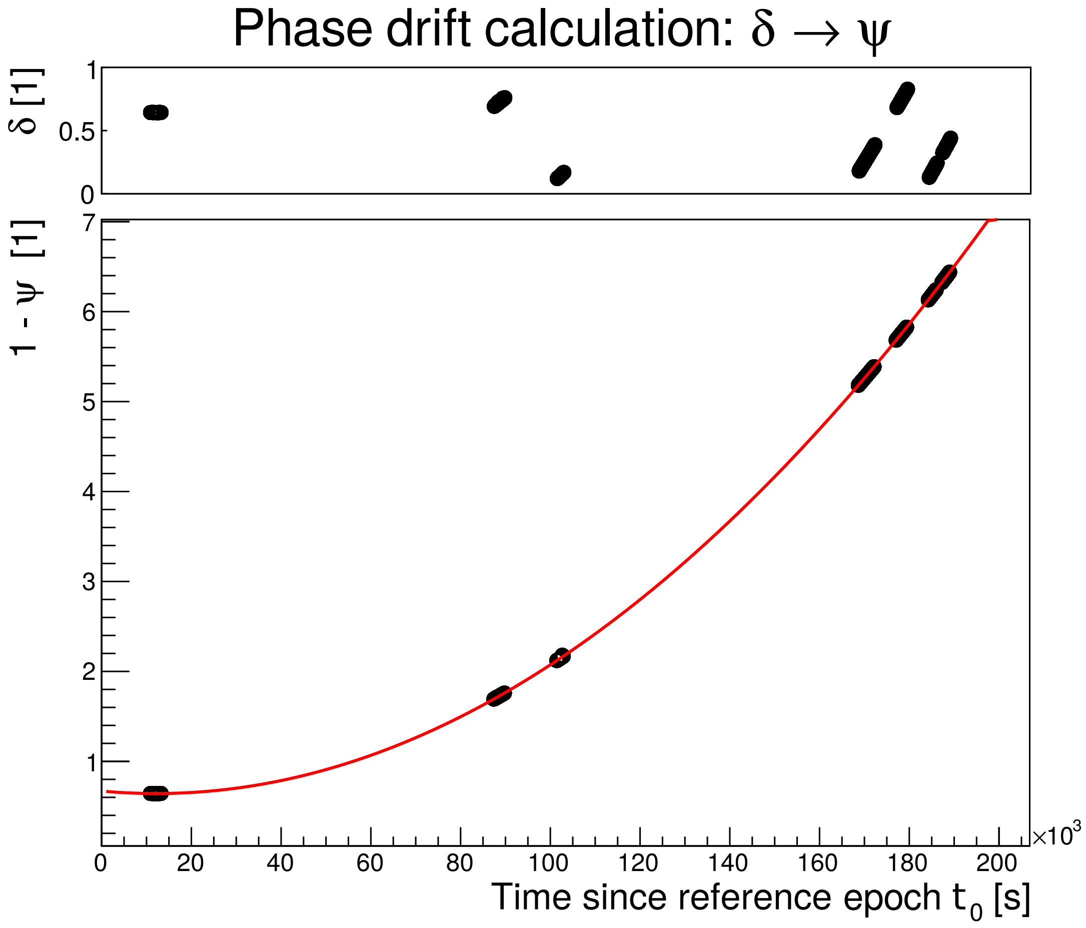

Figure 3.9: Reconstruction of the phase drift ψ starting from the measured peak shift δ. Delta values span the 0–1 interval (upper panel). To obtain ψ values, one has to guess the integer shifts between different acquisitions. In this plot seven separated runs are visible, the last two being almost united in a single one. Each run but the very first is shifted by a trial integer constant: the resulting set $\mathcal{I} = (I_1, I_2, ..., I_6)$ defines a point in the 6-D "index" space of possible translations. Shifted data are linear-fitted with a low-order polynomial: the best fit among different $\mathcal{I}$ is most likely the one with correct shifts. In this plot, the best fit is obtained for $\mathcal{I} = (1, 2, 5, 5, 6, 6)$ and has a χ^2_{red} of 1.8. Even the second best-χ^2 group of indices $\mathcal{I}' = (2, 3, 6, 6, 7, 7)$ gives instead $\chi^2_{red} = 3875.57$, and can thus be rejected.

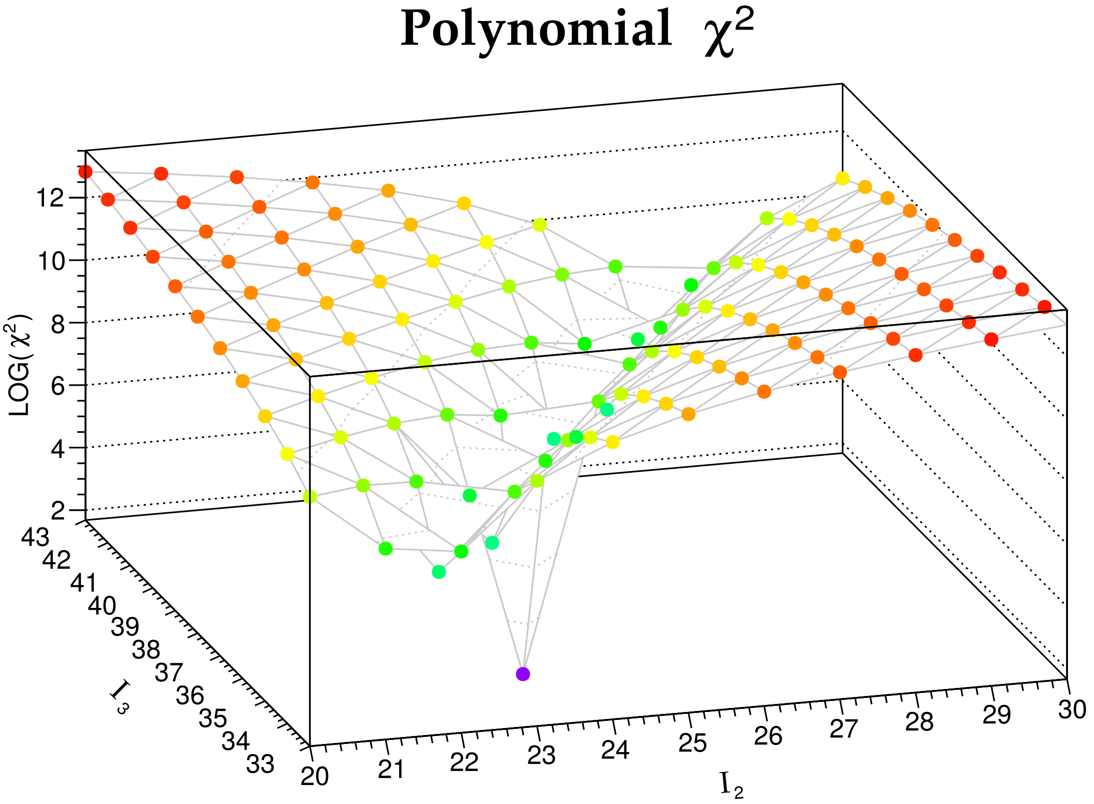

Figure 3.10: Logarithmic plot of χ^2_{red} for a 2-D index space. The best fit corresponds to $\mathcal{I}$ = (24, 37) and has a χ^2_{red} = 1.26 (purple point at the bottom). Other indices give a three orders of magnitude higher value of $\chi^2_{red.}$, at least.

higher order ones only if a clear χ^2 minimum cannot be found; using high ($n \geq 4$) grades may produce better χ^2 values, since the resulting curve can bend more easily to fit the data, but usually corrupts the estimates on lower grade parameters. As a rule, it is thus better to start from a grade 2 polynomial (a parabola) and move to grade 3 only if the fit produces a statistically significant estimate of p_3, and so on for higher grades.

Phase curve determination and radio data comparison By direct comparison between 3.15 and 3.8 it is evident that:

$$\begin{aligned} p_0 &= 1 - \psi_0 \\ p_1 &= \nu_0 - \nu \\ p_2 &= -\dot{\nu}/2 \\ p_3 &= -\ddot{\nu}/6 \\ &\vdots \\ p_j &= -\frac{1}{j!}\frac{d^j\nu}{dt^j} \end{aligned} \tag{3.20}$$

Once the data have been phase-connected it is thus possible to get phisical information on the pulsar's rotation. Using then the temporal gauge definition 3.9 the phase $\varphi(t)$ can finally be determined. This enables us to compare it with radio ephemerides and to determine if a delay in the main pulse arrival time is present.

Global phasing

The method just described is applicable also to try a "global" phasing, i.e. finding a single phase solution for very distant data. In the next chapter, we present a global phase solution for the Crab pulsar from January to October 2012. As already stated at the end of section 3.3.3, in such a case it is impossible to use a single reference frequency ν_0, the variation of the period between January and October being too large. Two different temporal gauges G and G' ought to be used first to fold data separately; once δ values have been obtained for both, it is possible to transform values from gauge $G \leftrightarrow (t, \delta)$ to $G' \leftrightarrow (t', \delta')$ with:

$$\delta' = \mathfrak{F}\left\{\frac{\Delta}{T'_0} + \left\lfloor\frac{t}{T_0}\right\rfloor\frac{T_0}{T'_0} + \delta\frac{T_0}{T'_0}\right\} \tag{3.21}$$

The proof of 3.21 is given in appendix *B*. The phase drift ψ can reach very high values on long interval (in the actual case, ≈ 300 days): it is thus a good idea to find first a local phasing and to deal with the global one as a 1-D problem in a second time.

For a long term phase solution, effects of higher grade terms in Equation 3.15 may be significant. A measure of $\ddot{\nu}$, associated with the third order of the polynomial fit, allows to compute the *braking index n* for the pulsar (see Section 1.3.1). Using 3.20, the braking index itself may be rewritten as:

$$n = \frac{3}{2}\frac{(p_1 + \nu_0)p_3}{p_2^2} \tag{3.22}$$

Chapter 4

Results

This chapter presents the observational data and main results of the analysis. Initial sections are devoted to the characterization of data, while the outcome of phase analysis is discussed in later sections.

4.1 Data

Two observing campaings of the Crab pulsar with AQUEYE were considered in this work. The first took place at the beginning of January 2012 and spanned 6 days of observations.
The latter also covered 6 days in the second half of October 2012, but only in half of them whitelight observations were performed.
Table 4.1 contains basic information which characterize the two sessions. During pre-analysis operations it turned out that the quality of the October observations was much better than the January ones. The reason is clear from Table 4.2, where angular distances from the Sun and the Moon, as well as the mean Moon phase are listed: moonlight background contaminations were much more significant in the January observing run.

Both sessions were done before AQUEYE+ improvements. In the 2012 AQUEYE configuration, only 3 of the 4 SPADs were used to monitor the Crab pulsar, the fourth being devoted to monitor the background. Throughout this chapter, different SPADs will be identified by their acquisition channel number: SPADs 8, 10 and 14 observe the pulsar, while SPAD 12 monitors the background.

$$\left.\begin{array}{c}8\\10\\14\end{array}\right\}\text{On-source}\qquad\qquad \left.\begin{array}{c}12\end{array}\right\}\text{Background}$$

The first pre-analysis steps (calculation of lightcurves and power spectra) have been done both on each single channel SPAD (including the background one) and on data resulting by summing up signals from all on-source SPADs (8+10+14, no background).

Session	Start time	End time	№ obs.	t_{obs} [s]
JAN	04/01/2012 h. 18 30′ 07″ UTC	10/01/2012 h. 00 12′ 52″ UTC	16	65034
OCT	17/10/2012 h. 02 55′ 40″ UTC	19/10/2012 h. 03 54′ 48″ UTC	7	15856

Table 4.1: January and October 2012 observing runs of the Crab pulsar with AQUEYE. October run was actually longer, but only whitelight data are listed here.

Session	α_L	Φ_L	α_S
JAN	33 °– 0.5 °	90%	158 °
OCT	143 °– 173 °	12%	121 °

Table 4.2: Maximum and minimum lunar angular separation during observations, mean lunar phase, mean solar separation. Notice the grazing full Moon during the January session.

Obs. №	Start time	Duration [s]
01	04/01/2012 h. 18 30′ 07″ UTC	3600
02	04/01/2012 h. 19 38′ 14″ UTC	3599
03	04/01/2012 h. 21 24′ 44″ UTC	3600
04	04/01/2012 h. 22 39′ 58″ UTC	3600
05	04/01/2012 h. 23 52′ 39″ UTC	3387
06	05/01/2012 h. 22 05′ 43″ UTC	1390
07	05/01/2012 h. 22 52′ 33″ UTC	2636
08	06/01/2012 h. 00 38′ 10″ UTC	148
09	06/01/2012 h. 00 50′ 54″ UTC	1877
10	08/01/2012 h. 21 27′ 44″ UTC	3599
11	08/01/2012 h. 22 28′ 39″ UTC	7199
12	09/01/2012 h. 00 55′ 36″ UTC	3599
13	09/01/2012 h. 01 58′ 13″ UTC	1803
14	09/01/2012 h. 18 03′ 52″ UTC	9999
15	09/01/2012 h. 21 25′ 11″ UTC	9999
16	10/01/2012 h. 00 12′ 52″ UTC	4999
17	17/10/2012 h. 02 55′ 40″ UTC	2400
18	18/10/2012 h. 00 11′ 03″ UTC	2401
19	18/10/2012 h. 04 04′ 53″ UTC	1500
20	18/10/2012 h. 22 44′ 29″ UTC	3560
21	19/10/2012 h. 01 05′ 06″ UTC	2398
22	19/10/2012 h. 03 04′ 46″ UTC	1798
23	19/10/2012 h. 03 54′ 48″ UTC	1799

Table 4.3: Log of the AQUEYE observations of the Crab pulsar taken in Janualy and October 2012. Red IDs signal observations whose data have been discarded, due to various reasons.

SPAD 8 was off for most of January observations and recorded no data, its temperature being too low to be operational; this had no effect on the analysis (see section 4.2.2).

Table 4.3 reports a log of the observations taken in both January and October. Data from some observations (red) were later rejected, the signal from the Crab pulsar being too noisy or simply absent.

4.2 Pre-analysis

4.2.1 Light-curves

As discussed in Section 3.2, LCs were first created for all data to inspect for long-term variability. A time bin of 1 s was used both for January and October observations. During the same observation, no significant difference is present among the shape of the LC in different channels (though there may be scale factors, due to different channel efficiencies). An exception to this is the already quoted SPAD 8, which was totally off during most of January observations. Tables 4.4 and 4.5 list the main statistical parameters for each LC, and figure 4.1 shows some typical lightcurves.

Lighcurves from January exibit highly irregular trends with sudden flux variations, flickering, off periods. This can be deduced also by values listed in Table 4.4: mean fluxes considerably vary from one observation to the next, LC standard deviation is high and reduced χ^2 values for both a constant and a linear interpolation are huge. In fact, the notes in the observing logs for January state that weather was extremely variable, with hazes and groups of clouds constantly passing on. Observation number 8 started with SPAD 12 off and was immediately stopped. Since in the folded LC background variations only contribute adding an offset to the pulse profile, power spectra computation and phase analysis have been carried on despite these facts.

On the other hand, October LCs are extremely stable. Only observation 18 was affected by the passage of a cloud, while observations 19 and 23 show minor flux increases due to brightening sky near dawn time. Reduced chi-squares of the linear fit indeed indicate that minor variabilities due to wheather are present, even if they are hardly visible (see figure 4.1).

Lighcurves analysis indicate thus that October observations are little affected by long term variabilities, whether January obes show many long term irregularities. At this point, nothing can be said about relative signal strenghts, but January observations are expected to be somewhat more noisy.

Obs. №	**Duration [s]**	F **[10^4 ph./s]**	σ **[ph./s]**	$\chi^2_{const.}$	χ^2_{lin}	**Notes**
01	3598	1.07	$3.66 \cdot 10^2$	$1.2 \cdot 10^1$	$2.4 \cdot 10^0$	Regular
02	3597	1.42	$5.77 \cdot 10^3$	$2.0 \cdot 10^3$	$8.3 \cdot 10^2$	
03	3598	1.07	$3.29 \cdot 10^3$	$6.5 \cdot 10^2$	$4.2 \cdot 10^2$	
04	3598	0.37	$8.39 \cdot 10^2$	$3.3 \cdot 10^2$	$1.8 \cdot 10^2$	
05	3385	2.93	$2.16 \cdot 10^3$	$1.8 \cdot 10^2$	$1.7 \cdot 10^2$	
06	1388	0.49	$5.94 \cdot 10^3$	$2.2 \cdot 10^6$	$4.8 \cdot 10^3$	
07	2634	1.60	$6.10 \cdot 10^3$	$1.0 \cdot 10^3$	$9.4 \cdot 10^2$	
08	148	—	—	—	—	SPAD off
09	1875	1.67	$3.94 \cdot 10^2$	$4.2 \cdot 10^1$	$4.4 \cdot 10^1$	
10	3597	2.80	$2.78 \cdot 10^3$	$2.4 \cdot 10^2$	$2.4 \cdot 10^2$	Dome refl.
11	7197	3.08	$5.40 \cdot 10^3$	$8.2 \cdot 10^2$	$7.8 \cdot 10^2$	Dome refl.
12	3597	4.40	$7.10 \cdot 10^3$	$1.3 \cdot 10^3$	$1.3 \cdot 10^3$	Dome refl.
13	1801	4.33	$7.02 \cdot 10^3$	$1.2 \cdot 10^3$	$1.1 \cdot 10^3$	Dome refl.
14	9997	4.29	$4.19 \cdot 10^4$	$3.7 \cdot 10^4$	$1.8 \cdot 10^4$	
15	9997	1.66	$7.55 \cdot 10^3$	$1.2 \cdot 10^3$	$1.1 \cdot 10^3$	
16	4997	1.74	$6.45 \cdot 10^2$	$2.4 \cdot 10^1$	$4.4 \cdot 10^0$	Regular

Table 4.4: LC properties for the January session. These LCs have been generated from the data of a single SPAD (12, the background one): the reason for this will be given in section 4.2.2. During the very short RUN 8, SPAD 12 was off. Notice the high and highly variable mean fluxes F and standard deviations σ and the huge reduced χ^2 for both a constant and a linear fit. This indicates that there was very variable and poor weather conditions during the observations.

Obs. №	**Duration [s]**	F **[10^4 ph./s]**	σ **[ph./s]**	$\chi^2_{const.}$	χ^2_{lin}	**Notes**
17	2399	1.54	$3.70 \cdot 10^2$	$8.8 \cdot 10^0$	$4.46 \cdot 10^0$	
18	2399	1.46	$1.37 \cdot 10^3$	$1.7 \cdot 10^2$	$1.54 \cdot 10^2$	Cloud
19	1500	1.62	$1.56 \cdot 10^3$	$1.4 \cdot 10^2$	$3.90 \cdot 10^1$	Dawn
20	3560	1.57	$3.17 \cdot 10^2$	$6.5 \cdot 10^0$	$4.85 \cdot 10^0$	
21	2398	1.55	$2.16 \cdot 10^2$	$3.0 \cdot 10^0$	$3.36 \cdot 10^0$	
22	1798	1.53	$3.17 \cdot 10^2$	$6.6 \cdot 10^0$	$6.83 \cdot 10^0$	
23	1799	1.70	$7.52 \cdot 10^2$	$3.1 \cdot 10^1$	$1.18 \cdot 10^1$	Dawn

Table 4.5: LC properties for the October session. These LCs have been generated from the whole on-source data (8+10+14). Notice the rather stable mean flux F. Standard deviation is $\simeq 300$ and takes higher values for observations near sunrise (19, 23) and for observation 18, during which a cloud passed over. χ^2 values are much smaller than for January, but still above hypotesis rejection threshold: this likely indicates that indeed smaller sky and airmass variations were present.

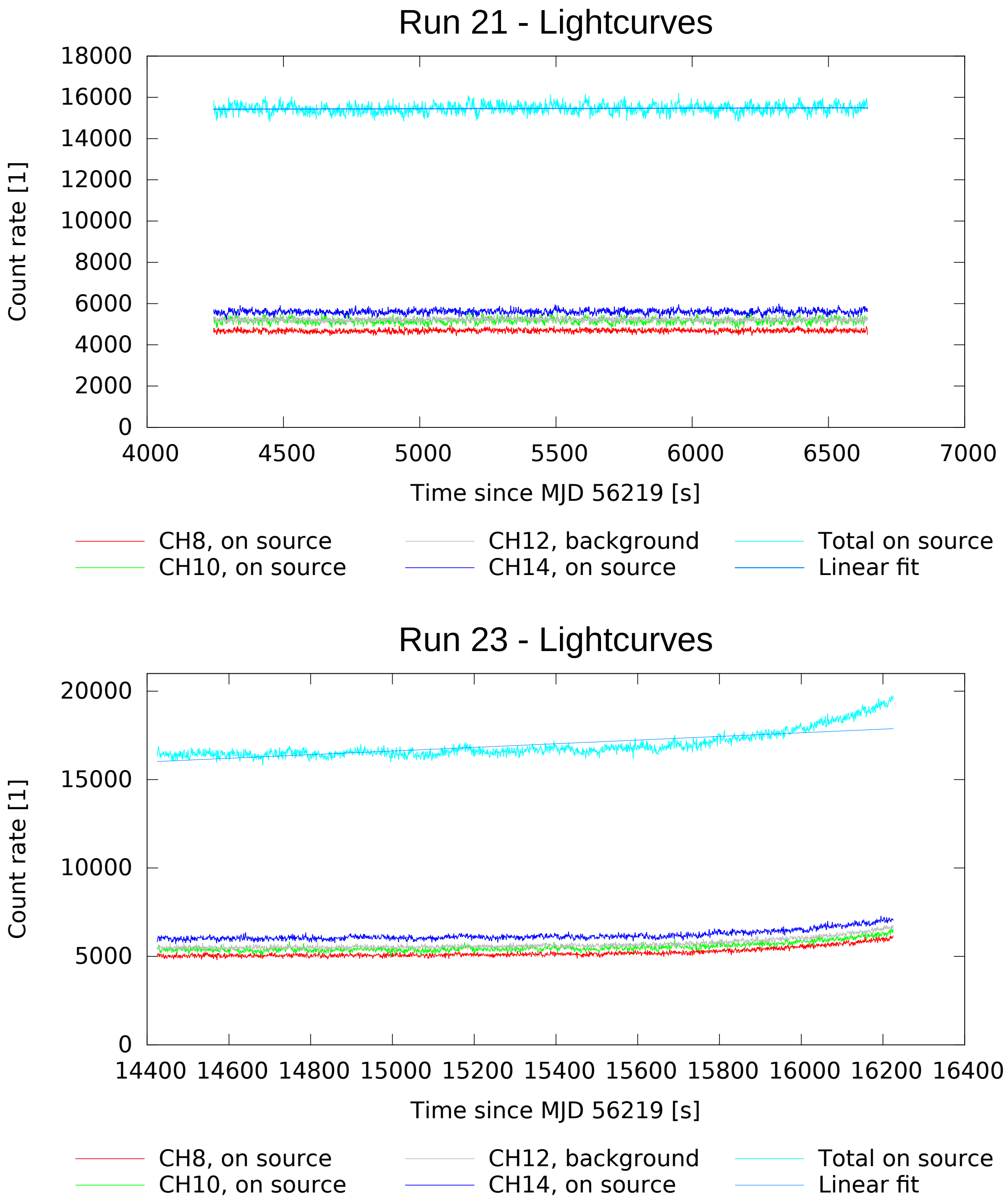

Figure 4.1: LCs for observations 21 and 23. These are both October observations and exibit rather stable LCs; the exponential growth starting at about $t = 15400\,\mathrm{s}$ in the bottom panel is caused by sky getting brighter and brighter due to upcoming sunrise.

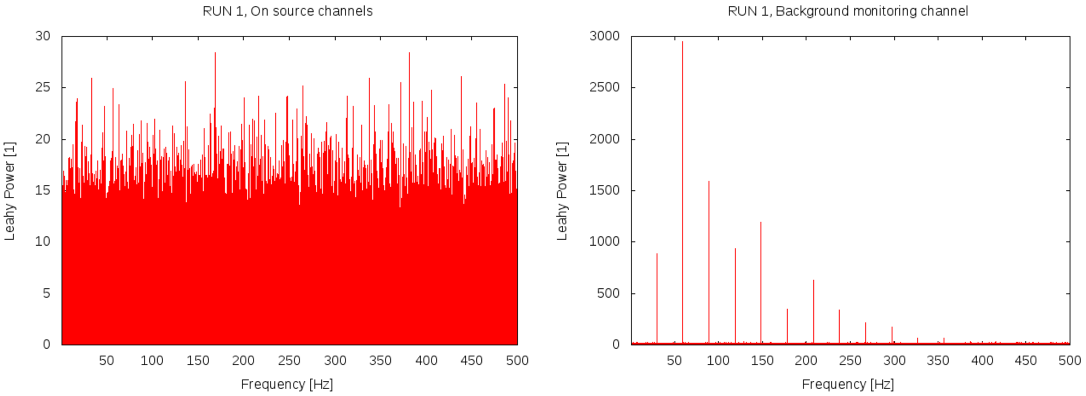

Figure 4.2: Power spectra for observation 1 (January). The intended on-source channels contain no signal, whether the background channel 12 shows a power spectrum with 14 harmonics, associated with the Crab pulsar. This was caused by a small pointing error.

4.2.2 Power spectra

Power spectra allow the study of short term variability, such as the one caused by the Crab pulsar's signal. Main values characterizing power spectra for all observations are listed in Tables 4.6 and 4.7. Power spectra analysis for the January and October sessions are separately discussed in the next paragraphs.

January Power Spectra

The computation of power spectra for the January observations immediately highlighted that on-source SPADs 10 and 14 registered no signal from the pulsar (SPAD 8 was off). The sum of on source channels also showed no evidence for signal, but surprisingly the background monitoring SPAD 12 registered photons from the pulsar (see Figure 4.2). This was interpreted as a result of a small pointing error: January data where taken with grazing full Moon, which made visualising the pulsar for pointing difficult. The pulsar was targeted by first pointing a nearby brighter star and then specifying a coordinate offset measured in previous observations. This procedure did not eventually grant sufficient precision, but the small misalignment resulted in the background SPAD detecting pulsar light. All analysis on January observations has been performed on the SPAD 12 data alone, including power spectra and former lightcurves calculations.

Table 4.6 lists power spectra quantities for January observations: power associated with the fundamental frequency P_1; power of the most powerful higher harmonic P_{max}; average power $P_{avg.}$ above 1 Hz; probability that white-noise alone produces a line as strong as the fundamental harmonic p_w; number of visible harmonics L.

Obs. №	P_1 [1]	P_{max} [1]	$P_{avg.}$ [1]	p_w	L
01	886	2953	2.07	0	14
02	556	1987	2.06	0	13
03	486	3538	2.07	0	14
04	17	—	2.06	$2{\cdot}10^{-4}$	1
05	35	40	2.06	$3{\cdot}10^{-8}$	4
06	17	—	2.06	$2{\cdot}10^{-4}$	1
07	365	1788	2.06	0	12
08	—	—	—	—	—
09	12	—	2.06	$2{\cdot}10^{-3}$	1
10	294	1018	2.06	0	12
11	756	2267	2.06	0	14
12	101	660	2.05	0	10
13	98	282	2.05	0	7
14	189	637	2.07	0	12
15	1984	4590	2.07	0	16
16	820	2595	2.06	0	16

Table 4.6: Power spectra parameters for the January observations, initial binning time t_{bin} = 1 ms, Nyquist frequency ν_N = 500 Hz. Listed values are: the fundamental harmonic (i.e. 29.7 Hz) Leahy power P_1; the maximum spectral power P_{max}, if associated with a higher harmonic; average power $P_{avg.}$ above 1 Hz; the probability p_w that the fundamental harmonic line is produced by white noise alone; the number of detected harmonics L.

Obs. №	P_1 [1]	P_{max} [1]	$P_{avg.}$ [1]	L
17	22822	206506	2.20	46
18	19602	94061	2.14	43
19	7869	64028	2.12	38
20	22669	74006	2.11	38
21	26350	214059	2.21	47
22	23907	69757	2.15	41
23	24384	189700	2.24	45

Table 4.7: Power spectra parameters for the October observations, initial binning time t_{bin} = 250 μs, Nyquist frequency ν_N = 2000 Hz. Same variables as in Table 4.6, except for the white noise probabilities which have been omitted, being all zero. Notice the very strong signal power and the high number of visible harmonics.

We note that:

- $P_{avg.}$ values are all close to 2, the pure white noise prediction. This confirms that the Leahy-nomalized power spectrum contains only stochastic noise but for the pulsar signal, which accounts for the $\gtrsim 2$ trend.

- P_1 values vary much among observations, ranging from 10 to 2000; $P_{max} = P_2$ values, which are associated with the second harmonic, are always greater than P_1: this is an expected behaviour, since the pulse profile of the Crab pulsar is markedly double peaked with a strong interpulse. Higher P_1 values correspond to higher P_2 values and a global proportionality with wide oscillations is visible.

- $p_w = \exp(-P_1/2)$ is null but for four observations, for which few or no higher harmonics are visible in. Observations 4, 6 and 9 have $L = 1$: this indicates that signal was too noisy to solve major features such as the interpulse. Quality of these observations is judged too low to proceed with further analysis. During obs. 8, SPAD 12 was off and no data was detected. Run 5 is at rejection theshold (only 4 lines are visible), but phase analysis was tried anyhow. All other observations exibit good signal ($L \simeq 7$–16) and are accepted for phase analysis.

October power spectra

Table 4.7 lists parameters of the power spectra of the October campaing observations. White noise probability has been omitted, since it is null. In this case, all the on-source SPADs registered very good and equal strenght signal, while the background SPAD showed no trace of signal. We note that:

- $P_{avg.}$ is still close to 2, but higher values, due to higher harmonic powers, are reached.

- P_1 and P_{max} values are all much greater than January ones (from 10 to 100 times). This indicates that data contain much more signal than January observations and enable phase analysis to be carried on shorter intervals.

- The number of visible harmonics L is much higher than in January. Some observations show harmonics up to the 53^{rd}. This yields higher accuracy determining both major and minor features of the pulse profile.

Given these results, all October observations have been accepted for phase analysys. Figure 4.3 shows a typical power spectrum from October observations (obs. 21).

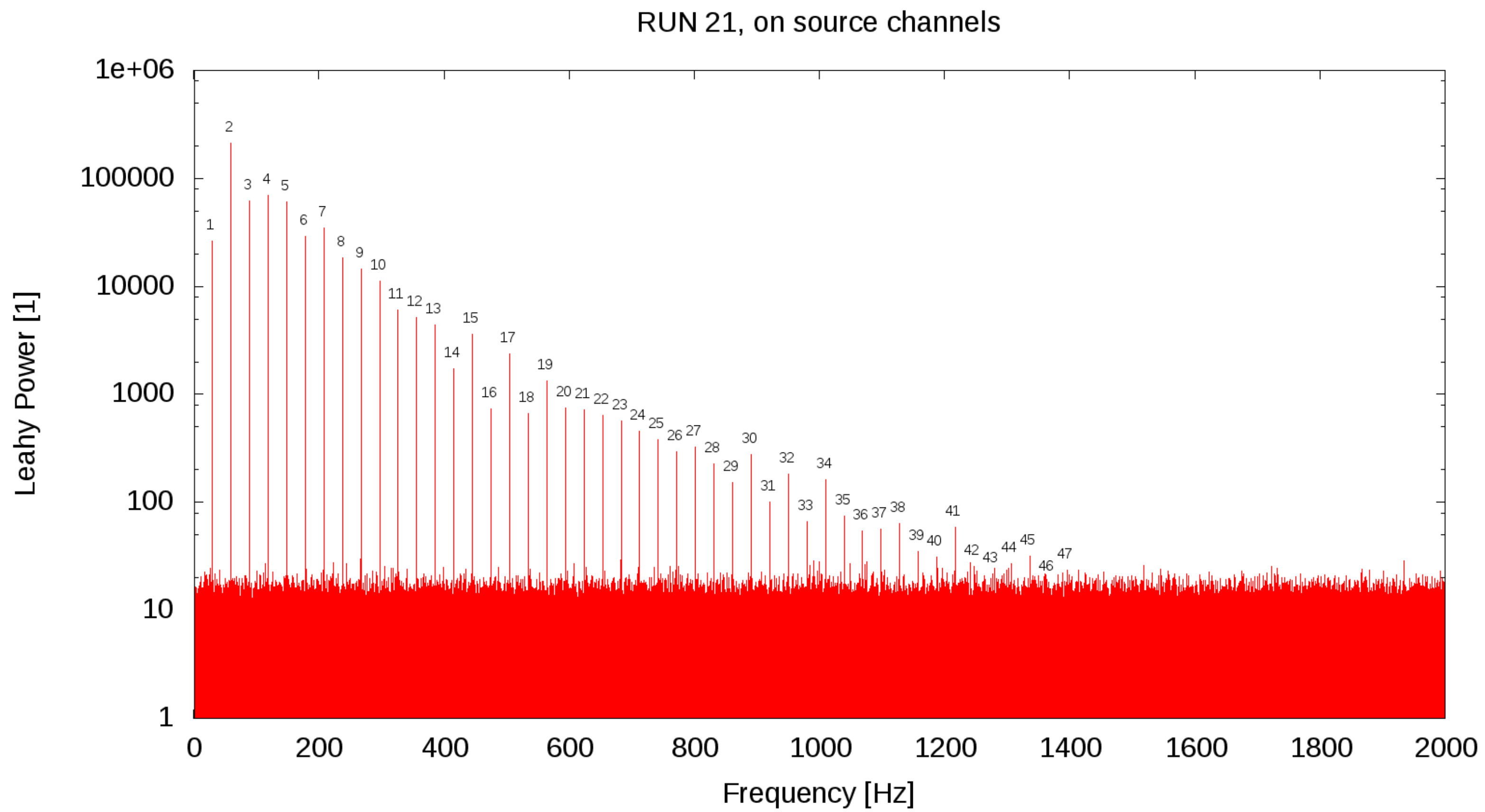

Figure 4.3: Log power spectrum of observation 21 (October). Up to 42 lines are directly visible, 5 more lines can be seen enlarging the scale. Pulsar harmonics are labelled with harmonic number. The maximum frequency (Nyquist frequency) is set by the binning time of the lighcurve which this spectrum was extracted from, $\nu_N = 2\,\text{kHz}$. Frequency resolution is $4.2 \cdot 10^{-4}$ Hz.

4.3 Phase Analysis results

4.3.1 January data

As explained in Section 3.3, a high precision period measure is required for folding: a 10 ps EFS procedure with parabolic fit around maximum has been used on data of obs. 1 for deriving a suitable estimate T_0 to be used with January data with sub-picosecond uncertainty. The folding reference epoch t_0 was taken at midnight of the first day of observations (04/01/2012, MJD 55930).

t_0 [MJD]	T_0 [s]
55930	0.0336645097842

Table 4.8: Temporal gauge for January data folding.

Some folding trial initial configuration were tested in order to optimize the S/N ratio for fitting the peak profile. Finally a folding period $t_{fold} = 32$ s and a number of phase bins $N_\phi = 128$ was selected. These values agree with equation 3.14 (see also Appendix D). Further increasing t_{fold} results in a proportional reduction of N_ϕ, which is already the minimum value required to garantee a sufficiently accurate resolution of the pulse profile. On the other hand, reducting t_{fold} would not grant sufficient statistics. Figure 4.4 shows a typical January folded lightcurve fit.

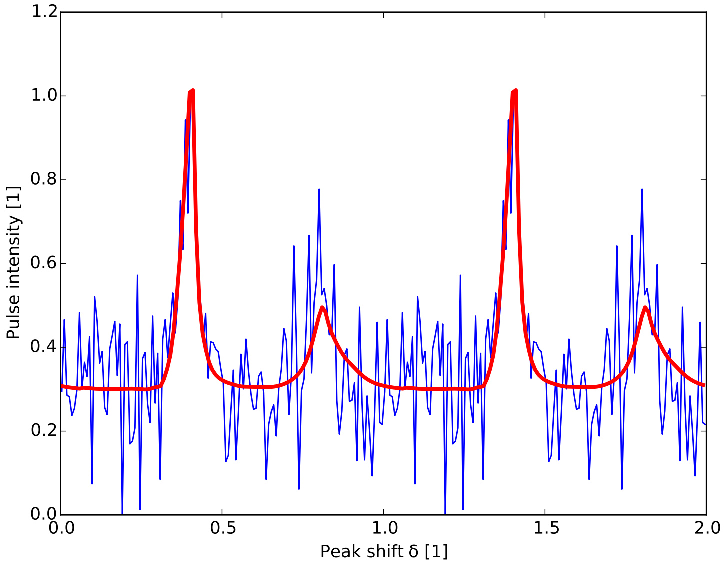

Figure 4.4: Lighcurve for a 32 s folded interval and pulse profile fit. The lightcurve has been repeated twice for clarity. Main pulse and interpulse are both resolved. The fit gives $\delta = 0.406 \pm 0.002$ and a reduced chi-square of 0.74.

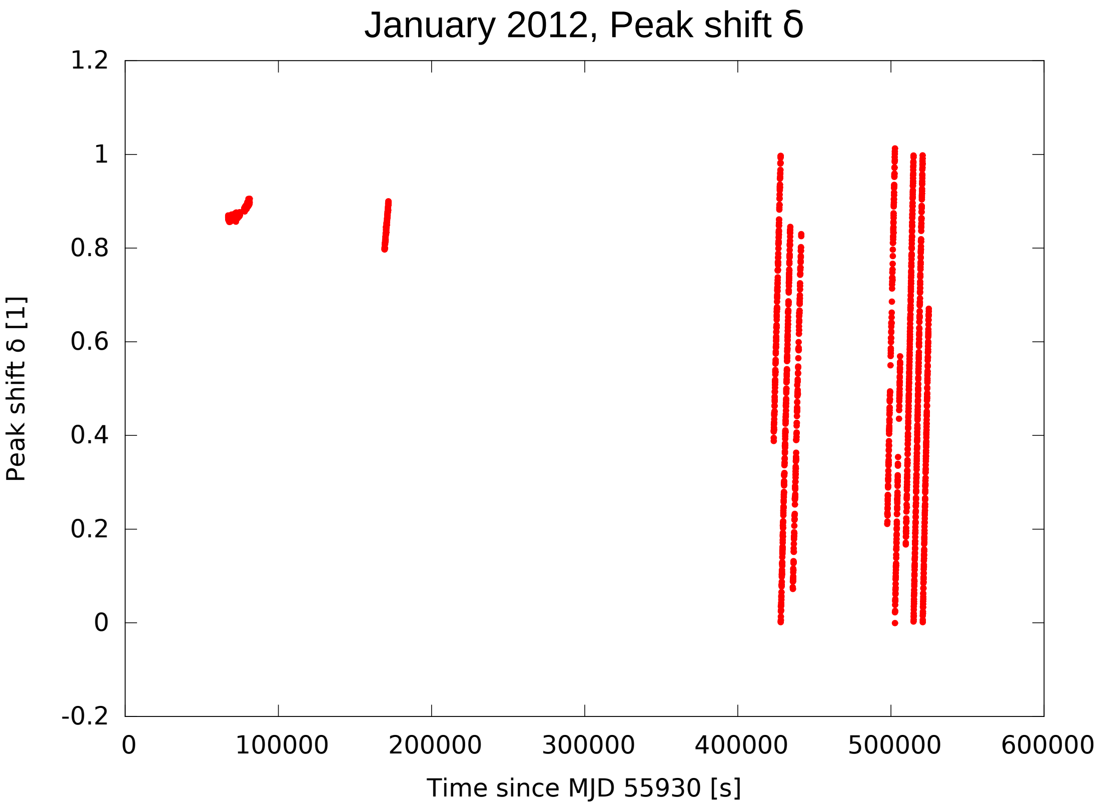

Figure 4.5: Peak shift δ in January, measured in 32 s folded intervals.

January Phase Solution

The folded lightcurve fits give the peak shift δ vs. time. As discussed in Section 3.3.4, January data were very noisy and required a cleaning process to be usable. The cleaning removed outliers with high accuracy; data from obs. 5, which were on rejection threshold after power spectral analysis (only 4 harmonics visible), were all removed at this stage by the cleaning algorithm. This indicates that a minimum number of $\simeq 7$ visible harmonics or a fundamental harmonic power of 100 at least in the Leahy nomalized power-spectrum is needed for phase analysis. Peak shift δ for January data is plotted against time in Figure 4.5. Initial data at $t' = t - t_0 = 65000$ show the beginning of the drift as a second order (parabolic) effect; once a sensible period difference dT has been produced, at each cycle the main peak shifts by dT/T_0: as a result at later times δ spans the whole (0–1) interval (see section 3.3.3).

To obtain $\psi(t')$ one has to reconstruct the integer part of the peak shift (see Section 3.3.4). Guessing the shifts to be applied at discontinuities which occur during an observation is trivial, while a polynomial fit chisquare minimization process is required to recover

Obs. №	Integer shift I
1–3	0
7	+2
10–13	+24
14	+35
15–16	+37

Table 4.9: Integer shifts among January obs. giving the best-χ^2 parabolic fit.

Parameter	Value		
t_0	55930		MJD
ν_0	29.704873533		Hz
p_0	1.6982(3)		
p_1	−2.4898(4)	$\cdot 10^{-5}$	Hz
p_2	1.85393(6)	$\cdot 10^{-10}$	Hz^2

Table 4.10: Temporal gauge and best fit parameters of the phase drift. Parameters are defined in Section 3.3.4. №: 1509, $\chi^2_{red.} = 1.52$.

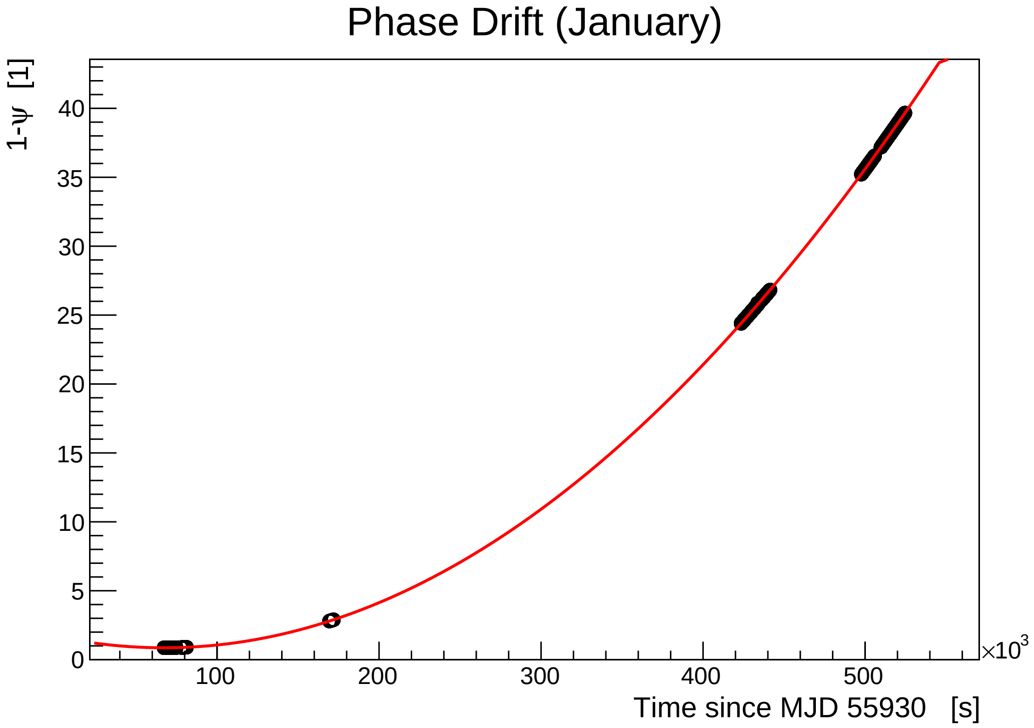

Figure 4.6: Phase drift during the January session. Single data points are undistinguishable on this scale; the global best-χ^2 fit, whose parameters are is Table 4.10, is plottet as a red curve. Reduced χ^2 for this fit is 1.52.

shifts occurring among different observations. Such a procedure was carried out on January data, assuming a second order polynomial behaviour. The observations involved where № 1–3, 7 and 10–16. Table 4.9 lists the integer shift for each observation resulting in the overall best reduced χ^2, while the best fit parameters are reported in Table 4.10. The opposite of phase drift $\psi(t')$ is plotted in Figure 4.6.

The distribution of phase fit residuals was histogrammed to better study it. The overall

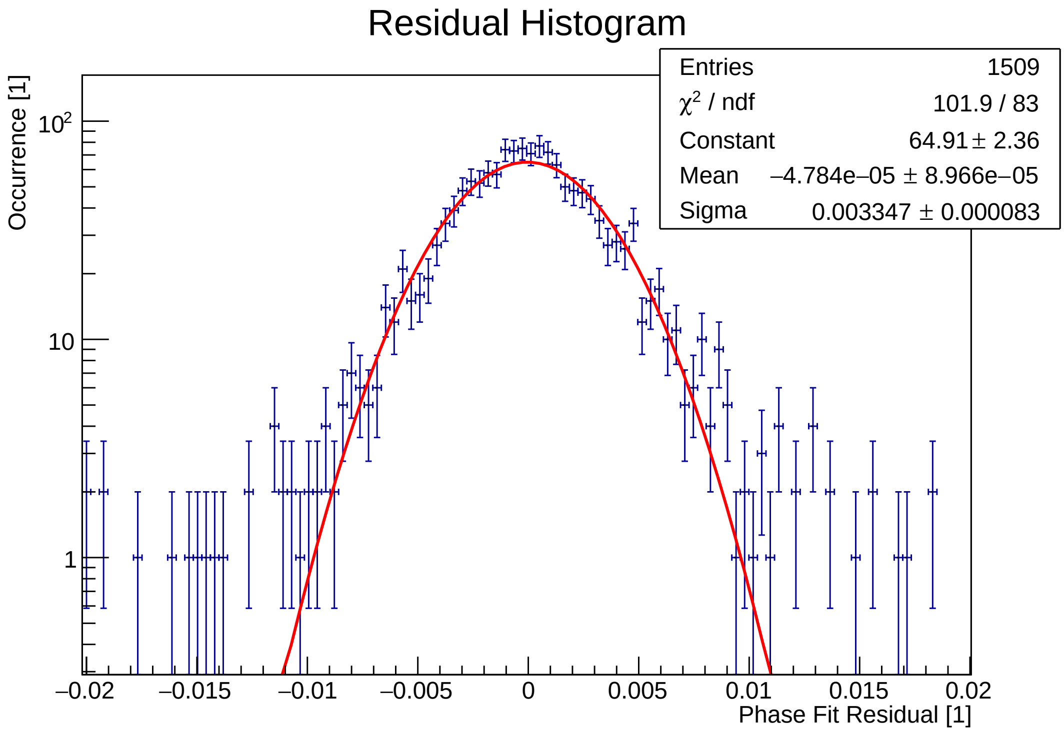

Figure 4.7: Phase fit residuals for January data, on log scale. The overall distribution is well-approximated by a gaussian curve with a phase dispersion of $\sigma = 3.35(8) \cdot 10^{-3}$. The reduced chisquare for a gaussian fit is 1.23. Points on the tails are likely related to more noisy obervations. The fit function is: $c \cdot \exp[-(x-m)^2/(2\sigma^2)]$.

distribution is a gaussian with a reduced $\chi^2_{red.} = 1.23$: this indicates that fluctuations are likely to be attributed to random timing noise alone. Even if very few significance may be attributed to the tails, data appear to be above the fitting gaussian. This is probably caused by the data of more noisy observations, which exibit a broader distribution and are stacked with lesser noisy ones.

Using relations 3.20, it is possible to draw a first estimate of the Pulsar's physical parameters (i.e. ν, $\dot{\nu}$) from the best fitting parameters of the phase drift in Table 4.10. These values are listed in table 4.11.

$$\underline{\textbf{January data}} \begin{cases} t_0 & = & 55930 & \text{MJD} \\ \nu(t_0) & = & 29.704898430(4) & \text{Hz} \\ \dot{\nu}(t_0) & = & -3.7079(1) \cdot 10^{-10} & \text{Hz}^2 \end{cases}$$

Table 4.11: Pulsar's physical parameters drawn from January phase solution.

4.3.2 October data

The same phase analysis workflow adopted for January data was later used to analyse also the October observations. Since the pulsar's signal is much stronger in these, the analysis could be carried out at a higher resolution. A reference period T_0, very close to that of the pulsar at the beginning of the October run, was estimated with an EFS procedure analogue to the one adopted for January data. The reference time t_0 was taken at midnight of the first day of October observations. The resulting temporal gauge is described in Table 4.12.

t_0 [MJD]	T_0 [s]
56217	0.0336749051203

Table 4.12: Temporal gauge for October data folding.

October data were folded using a period $t_{fold} = 8$ s, since such a short interval already permitted a clear resolution of the main pulse and interpulse. Each folded lightcurve consist of $N_\phi = 512$ phasebins.

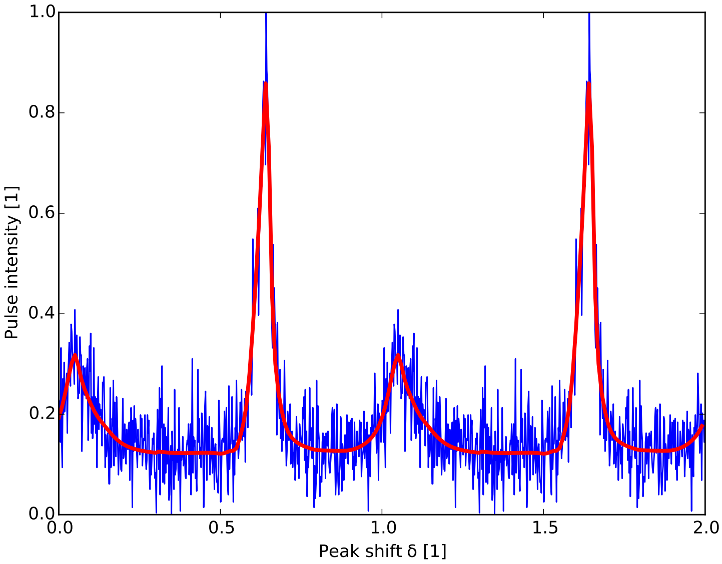

Figure 4.8: Lighcurve for a 8 s folded interval and pulse profile fit. Both the main pulse and the interpulse are clearly resolved. The fit gives $\delta = 0.6430 \pm 0.0004$ and a reduced chi-square of 1.05. This plot should be compared with Figure 4.4 to appreciate data quality differences.

October Phase solution

Figure 4.9 plots the estimated peak shift δ vs. time. For these observations no data cleaning procedure was needed, the main pulse being always well-resolved. The integer shifts applied to δ-curve segments are listed in Table 4.13, while the best polynomial fit parameters are reported in Table 4.14; a parabola was used as fitting function, as no higher order derivative contribute significantly on a 3 days interval.

The phase drift ψ as a function of $t' = t - t_0$ is plotted in Figure 4.10, together with phase fit residual distribution in Figure 4.11. The higher overall quality of October data is also noticeable in the latter plot, which shows a narrower gaussian distribution than

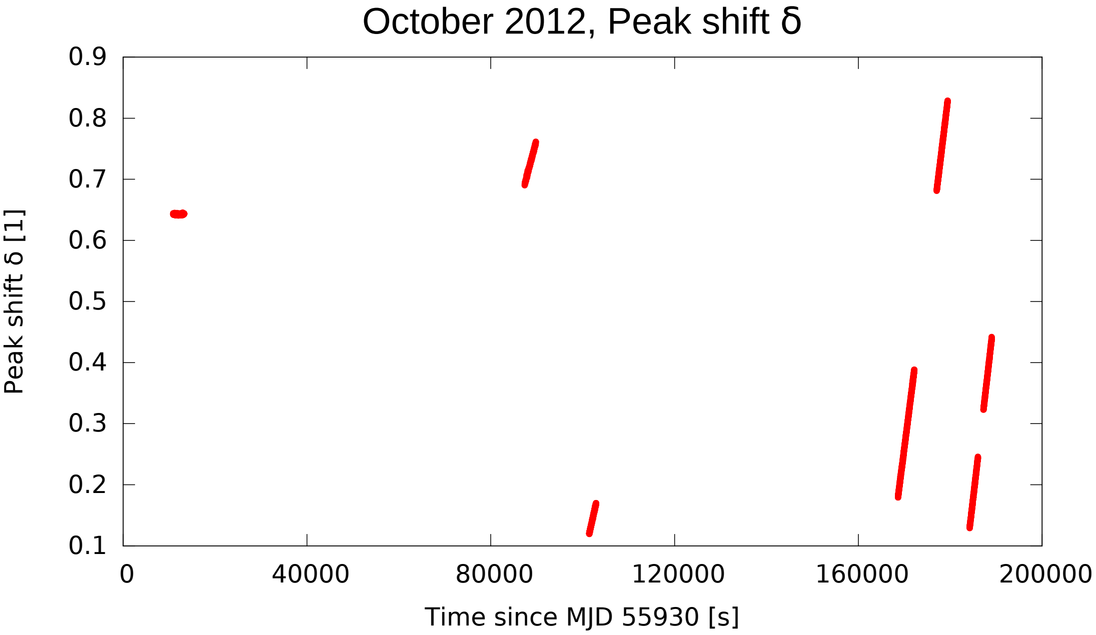

Figure 4.9: Peak shift δ in October observations mesured in 8 s folded intervals.

Obs. №	Integer shift I
17	0
18	+1
19	+2
20–21	+5
22–23	+7

Table 4.13: Integer shifts among October obs. giving the best-χ^2 parabolic fit.

Parameter	Value		
t_0	56217		MJD
ν_0	29.695703564		Hz
p_0	6.7004(4)	$\cdot 10^{-1}$	
p_1	−4.494(1)	$\cdot 10^{-6}$	Hz
p_2	1.85250(5)	$\cdot 10^{-10}$	Hz^2

Table 4.14: Temporal gauge and best fit parameters of the phase drift. Parameters are defined in Section 3.3.4. №: 1982, $\chi^2_{red.} = 1.82$.

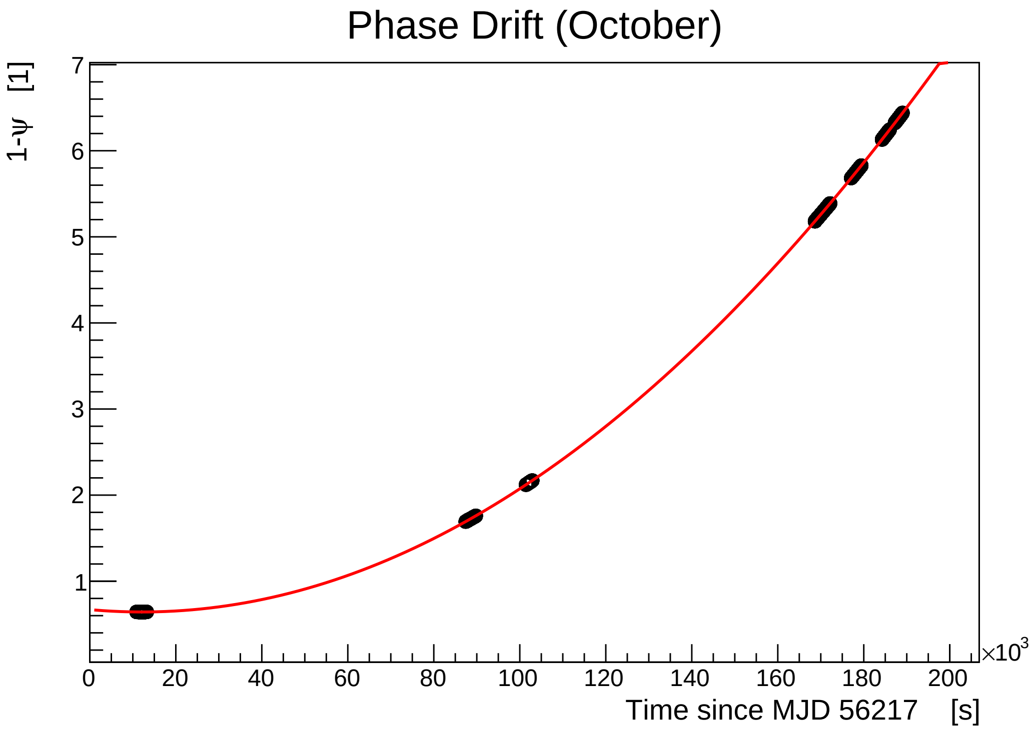

Figure 4.10: Phase drift during the October session. Single data points are undistinguishable on this scale; the global best-χ^2 fit, whose parameters are is Table 4.14, is plottet as a red curve. Reduced χ^2 for this fit is 1.82.

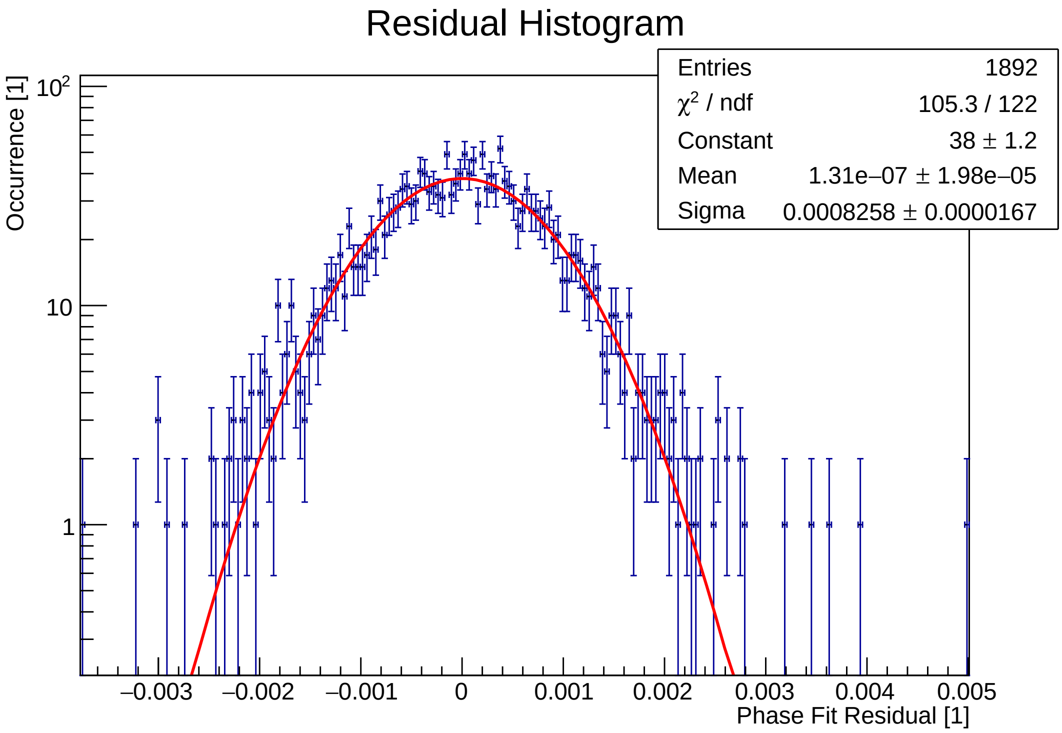

Figure 4.11: Phase fit residuals for October data, on log scale. The overall distribution is well-approximated by a gaussian curve with a phase dispersion of $\sigma = 8.2 \pm 0.2 \cdot 10^{-4}$. The reduced chisquare for a gaussian fit is $\chi^2_{red} = 0.86$. The fit function is: $c \cdot \exp[-(x-m)^2/(2\sigma^2)]$.

the January one ($\sigma_{OCT} \simeq 8.2 \cdot 10^{-4}$ vs. $\sigma_{JAN} \simeq 3.3 \cdot 10^{-3}$) and a well-behaved distribution of the tails.

Finally, one can estimate the pulsar's physical parameters for October 2012 from the best-fit parameters of the phase drift in Table 4.14. These values are given in Table 4.15.

$$\underline{\textbf{October data}} \begin{cases} t_0 & = & 56217 & \text{MJD} \\ \nu(t_0) & = & 29.695708058(1) & \text{Hz} \\ \dot{\nu}(t_0) & = & -3.7050(1) \cdot 10^{-10} & \text{Hz}^2 \end{cases}$$

Table 4.15: Pulsar's physical parameters drawn from October phase solution.

4.4 Global 2012 phase solution

Using equation 3.21, it is possible to refer the measured October's peak shift in figure 4.9 to the same temporal gauge used for January, thus making a global polynomial fit of 2012 data possible. After the temporal gauge transformation, integer shifts among October observations have to be redetermined: October phase fit is plotted in Figure 4.12. The integer shifts giving the best fit in the new temporal gauge and best fit results are listed in Tables 4.16 and 4.17, respectively. The integer shifts among observations

Obs. №	Integer shift *I*
17	0
18	+702
19	+832
20	+1451
21	+1529
22	+1595
23	+1623

Table 4.16: Integer shifts among October observations giving the best-χ^2 parabolic fit in the January temporal gauge. Values are high, being the January reference frequency far from the October one.

Parameter	Value		
t_0	55930		MJD
ν_0	29.704873533		Hz
p_0	−1.1346(3)	$\cdot 10^{5}$	
p_1	−2.25(2)	$\cdot 10^{-5}$	Hz
p_2	1.85261(5)	$\cdot 10^{-10}$	Hz^2

Table 4.17: Best fit of the October data in the January temporal gauge. Parameters are defined in Section 3.3.4. №: 1982, $\chi^2_{red.} = 1.86$.

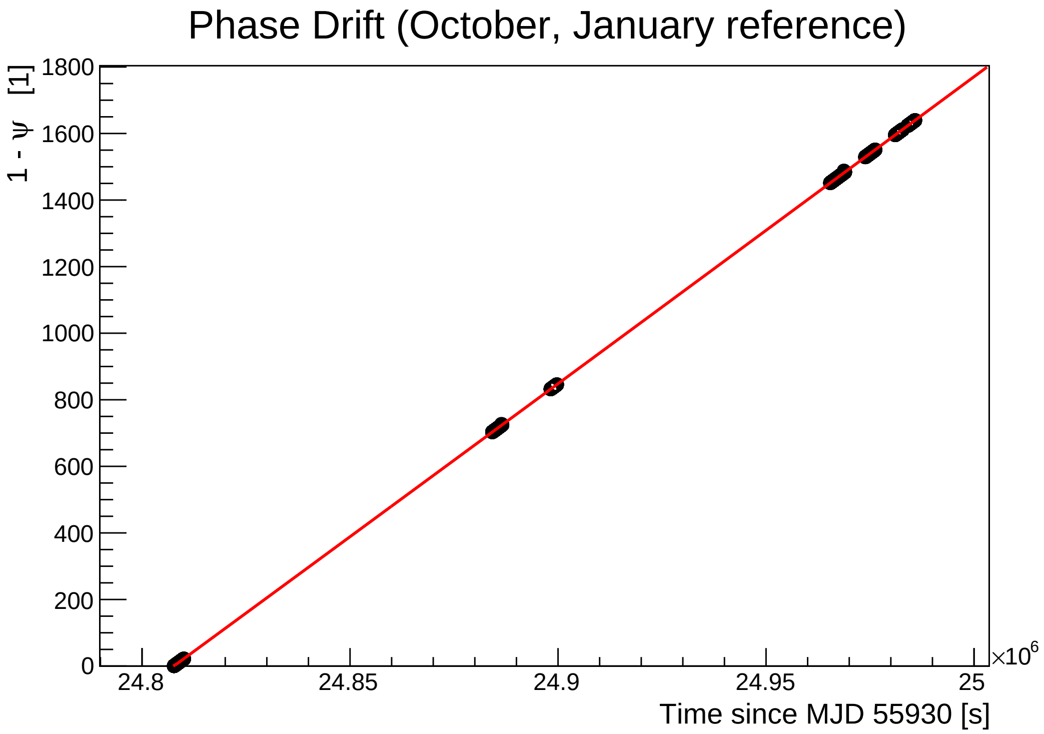

Figure 4.12: Phase drift during the October session in the January time reference. Single data points are undistinguishable on this scale; the global best-χ^2 fit, whose parameters are reported in Table 4.17, is plottet as a red curve. Reduced χ^2 for this fit is 1.86.

are in this case much higher. This is due to the reference period being the one of January, which is significantly different from the actual pulsar period in October. Because of this, the phase drift evolves much faster and folding October data directly in the January temporal gauge would result in unusable data.

The integer part of the phase drift between January and October data was determined just as the drifts among observations, using global χ^2 minimization. The time interval encompassed by data is about 300 d, which is long enough for a third grade polynomial fit to be adopted.

A cubic fit was perfomed: the best fit is obtained with a shift $\mathcal{I} = 113443$: this means that the pulsar's phase drifted from January to October by $\simeq 113442$ cycles with respect to a uniform rotator. Fit results are given in table 4.18, while plots of the fit and of fit residuals are in Figures 4.13 and 4.14. Residuals do not follow a normal distribution, being rather distributed as the sum of two different gaussians, which have a standard deviation of $\sigma_1 = (3.6 \pm 0.1) \cdot 10^{-3}$ and $\sigma_2 = (8.5 \pm 0.3) \cdot 10^{-4}$, respectively. These value are in good agreement with the standard deviations obtained from local October and January residual fits, $\sigma_{JAN} = (3.35 \pm 0.08) \cdot 10^{-3}$ and $\sigma_{OCT} = (8.3 \pm 0.2) \cdot 10^{-4}$, their compat-

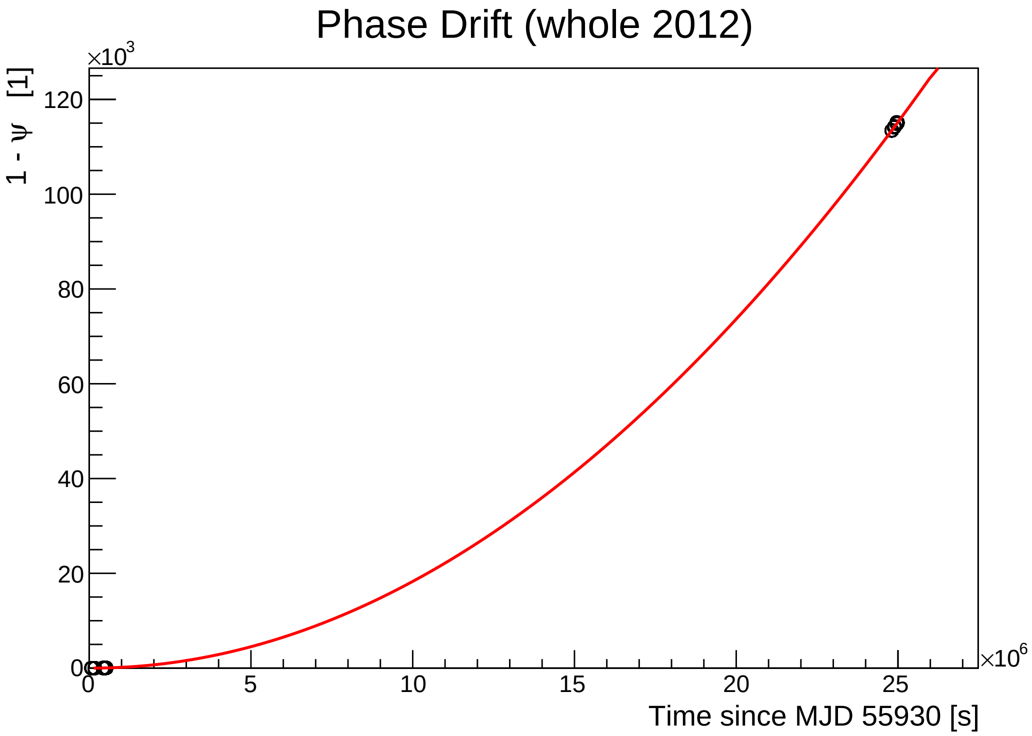

Figure 4.13: Phase drift in the whole year 2012 and corresponding cubic fit. Individual observations are not visible on this scale.

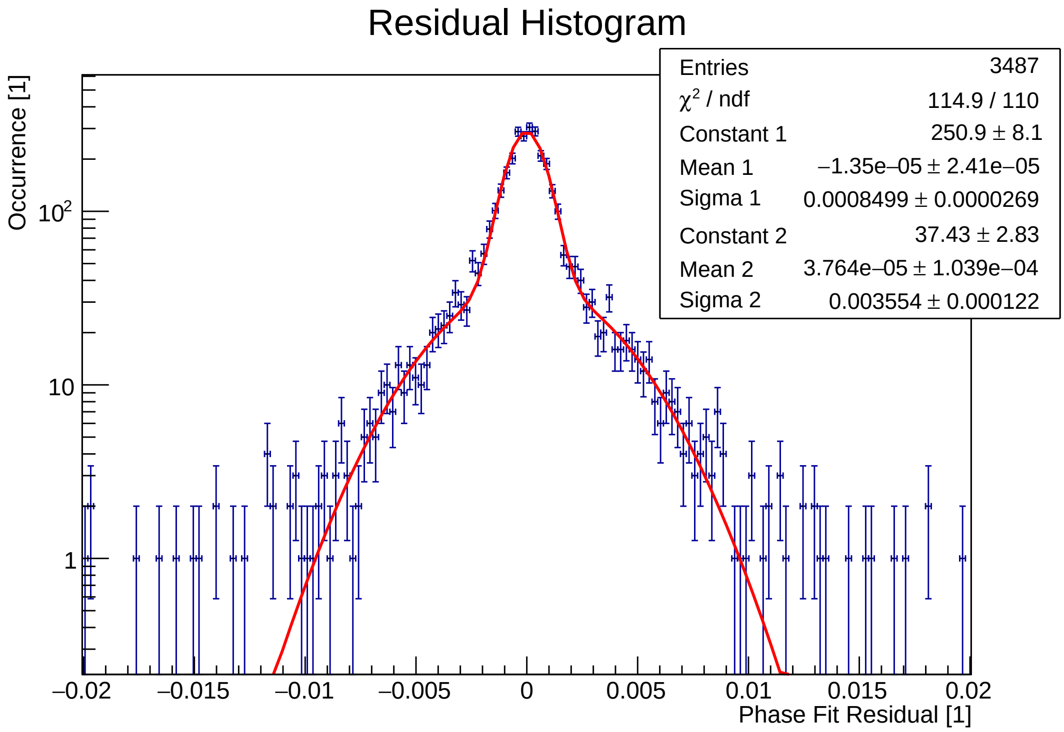

Figure 4.14: Histogram of cubic phase fit residuals for the whole year 2012 (log scale). The distribution is well described by the sum of two indipendent gaussians, the former being associated with more disperse January data and the latter with more accurate October data. The fit function was: $c_1 \cdot \exp[-(x-m_1)^2/(2\sigma_1^2)] + c_2 \cdot \exp[-(x-m_2)^2/(2\sigma_2^2)]$

.

$\mathcal{I}_{\mathcal{J},\mathcal{O}} = 113442$

Parameter	Value		
t_0	55930		MJD
ν_0	29.704873533		Hz
p_0	1.6975(2)		
p_1	$-2.48891(4)$	$\cdot 10^{-5}$	Hz
p_2	1.8537960(3)	$\cdot 10^{-10}$	Hz^2
p_3	$-1.8677(7)$	$\cdot 10^{-21}$	Hz^3

Table 4.18: Global 2012 fit, temporal gauge and resulting parameters. The long time spanned by observations (≃ 300 d) made the measurement of p_3 possible, while the very high number of points (3487) allows better parameters' estimates. The fit's chisquare is $\chi^2_{red.} = 1.71$.

ibilities being 1.40 and 0.76, respectively. The global non-gaussian residual distribution is thus interpreted as resulting from the sum of two datasets with different dispersion, the residuals of each of them being distributed according to a gaussian law.

4.4.1 Braking index

Being the coefficient p_3 of the third grade term in 3.15 associated with the *second* derivative of pulsar's rotation frequency $\ddot{\nu}$, its measurement in Table 4.18 allows us to derive an estimate of the pulsar's braking index (see section 1.3.1). The physical parameters related to the global 2012 fit are:

$$\underline{\textbf{2012 data}} \begin{cases} t_0 & = & 55930 & \mathrm{MJD} \\ \nu(t_0) & = & 29.7048984217(4) & \mathrm{Hz} \\ \dot{\nu}(t_0) & = & -3.7075921(6)\cdot 10^{-10} & \mathrm{Hz}^2 \\ \ddot{\nu}(t_0) & = & 1.1206(4)\cdot 10^{-20} & \mathrm{Hz}^3 \\ & & & \\ n(t_0) & = & 2.422 \pm 0.001 & \end{cases}$$

Table 4.19: Pulsar's physical parameters drawn from 2012 global phase solution.

The braking index measurement falls in the range quoted in the literature (2.3 – 2.5), where the higher value of 2.5 are obtained during period between and far from pulsar glitches, [35], [36]. The lower estimate of this work may be understood by noting that on 10 November 2011 (MJD 55875) the Crab pulsar underwent a major glitch event (see Section 1.3.2). During such events the pulsar rotation slowdown rate abruptly increases; this is followed by an initial post-glitch recovery period lasting ≃ 100 d, during which the slowdown rate lowers to values similar to the pre-glitch phase, and by a longer stabilization period (≃ 320 d), [36]. Since January observations were done on MJD 55930 (55 d after the glitch) and October ones at MJD 56217 (342 d after the glitch), the low measured n is likely a consequence of post-glitch settlement effects.

4.5 Radio comparison

This final section is devoted to the comparison of optical measurements with the radio ephemerides from the Jodrell Banks Radio Observatory (`http://www.jb.man.ac.uk/~pulsar/crab.html`) [35]. These ephemerides consist of a monthly updated phase solution based on radio observations. Ephemerides covering AQUEYE's optical observations' periods are listed in Table 4.20.

Period	t'_0 **[MJD]**	t_1 **[s]**	ν **[Hz]**	$\dot{\nu}$ **[10^{-15}Hz^2]**	e_t **[μs]**
January	55941	0.028576	29.7045458881(3)	-370746.21(42)	170
October	56215	0.018797	29.6957720714(2)	-370494.71(52)	90

Table 4.20: Radio ephemerides from Jodrell Banks Radio Observatory (Manchester University). The phase solution is given in terms of: the reference time t'_0; the time of arrival of the first main pulse t_1 after the reference time, in seconds; Frequency ν and its first derivative $\dot{\nu}$ at t'_0; an estimate of the total (statistical+systematical) error for a phase measurement obtained from these parameters, valid over the whole month.

To compare the optical and radio solution, a common reference has to be used. This can be accomplished by using formula B.20, which maps a phase solution with time reference t'_0 in the phase drift ψ calculated for a different time reference t_0 (see Appendix B). To further ease the comparison, we subtract the optical phase curve (fitted on optical data). Resulting plots for January and October observations are shown in Figures 4.15 and 4.16.

For both sessions the (pointwise) average radio-optical delay Δt_p and the reduced χ^2_{RAD} of optical data with respect to the radio phase curve was determined, considering as the error on each point the quadratic sum of both the optical fit error and the quoted radio e_t error as if it were purely statistical: $\sigma^2_{tot} = \sigma^2_{opt.} + e^2_t$. Since the radio delay curve has a non-null slope (see next chapter), the value of Δt_p calculated in this way depends upon the optical points' distribution: the average delay will be closer to values which occur near higher concentrations of optical points. For this reason, we derive also the (curvewise) mean radio-optical delay Δt_c occuring between optical and radio ephemeris curves: this value is essentialy the mean of the green curve in Figures 4.15 and 4.16 and is not influenced by the time distribution of experimental measurements, but a significant error for it is not straightforward to compute and the whole radio error e_t was considered; the optical fit error was neglected, being about 1/100th of the radio one. Results follow in Table 4.21.

Observation	N	$(\Delta t)_p$	χ^2_{RAD}	$(\Delta t)_c$
January	1509	$187 \pm 5\,\mu$s	1.34	$179 \pm 170\,\mu$s
October	1982	$225 \pm 2\,\mu$s	6.05	$216 \pm 90\,\mu$s

Table 4.21: Radio delay Δt values and reduced χ^2_{RAD} with respect to the radio phase solution. See text for details.

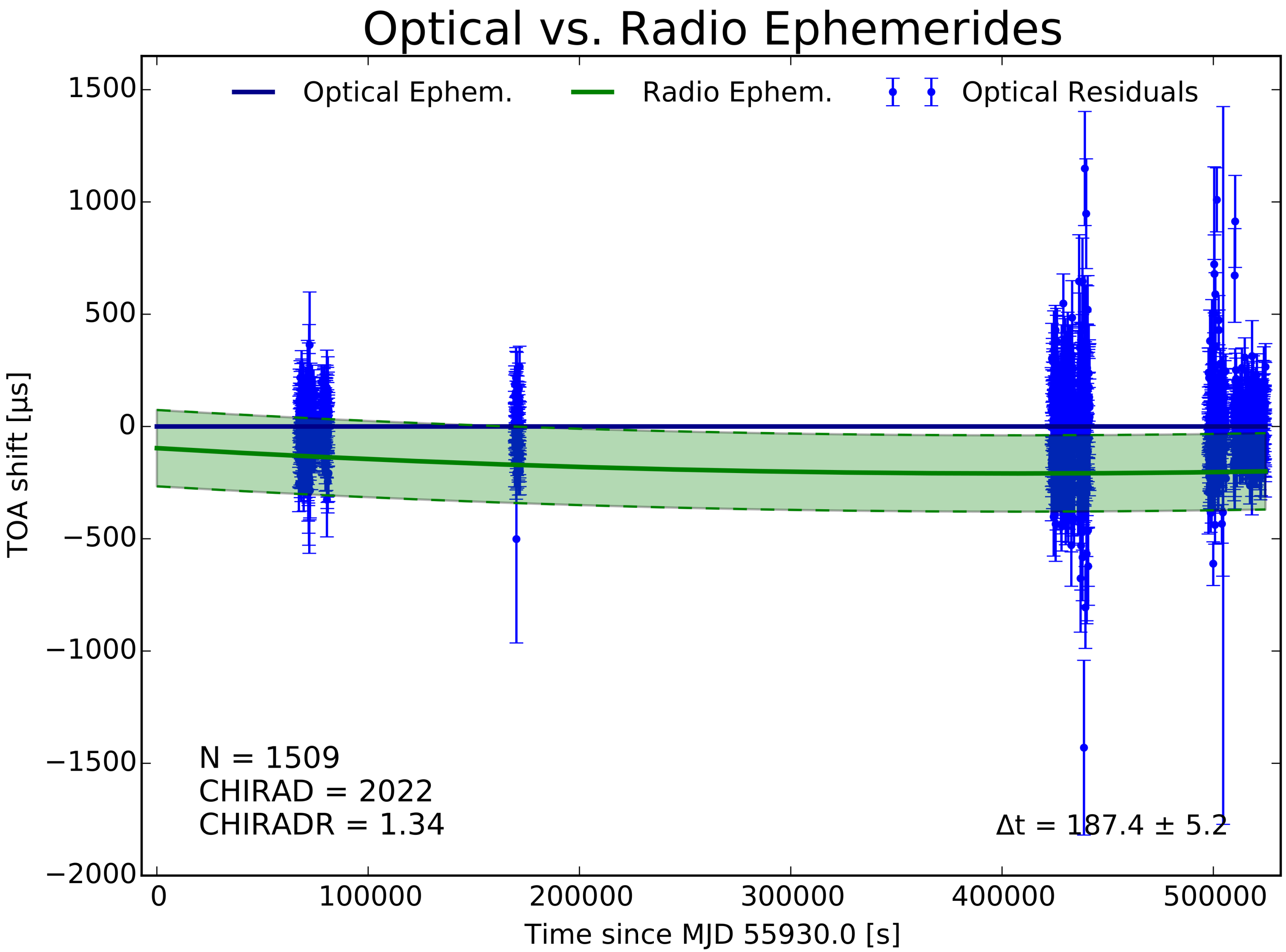

Figure 4.15: Optical data and radio ephemeris for January 2012, plotted as residuals with respect to the optical data fit. The green band represents the statistical + systematical error on a measure drawn from the radio ephemeris. $N = 1509$ optical points are plotted. The reduced chisquare of optical data with respect to the radio curve is $\chi^2_{red.} = 1.34$. The average delay of radio data is $187 \pm 5\,\mu$s (pointwise) and $179 \pm 170\,\mu$s (continuum). The 1σ error bands on optical fit are not visible on this scale.

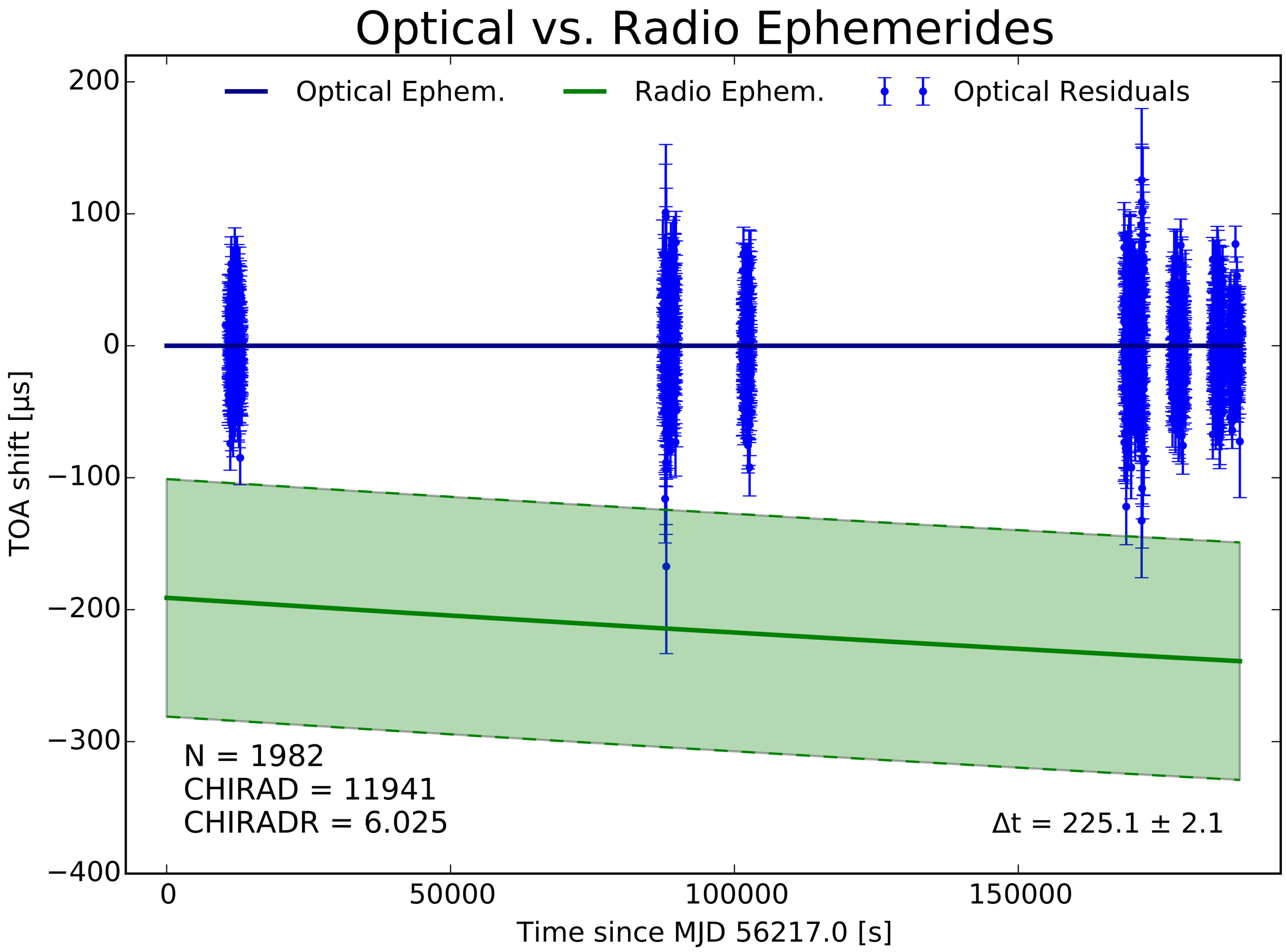

Figure 4.16: Optical data and radio ephemeris for October 2012, plotted as residuals with respect to the optical data fit. The green band represents the statistical + systematical error on a measure drawn from the radio ephemeris. $N = 1982$ optical points are plotted. The reduced chisquare of optical data with respect to the radio curve is $\chi^2_{red.} = 6.05$: the radio delay is thus highly significant. The average delay of radio data is $225 \pm 2\,\mu$s (pointwise) and $216 \pm 90\,\mu$s (continuum). The 1σ error bands on optical fit are not visible on this scale.

While the radio pulse delay computed for January is not very robust, due to the high radio uncertainty ($\chi^2_{RAD} \simeq 1$ and $e_{t,JAN} = 170\,\mu$s), the October data are clearly inconsistent with the radio prediction, showing a delay of the radio pulse with respect to the optical one of the order of 200 μs. This is consistent with previous indipendent measurements [37], [38], [39], [40], [23], [24], and is likely a true feature of the Crab pulsar.

4.6 Note on χ^2 values

The reduced χ^2 values which have been reported for polynomial phase drift fits are all less than 2.0, thus indicating an overall good fit quality. Nontheless, such values have an infinitesimal probability to manifest in a fit with $N \simeq 1000$–2000 degrees of freedom, and are above any reasonable χ^2 test rejection threshold. Since the residuals for all fits do distribute as a normal law and exbit no pathological behaviour, this fact is interpreded as an underestimate of errors on δ values made by the folded lightcurve fitting algorithm. This indeed, for internal efficiency speedup, returns only a statistical error on the peak shift δ, and neglects possible correlations with other parameters. As reported in Appendix C, two lightcurve fitting algorithms were used to test results' stability against fitting methods, both giving similar outcomes.

Furthermore, by calculating the mean error of the LC fitting algorithm and comparing it to the residuals dispersion σ (Figures 4.7, 4.11 and 4.14) such an underestimate is in fact found, the average point error being 70% – 90% of the residual standard deviation. These values translates to an empirical correction on chisquare values in the range 20% – 60%, just the one required for fully compatible χ^2 test values, supporting the fit error underestimate hypotesis. Because of this, "high" χ^2 values in phase drift fits have not been considered significative, their influence on final results being most likely negligible.

Chapter 5

Conclusions

In this work, we derived an optical phase solution for the Crab pulsar in January and October 2012, and a global solution for the whole period Jan-Oct 2012. This made it possible to measure the pulsar's rotation frequency ν and the frequency's first and second derivatives $\dot{\nu}$, $\ddot{\nu}$, ultimately allowing us to calculate the braking index $n \simeq 2.42$.

Optical data were then compared with monthly radio ephemerides from Jodrell Banks Observatory, showing a delay between radio and optical data, i.e. pulsar's main radio pulses arrive later than their optical counterparts. January data (Figure 4.15) are not believed to have sufficient significance, the reduced chisquare of optical measurements with respect to the radio solution being only 1.33. On the other hand, October data (Figure 4.16) give a radio signal delay of $\Delta t_c = 216 \pm 90\,\mu$s, with the optical points having a reduced chisquare of 6.05 with respect to the radio measurements. This is in agreement with previous works on the same subject, which also found a delay of $\simeq 200\,\mu$s (see Figure 5.1 and [25], [28], [37], [38] and [41]). Part of these measurements were obtained with different instruments and techniques, indicating that this result is not caused by measurement faults or systematic errors.

A difference in the rotation frequency between radio and optical data is also observed (slope of green line in Figure 4.16). However, it is always well consistent with the quoted radio ephemerides' error. Uncertainties affecting radio measurements and ultimately the radio-optical delay are likely to result from uncertainties on the *dispersion measure* (DM) of radio data, i.e. the amount of time by which radio waves are delayed propagating through the interstellar medium. This value continuously varies as the column density of interstellar medium between Earth and the Crab pulsar does, largely because of variations of the plasma conditions inside the pulsar's nebula. Also the slope of the radio-optical delay is likely affected by the uncertainty on the DM.

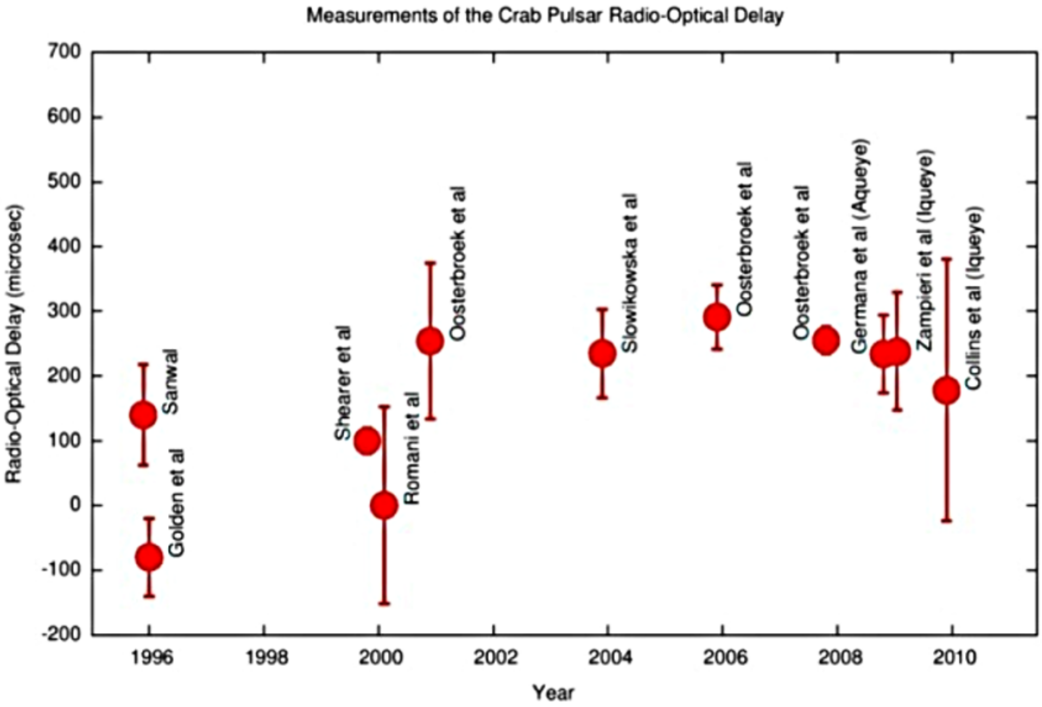

Figure 5.1: Former radio delay measurements. The last three points are from AQUEYE/IQUEYE observations: their errors are dominated by the uncertainty on the radio ephemerides.

Run	d_p	α_p	d_c	α_c
January	56.1 ± 1.5 km	0.034(1) rad	53.7 ± 51.0 km	0.033(32) rad
October	67.5 ± 0.6 km	0.0420(4) rad	64.5 ± 27.0 km	0.040(16) rad

Table 5.1: Linear and angular distance constrains on optical and radio emitters' separation, derived from Table 4.21.

Since baricentering calculations performed by dedicated software (TEMPO) are accurate at the level of 1 ps, the radio delay could be caused by:

- A genuine feature of the pulsar signal, i.e. the emission mechanism is such that visible radiation is emitted $\simeq 200\,\mu$s before the radio one;

- An alteration of the pulsar signal occuring during its path to the Earth. Being radio data already corrected against dispersion in the intestellar plasma, which does not affect optical photons by more than 10^{-12} s, there is no known phenomenon which can cause such a frequency-dependent effect. The first hypotesis is considered to be more plausible, as is done in other works [24].

Assuming that all radio delay is produced close to the pulsar, values derived in the previous chaper allow to derive simple geometric constrains to the basic oblique rotator model outlined in Section 1.3. These assume that a physical separation between the radio and optical emitting zones is present.

A typical linear distance may be derived between the radio and optical emitting zones as $d = \Delta t/c$. October 2012 data lead to $d_p = 67.5 \pm 0.6$ km by using the pointwise average Δt_p (weighted average of delays between the radio ephemerides and optical measurements) and $d_c = 64.5 \pm 27.0$ km by using the curve average Δt_c (average of radio phase solution delay from optical phase solution). The total statistic+systematic radio uncertainty of $90\,\mu$s was assumed on Δt_c to calculate d_c, which results in a likely overestimated error. These two values are in mutual agreement and are consistent with previous works' estimates, which derive a similar value of $\simeq 60$ km.

A second possibility is that optical and radio emitters are at different angles. By using the same value of Δt_p and Δt_c from October data, this gives a phase separation $\alpha = \omega\,\Delta t = 2\pi\nu\,\Delta t$, which is found to be $\alpha_p = 0.0420(4)$ rad and $\alpha_c = 0.040(16)$ rad, corresponing to an angle of about 2.4°. Values for both January and October runs are summoned up in Table 5.1.

At present days, a complete understanding of the Pulsar emission Physics is still lacking. The radio-optical delay derived in this work and the simple geometrical estimates made in the last paragraphs may be releavant for modeling the shape of the emission zone, assuming that the detected radio delay is only due to a physical separation.

Some measurements of the delay in other energy bands have been done in recent years: the Crab pulsar is a good candidate to do so, since it is observable along the whole electromagnetic spectrum. Simultaneous observations in radio and X-rays/γ-rays have been performed with the Rossi X-ray Timing Explorer ($\simeq 340\,\mu$s, [42]) and Fermi/LAT ($\simeq 280\,\mu$s, [43]) satellites. Implications of all these measurements for the pulsar emission mechanism are still debated. The use of simultaneous radio observations, in contrast to mean radio ephemerides, can largely reduce the uncertainty on the final results.

This work showed the power of pulsar timing at visible wavelengths, which is able to give very accurate results even with small aperture telescopes. We hope that next-generation observatories equipped with fast photometers, which AQUEYE and IQUEYE can be considered prototypes of, will really reach the "quantum" light timing limits, thus making a new kind of Astrophysics possible.

Appendix A

Fourier Transform

Consider a sufficiently well-behaved periodic function $X(t) : \mathbb{R} \rightarrow \mathbb{C}$ with period $T = 1/f$. This function can be represented by a combination of terms like $\exp(2\pi i\, n f\, t)$ with integer n, the *Fourier series* of $X(t)$:

$$X(t) \;=\; \sum_{n=-\infty}^{\infty} k_n\, e^{2\pi i n f t} \tag{A.1}$$

The coefficients k_n are the *Fourier coefficients* for $X(t)$. The Fourier coefficient k_n is determined by:

$$k_n \;=\; \frac{1}{T}\int_0^T X(t) e^{-2\pi i n f t}\, dt \tag{A.2}$$

It is straightforward to show that the Fourier coefficients are linear in X, that is a function $Z(t) = X(t) + Y(t)$ has Fourier coefficients $k(z)_n = k(x)_n + k(y)_n$. Further, if $X(t) \in \mathbb{R}$ (a real function), this imply that:

$$k_{-n} \;=\; k_n^* \tag{A.3}$$

Suppose now to deal with a non-periodic fuction $x(t)$. Define the fuction $x_T(t)$ as a periodic function with period T which is equal to $x(t)$ between $-T/2$ and $T/2$. As $x_T(t)$ is a periodic function on $(-T/2, +T/2)$ it can be written as a Fourier series:

$$x_T(t) \;=\; \sum_{n=-\infty}^{+\infty} k_n\, e^{2\pi i \frac{n}{T} t} \tag{A.4}$$

Let now T tend to ∞. In such a situation the above sum has to be replaced by an integral:

$$\sum_{n=-\infty}^{+\infty} \rightarrow \int_{-\infty}^{+\infty} df \tag{A.5}$$

As $\lim_{T\rightarrow\infty} x_T(t) = x(t)$, we have:

$$x(t) \;=\; \int_{-\infty}^{+\infty} \mathcal{X}(f)\, e^{2\pi i f t}\, df \tag{A.6}$$

$\mathcal{X}(t)$ is the *Fourier Trasform* of $x(t)$, a function defined on the *frequency domain*, i.e. on $\mathbb{R} \ni f$. The Fourier transform can be evaluated:

$$\mathcal{X}(f) = \int_{-\infty}^{+\infty} x(t)\, e^{-2\pi i f t}\, dt \tag{A.7}$$

The operators, both acting on integrable functions:

$$\mathcal{F}(\circ) = \int_{-\infty}^{+\infty} (\circ)\, e^{-2\pi i f t}\, dt \tag{A.8}$$

$$\mathcal{F}^{-1}(\circ) = \int_{-\infty}^{+\infty} (\circ)\, e^{2\pi i f t}\, df \tag{A.9}$$

are the Fourier Transform and Antitrasform (or Inverse-Transform) operators:

$$\mathcal{X}(f) = \mathcal{F}(x)\,(f) \tag{A.10}$$

$$x(t) = \mathcal{F}^{-1}(\mathcal{X})\,(t) \tag{A.11}$$

Of course $\mathcal{F}^{-1}(\mathcal{F}(\circ)) = \mathbb{1}$. Again, if $x(t)$ is real, the Fourier Transform has the property $\mathcal{X}(-f) = \mathcal{X}^*(f)$. A general introduction to Fourier Transform properties is beyond the scope of this Appendix. We just stress that different definitions exist, generally being different by a $1/2\pi$ factor either in the direct or inverse transform. Next sections are dedicated to some important results which are used elsewhere in the document.

A.1 Parseval Theorem

Suppose we have a real function $x(t)$. This function may represent a time-varying signal. The quantity:

$$P(x) = \int_{-\infty}^{+\infty} |x(t)|^2\, dt = \int_{-\infty}^{+\infty} x(t)x^*(t)\, dt \tag{A.12}$$

is related to the overall "energy" carried by the signal (if the signal is an electromagnetic wave, this is proportional to the carried energy). This can be related to the energy carried by *each single periodic component* by this theorem, named after Parseval:

Theorem 1. *Let $x(t)$ be a Fourier-transformable function and $\mathcal{X}(f)$ its Fourier Transform. Then:*

$$\int_{-\infty}^{+\infty} x(t)\, x^*(t)\, dt = \int_{-\infty}^{+\infty} \mathcal{X}(f)\, \mathcal{X}^*(f)\, df \tag{A.13}$$

Proof. We subsitute the definition of Fourier transform A.7 in the right-hand side of the above expression. This leads to:

$$\int_{-\infty}^{+\infty} \mathcal{X}(f)\,\mathcal{X}^{*}(f)\,df = \int_{-\infty}^{+\infty} df\,\mathcal{X}(f)\left(\int_{-\infty}^{+\infty} x(t)\,e^{-2\pi i f t}\,dt\right)^{*} \tag{A.14}$$

$$= \int_{-\infty}^{+\infty} df\,\mathcal{X}(f)\int_{-\infty}^{+\infty} x^{*}(t)\,e^{2\pi i f t}\,dt \tag{A.15}$$

$$= \int_{-\infty}^{+\infty} dt\,x^{*}(t)\int_{-\infty}^{+\infty} \mathcal{X}(f)\,e^{2\pi i f t}\,df \tag{A.16}$$

$$= \int_{-\infty}^{+\infty} dt\,x^{*}(t)\,x(t) \tag{A.17}$$

□

A.2 Convolution Theorem

The convolution of a function $x(t)$ with a function $y(t)$, written $x \circledast y\,(t)$ is a function of t defined as:

$$x \circledast y\,(t) = \int_{-\infty}^{+\infty} f(\tau)g(t-\tau)\,d\tau \tag{A.18}$$

The convolution operator $\circledast$ is commutative. Convolution has the geometric interpretation of replacing the value $x(t)$ with the $y(-t)$-weighted average of the function x centered on t. We proof an important theorem:

Theorem 2. *Suppose $x(t)$ and $y(t)$ are Fourier-transformable functions. Than the Fourier transform of their convolution is:*

$$\mathcal{F}(x \circledast y)\,(f) = \mathcal{F}(x)\cdot\mathcal{F}(y)\,(f) \tag{A.19}$$

And the inverse is also true, namely the Fourier transform of the product of $x(t)$ and $y(t)$ is:

$$\mathcal{F}(x\cdot y)\,(f) = \mathcal{F}(x) \circledast \mathcal{F}(y)\,(f) \tag{A.20}$$

Proof. The proof that $(x \circledast y)$ is also Fourier-transformable is omitted. We proof the direct version of the theorem first, by inserting equation A.18 in A.7:

$$\mathcal{F}(x \circledast y)\,(f) = \int_{-\infty}^{+\infty}\int_{-\infty}^{+\infty} x(\tau)y(t-\tau)\,d\tau \quad e^{-2\pi i f t}\,dt \tag{A.21}$$

$$= \int_{-\infty}^{+\infty} d\tau x(\tau)\int_{-\infty}^{+\infty} dt\,y(t-\tau)\,e^{-2\pi i f t} \tag{A.22}$$

$$_{(t-\tau=t')} \quad = \int_{-\infty}^{+\infty} d\tau\,x(\tau)\,e^{-2\pi i f \tau}\int_{-\infty}^{+\infty} dt'\,y(t')\,e^{-2\pi i f t'} \tag{A.23}$$

$$= \mathcal{F}(x)\cdot\mathcal{F}(y)\,(f) \tag{A.24}$$

Let us proof the invere statement:

$$
\begin{aligned}
\mathcal{F}(x) \circledast \mathcal{F}(y)\,(f) &= \int_{-\infty}^{+\infty} \mathcal{X}(\phi)\mathcal{Y}(f-\phi)\,d\phi && \text{(A.25)}\\
&= \int_{-\infty}^{+\infty} d\phi \int_{-\infty}^{+\infty} x(t)e^{-2\pi i\phi t}\,dt \int_{-\infty}^{+\infty} y(t')e^{-2\pi i(f-\phi)t'}\,dt' && \text{(A.26)}\\
&= \int_{-\infty}^{+\infty} dt\,x(t) \int_{-\infty}^{+\infty} dt'\,y(t')e^{-2\pi ift'} \int_{-\infty}^{+\infty} d\phi e^{-2\pi i(t-t')\phi} && \text{(A.27)}\\
&= \int_{-\infty}^{+\infty} dt\,x(t) \int_{-\infty}^{+\infty} dt'\,y(t')e^{-2\pi ift'}\,\delta(t-t') && \text{(A.28)}\\
&= \int_{-\infty}^{+\infty} dt\,x(t)\,y(t)\,e^{-2\pi ift} && \text{(A.29)}\\
&= \mathcal{F}(x\cdot y)\,(f) && \text{(A.30)}
\end{aligned}
$$

□

A.3 Sampling

Suppose we sample a signal $x(t)$ with a period $T_s = 1/f_s$. The resulting signal $x_s(t)$ can be written as:

$$x_s(t) = x(t)\cdot\sum_{n=-\infty}^{+\infty}\delta(t-nT_s) \tag{A.31}$$

By the inverse convolution theorem, its Fourier transform is:

$$
\begin{aligned}
\mathcal{X}_s(f) &= \mathcal{X}\circledast\mathcal{F}\left[\sum_{n=-\infty}^{+\infty}\delta(t-nT_s)\right] && \text{(A.32)}\\
&= \mathcal{X}\circledast f_v\sum_{n=-\infty}^{+\infty}\delta(f-nf_s) && \text{(A.33)}\\
&= f_v[\cdots+\mathcal{X}(f+f_s)+\mathcal{X}(f)+\mathcal{X}(f-f_s)+\dots] && \text{(A.34)}
\end{aligned}
$$

That is, the Fourier transform $\mathcal{X}_s(f)$ of $x_s(t)$ is the sum of $\mathcal{X}(f)$ and of an infinite series of its clones, each shifted by f_s. Suppose now that $\mathcal{X}(f)$ is null above a certain frequency $f^\star$ and below the opposite $-f^\star$. In order for $\mathcal{X}_s(f)$ to faithfully reproduce the shape of $\mathcal{X}(f)$ the separation between two adjacent clones has to be at least $f_s \geq 2f^\star$, so that the fist clone ends at $f^\star$, just where the second starts. The frequency $2f^\star$ is the Nyquist rate of the signal, i.e. the minimum frequency at which sampling can be done without losing information on the signal. Conversely, given a sampling frequency f_s, the *Nyquist frequency* $f_N = f_s/2$ is the maximum frequency which one can determine. If $f^\star \geq f_N$ for a certain sampled signal, the original signal is sub-sampled and its reconstruction will be affected by aliasing phenomena.

Finally, if the signal is sampled for a finite time Θ, an extra rectangular function $\mathrm{rect}_{\Theta}(t)$ ought to be multiplied in A.31, or equivalently the summation should be carried only from $-\Theta/2T_s$ to $\Theta/2T_s$. This produces a third convolution term in A.34, of the kind:

$$\Theta \,\mathrm{sinc}\,(\pi f \Theta) \tag{A.35}$$

Accounting for the impossibility to reconstruct long term ($t \geq \Theta$) variabilities of $x(t)$.

Appendix B

Temporal Gauges

This appendix presents the algebra employed in transforming data and parameters obtained by phase analysis with a temporal gauge $G = \{t_0, \Phi_0, \nu_0\}$ to a different temporal gauge $G' = \left\{t'_0, \Phi'_0, \nu'_0\right\}$. A temporal gauge was defined by equation 3.9 as the set of three values which specifies the relation between the phase drift $\psi(t)$ and the actual phase $\phi(t)$:

$$\varphi(t) \; = \; \Phi_0 + \nu_0 (t - t_0) + \psi(t - t_0) \tag{B.1}$$

The term Φ_0 (integer phase translations) is arbitrary and usually taken as zero; it will thus be neglected in following development, the gauge $\{t_0, 0, \nu_0\}$ being labeled simply by $\{t_0, \nu_0\}$.
Throughout this section the symbol $\lfloor x \rfloor$ denotes the *integer* or *floor part* of x, i.e. the closest and smaller integer number to x. The *fractional part* of x will be denoted by $\mathfrak{F}\{x\}$, where $\mathfrak{F}\{x\} = x - \lfloor x \rfloor \geq 0$.

$$\begin{aligned} \text{Integer part} \quad &\Rightarrow \quad \lfloor x \rfloor \\ \text{Fractional part} \quad &\Rightarrow \quad \mathfrak{F}\{x\} \end{aligned}$$

B.1 Data transformation

In the context of folding techniques (see section 3.3.3) the *peak shift* $\delta(t)$ was introduced as the phase difference between t and the time $t^* > t$ at which the next main pulse arrive:

$$\delta \; = \; \frac{t^* - t}{T_0} \tag{B.2}$$

where T_0 is the folding period. The time t is not a continuous variable, but rather takes values at which folding segments begin. It was shown also that a relation holds between the peak shift δ and the phase drift ψ from a uniform rotator with frequency $\nu_0 = 1/T_0$, namely δ and ψ are explementary:

$$\delta(t) \; = \; \mathfrak{F}\{1 - \psi(t)\} \tag{B.3}$$

This defines a correspondence between data folded with period T_0 and starting point t_0 and the phase drift curve related to the $\{t_0, \nu_0 = 1/T_0\}$ gauge. Transformations from a the gauge $G = \{t_0, T_0\}$ to $G' = \left\{t'_0, T'_0\right\}$ will thus link folding based at t_0 with period T_0 with the one based at t'_0 with T'_0.
To derive the proper transformation, note first that the time at which a specific pulse occurs must be the same in the two gauges, since it is correlated to a physical event[1]:

$$t_0 + t^* = t'_0 + t^{*\prime} \tag{B.4}$$

The above equation can be rearranged into:

$$\begin{aligned} t^{*\prime} &= t^* + t_0 - t'_0 \\ &= t^* + \Delta \end{aligned} \tag{B.5}$$

where $\Delta = t_0 - t'_0$ denotes the difference between the base times. It is now possible to insert the expression for δ to remove t^*, but some care has to be taken while inverting equation B.2.
Indeed, the t value in (t, δ) data doesn't usually refer to the beginning of a one-period folding segment as in B.2, being rather taken as the mid-time $t_{1/2}$ of the folding segment (see section 3.3.2). Since δ doesn't really vary on a sub-period scale, we can refer the beginning of the folded lightcurve to the one-period slice which contains the mid-time of the folding segment. This can be done by operating on time values the substitution:

$$t \rightarrow \left\lfloor \frac{t}{T_0} \right\rfloor T_0 \tag{B.6}$$

Inverting equation B.2 is now straightforward:

$$t^* = \left\lfloor \frac{t}{T_0} \right\rfloor T_0 + \delta T_0 \tag{B.7}$$

And further insertion in B.5 leads to:

$$t^{*\prime} = \Delta + \left\lfloor \frac{t}{T_0} \right\rfloor T_0 + \delta T_0 \tag{B.8}$$

The equivalent of equation B.2 for G' ought to be used in order to derive δ':

$$\delta' = \frac{t^{*\prime} - t'}{T'_0} \tag{B.9}$$

The former equation can further be cast in the form:

$$\delta' = \frac{t^{*\prime}}{T'_0} - \frac{t'}{T'_0} \tag{B.10}$$

---

[1] The times t^* and $t^{*\prime}$, as well as t and t' later on, are measured from their respective reference t_0 and t'_0.

But $t' = \left\lfloor \frac{t^{*\prime}}{T'_0} \right\rfloor T'_0$, since it is the time which the T'_0 folded slice containing $t^{*\prime}$ starts at:

$$\delta' = \frac{t^{*\prime}}{T'_0} - \left\lfloor \frac{t^{*\prime}}{T'_0} \right\rfloor \tag{B.11}$$

Which finally reduces to:

$$\delta' = \mathfrak{F}\left\{ \frac{\Delta}{T'_0} + \left\lfloor \frac{t}{T_0} \right\rfloor \frac{T_0}{T'_0} + \delta \frac{T_0}{T'_0} \right\} \tag{B.12}$$

Equation B.12 defines the seeked relation, which enables to transform data folded within the gauge $G = \{t_0, T_0\}$ to corresponding data in the gauge $G' = \left\{t'_0, T'_0\right\}$. To complete the transformation, it is necessary to translate time by Δ.

The relation B.12 has a primary role in long-period phase analysis. This task involves phasing of very distant (several months) observations, which cannot be folded with the same reference period, being its changes during such a long interval too large. On the other hand, a single folding gauge is required to try a global fit of the data; a solution might be found by folding each observations' set with a "local" gauge and then pulling them back to a single gauge with B.12. This approach proved to be enought robust to make a common fit of the January and October 2012 data, which later permitted to estimate the frequency's second derivative $\ddot{\nu}$ and the braking index n.

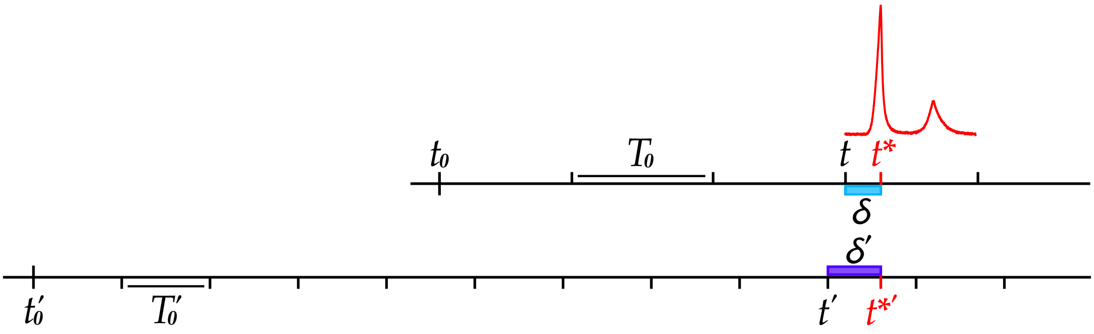

Figure B.1: Illustration of time variables involved in the temporal gauge transformation and their relative positions. The upper time axes is associated with the gauge G, while the lower one uses G'. The azure and violet segments represent respectively the peak shifts δ and δ'.

B.2 Phase solution transformation

If a phase solution is known, it is straightforward to compare it with a second phase solution. The best way to visualize if any delay is present is to reduce both solutions to a residual ψ versus ψ_{fit} plot, since so any offset will be directly shown in the plot.
Let us denote the second phase solution and related parameters with the prime symbol.

$$\begin{aligned} \varphi(t) &= \varphi_0 + \nu(t-t_0) + \frac{1}{2}\dot{\nu}(t-t_0)^2 + ... \quad &(B.13)\\ \varphi'(t) &= \varphi'_0 + \nu'(t-t'_0) + \frac{1}{2}\dot{\nu}'(t-t'_0)^2 + ... \quad &(B.14)\end{aligned}$$

Equation defining the temporal gauge is:

$$\varphi(t) = \Phi_0 + \nu_0(t-t_0) + \psi(t-t_0) \tag{B.15}$$

And inverting it one obtains:

$$\psi(t-t_0) = \varphi(t) - \Phi_0 - \nu_0(t-t_0) \tag{B.16}$$

The analogous relation for φ' is:

$$\begin{aligned} \psi'(t-t_0) &= \varphi'(t) - \Phi_0 - \nu_0(t-t_0) \quad &(B.17)\\ &= \Psi'_0 + \psi'_0 + \nu'(t-t'_0) - \nu_0(t-t_0) + \frac{1}{2}\dot{\nu}'(t-t'_0)^2 + ... \quad &(B.18)\end{aligned}$$

Where $\Psi'_0 = \Phi'_0 - \Phi_0$ is the integer phase accumulated during the interval between time references. Let us call $\Delta = t_0 - t'_0$. Upon inserting it in round parenthesis, we obtain:

$$\psi(t-t_0)' = \Psi'_0 + \psi'_0 + \nu'\Delta + (\nu'-\nu_0)\cdot(t-t_0) + \frac{1}{2}\dot{\nu}'(t-t_0+\Delta)^2 + ... \tag{B.19}$$

Which is the relation porting the φ' phase in the temporal gauge of ψ. For computing purposes, it might be convenient to write it as:

$$\psi(t-t_0)' = \psi'_0 - \left\lfloor \psi'_0 + \nu'\Delta + \frac{1}{2}\dot{\nu}'\Delta^2 \right\rfloor + \nu'\Delta + (\nu'-\nu_0)\cdot(t-t_0) + \frac{1}{2}\dot{\nu}'(t-t_0+\Delta)^2 + ... \tag{B.20}$$

Appendix C

Computing details

The phase analysis procedures reported in this work required the development of several tools for data manipulation. These tools have been either written by the author or adapted by expanding previous existing ones. Next paragraphs briefly describe the most relevant ones.

Lightcurves

A simple `C++` program has been written to generate lightcurves from time series. This is basically done by defining the total number of desired bins and then iterating over photons to fill them. The method has been tested on few simple cases and has been debugged against bin-number rounding effects. Internal integer representation made use of the `unsigned long` type (64-bit) to handle high photon counts. The same code was used for a time-series folding tool, which was used to check results of a pre-existing `FORTRAN` one. A lightcurve statistical analysis tool (calculating Mean, Variance, Residual RMS) was coded in `Python` and used methods from the `NumPy` (`http://www.numpy.org/`) package. A simple `C++` linear regression program, based on least squares minimization, has been used too.

Power Spectra and Fourier Transforms

A set of `C++` tools have been developed for handling data Fourier transforms and power spectra generation. These make use of the `FFTW v.3` library (`http://www.fftw.org/`, [44]), a widely used Fast Fourier Transform Algorithm. Again, a Python script has been written for power spectra analysis operation, such as harmonics detection.

Epoch Folding Search

The EFS procedures were carried on by the `efsearch` tool, part of NASA's HEASARC `Xronos` suite. This tool has been written with radio observations as its primary target, but proved to behave well also with optical ones.

Folding and Phase tracking

A `Phyton` script has been adapted for managing the folding of time series into lightcurves and their following fit to find the peak shift δ. The fold is actually handled by a faster external `FORTRAN` executable, which loops through photons and folded lightcurve bins to generate a histogram. Two fitting procedures have been used to determine the peak shift, in order to test for possible dependance upon fit method. The first one uses the external `GNUPLOT` program, while the second uses `Python`'s `SciPy` (`http://scipy.org`) fitting capabilities. Both methods rely on a nonlinear least squares minimization algorithm, and give full compatible results.

Polynomial fit and integer phase shifts determination

To accomplish the polynomial fits required to get the phase solution and to determine the integer part of phase drift ψ among different observations, a `C++` program which is based on CERN's `ROOT` (`http://root.cern.ch/`) libraries was developed. This proved to be a good choice, since `ROOT`'s internal *linear* fit algorithm for polynomial functions is fast and allowed to test $\simeq$ 500 integer shifts combinations per second. Once observations' data are loaded, trial integer shifts $\mathcal{I} = (I_1, I_2, I_3, ...)$ between different runs are applied and resulting datasets are fitted. Results of each fit, a χ^2 vs. $\mathcal{I}$ table, high precision parameters of the best χ^2 fit, best $\mathcal{I}$ shifted data and a graph macro are then saved to disk.

Appendix D

Linear period phase drift

Suppose the period of the pulsar varies with a simple linear law:

$$T(t) = T_0 + kt \tag{D.1}$$

How will phase drift with respect to the uniform T_0 case evolve? The istantaneous frequency of the pulsar is:

$$\begin{aligned}
\nu(t) &= \frac{1}{T_0 + kt} && \text{(D.2)} \\
&= \frac{1}{T_0}\frac{1}{1 + k\frac{t}{T_0}} \\
&= \nu_0 \frac{1}{1 + k\frac{t}{T_0}} && \text{(D.3)}
\end{aligned}$$

The phase of the pulsar has to be calculated considering the varying frequency, i.e.:

$$\begin{aligned}
\varphi(t) &= \nu_0 \int_0^t \frac{1}{1 + k\frac{\tau}{T_0}}\, d\tau && \text{(D.4)} \\
&= \frac{1}{k} \int_0^{k\frac{t}{T_0}} \frac{1}{1+s}\, ds \\
&= \frac{1}{k} \ln\left(1 + k\frac{t}{T_0}\right) && \text{(D.5)} \\
&= \frac{1}{k}\left(k\frac{t}{T_0} - \frac{1}{2}k^2\frac{t^2}{T_0^2} + \frac{1}{6}k^3\frac{t^3}{T_0^3} + ...\right) && \text{(D.6)}
\end{aligned}$$

$$\varphi(t) = \nu_0 t - \frac{1}{2}k\frac{t^2}{T_0^2} + \frac{1}{6}k^2\frac{t^3}{T_0^3} + ... \tag{D.7}$$

The first term represents the uniform rotator, while higher order terms account for the phase drift ψ. Ending the Taylor expansion at the first significant term results in:

$$\psi(t) = -\frac{1}{2}k\frac{t^2}{T_0^2} \tag{D.8}$$

Equation D.2 enables also to calculate the theoretical braking index for such an ideal case:

$$n = -\frac{\nu\ddot{\nu}}{\dot{\nu}^2} = -\frac{\frac{1}{(T_0+kt)}(-2)\frac{1}{(T_0+kt)^3}}{\frac{1}{(T_0+kt)^4}} = 2 \tag{D.9}$$

With the aid of equation D.8, it is possible to estimate how much phase drift is accumulated during a period of time τ starting at time t after the reference t_0:

$$\begin{aligned}
\Delta\psi_t(\tau) &= -\frac{1}{2}\frac{k}{T_0^2}[(t+\tau)^2 - t^2] && \text{(D.10)}\\
&= -\frac{1}{2}\frac{k}{T_0^2}[2t\tau + \tau^2] && \text{(D.11)}\\
&\simeq -\frac{k}{T_0^2}t\tau && \text{(D.12)}
\end{aligned}$$

This proves to be useful during phase analysis to determine how folding should be performed. If the phase drift generated during a folding period τ is comparable to the bin width of the folded lightcurve at any time t spanned by the observations, there is loss of information caused by bins "flowing" each in its nearest. It is then convenient to define the maximum phase bin number N_ϕ as:

$$N_\phi = \frac{1}{k}\frac{T_0^2}{t\tau} \tag{D.13}$$

For the Crab pulsar (as of 2012), $k = 4{,}3 \cdot 10^{-13}\,\mathrm{s/s}$, $T_0 = 3.367 \cdot 10^{-2}\,\mathrm{s}$. The value for $t = 1\,\mathrm{d}$ and $\tau = 1\,\mathrm{s}$ is $N_\phi = 3 \cdot 10^4$. The cases of interest for this work are listed in the following table:

×	τ [s]	t [d]	$\Delta\psi$	N_ϕ
January	32	6	0.006	159
October	8	3	0.00078	1271
Global	8	300	0.078	13

If the maximum number of bins reaches very low values, such as the one for the global case, it is necessary to fold part of the data with a different gauge and then transforming the results with the relation which have been worked out in appendix B. Finally, if $\Delta\psi$ approaches unity, also such a procedure becomes dangerous, because the integer phase drift which occurs during time τ cannot be recovered neither with χ^2 minimization and is lost forever.

Appendix E

Theoretical EFS curve

Suppose we are folding a periodic signal (proper period T) with a period $T + \Delta T$ which is slightly off the actual one. We then compute the χ^2 for the folded lightcurve with respect to its average (RMS of residuals): what value will this χ^2 have? If we try different ΔT values and carry on an EFS procedure, what shape will the $\chi^2(\Delta T)$ curve have?

Let us inspect the χ^2 computed for the lightcurve:

$$\chi^2 = \sum_{i=0}^{N} \frac{\left(x'_i - \overline{x}'\right)^2}{x'_i} \tag{E.1}$$

In the above equation $\overline{x}$ is the mean of the x_i values, and we assumed Poisson statistics for the fluctuations ($\sigma_{x_i} = \sqrt{x_i}$). In the actual case the $x_i - \overline{x}$ values are all very small compared to x_i itself, being the true signal from the pulsar superimposed on a greater background. Thus, the errors $\sigma_i = \sqrt{x_i}$ may be just well approximated by a constant $\sigma = \sqrt{\overline{x}}$ error, being the variability of $\sqrt{x}$ even smaller than the one of x. We will thus assume that E.1 can be written as:

$$\chi^2 = \frac{1}{\overline{x}} \sum_{i=0}^{N} (x_i - \overline{x})^2 \tag{E.2}$$

$$\chi^2 \propto \sum_{i=0}^{N} z_i^2 \tag{E.3}$$

where z_i is the residual of bin i. From now on, both the signal and the folded lightcurve will be treated as continuous periodical functions. The continuous analogous to E.3 is:

$$\chi^2 = \int_0^T dt\, z^2(t) \tag{E.4}$$

How should we relate the folded lightcurve values $z(t)$ with the signal $Z(t)$, considering that the folding period is not the actual period of the signal but differs from it by ΔT?

Being the period slightly different, at first rollup the signal $Z(t)$ will not be summed with its correspondent $Z(t+T)$, but rather with $Z(t+T+\Delta T)$; at the second rollup, the value $Z(t+2T+2\Delta T)$ will be added, and so on untill the folding segment ends. There are $L/(T+\Delta T)$ cycles in the whole segment, but since $\Delta T/T$ is small we may approximate it to L/T. Being $Z(s+T) = Z(s)$, we will end up with:

$$z(t) \;=\; Z(t) + Z(t+\Delta T) + Z(t+2\Delta T) + ... + Z(t + L/T\ \Delta T) \tag{E.5}$$

We can mimic this in the continuous approach by convolving the signal $Z(t)$ with a normalized rectangular function $\mathrm{rect}_k(t)$ with width $k = L/T \cdot \Delta T$.

$$\mathrm{rect}_k(x) \;=\; \frac{1}{k}\cdot\begin{cases} 1 & -k/2 \;\le\; x \;\le\; k/2 \\ 0 & \text{elsewhere} \end{cases} \tag{E.6}$$

Actually the correct function to model E.5 behaviour is $\mathrm{rect}_k(x - k/2)$, but it can be proved that the convolution operator $\circledast$ commutes with translations, and since we are later integrating over the whole period T the translation itself is irrilevant.

$$z(t) \;=\; Z \circledast \mathrm{rect}_k\ (t) \tag{E.7}$$

We recall that the convolution of two functions (or of two distributions) is defined by the integral:

$$f \circledast g\ (x) \;=\; \int_{-\infty}^{+\infty} f(t) g(x-t)\, dt \tag{E.8}$$

By inserting E.7 in E.4 we obtain:

$$\chi^2(k) \;=\; \int_0^T dt\ \ [Z \circledast \mathrm{rect}_k]^2\,(t) \tag{E.9}$$

We will now leap in the frequency domain by chain applying the direct ($\mathcal{F}$) and inverse ($\mathcal{F}^{-1}$) Fourier transforms on the integrand. We shall indicate with the coursive letters $\mathcal{Z}$ and $\mathcal{R}_k$ the Fourier transforms of $Z(t)$ and $\mathrm{rect}_k(t)$. $\mathcal{Z}$ equals the Fourier transform $\mathcal{X}$ of the whole signal, but for the $\mathcal{X}(0)$ value (additive constant).

$$\begin{aligned}
\chi^2(k) \;&=\; \int_0^T dt\ \ [Z \circledast \mathrm{rect}_k]^2\,(t) && \text{(E.10)}\\
&=\; \int_0^T dt\, \mathcal{F}^{-1}\Big\{\mathcal{F}\Big[\,(Z \circledast \mathrm{rect}_k\,)^2\,\Big]\Big\}\,(t) && \text{(E.11)}\\
&=\; \int_0^T dt\ \int_{-\infty}^{+\infty} df\ e^{2\pi i t f}\ \ \mathcal{F}\,[\,(Z \circledast \mathrm{rect}_k) \cdot (Z \circledast \mathrm{rect}_k)\,]\ (f) && \text{(E.12)}\\
&=\; \int_0^T dt\ \int_{-\infty}^{+\infty} df\ e^{2\pi i t f}\ \ \mathcal{F}\,[\,Z \circledast \mathrm{rect}_k\,] \circledast \mathcal{F}\,[\,Z \circledast \mathrm{rect}_k\,]\ (f) && \text{(E.13)}\\
&=\; \int_0^T dt\ \int_{-\infty}^{+\infty} df\ e^{2\pi i t f}\ \ (\mathcal{Z} \cdot \mathcal{R}_k) \circledast (\mathcal{Z} \cdot \mathcal{R}_k)\ (f) && \text{(E.14)}
\end{aligned}$$

Where we made use twice of the convolution theorem (both direct and inverse form):

$$\text{Convolution theorem} \quad \begin{array}{rcl} \mathcal{F}\left(f \circledast g\right) & = & \mathcal{F}(f) \cdot \mathcal{F}(g) \\ \mathcal{F}\left(f \cdot g\right) & = & \mathcal{F}(f) \circledast \mathcal{F}(g) \end{array} \tag{E.15}$$

Note the self-convolution of the Fourier transform of $z(t)$ in E.13 and E.14 . We can further expand E.14 by using the convolution definition E.8:

$$\chi^2(k) = \int_0^T dt \int_{-\infty}^{+\infty} df\, e^{2\pi i t f} \int_{-\infty}^{+\infty} d\phi\, \mathcal{Z}(\phi) \cdot \mathcal{R}_k(\phi) \cdot \mathcal{Z}(f-\phi) \cdot \mathcal{R}_k(f-\phi) \tag{E.16}$$

Since the signal is periodic, it is possible to find a closed form for the equation E.16. We will solve it in three steps.

1. Solution for a δ function Suppose the signal's Fourier transform $\mathcal{Z}$ were the product of a constat ζ and a Dirac's δ function:

$$\mathcal{Z}(\phi) = \zeta \cdot \delta(\phi - f^\star) \tag{E.17}$$

Where $f^\star$ is a multiple of $f_0 = 1/T$. In this case the innermost integral in E.14 reduces to:

$$\zeta^2 \int_{-\infty}^{+\infty} d\phi \;\; \mathcal{R}_k(\phi)\mathcal{R}_k(f-\phi) \;\; \delta(\phi - f^\star)\delta(f - \phi - f^\star) \tag{E.18}$$

Using the sampling property for both delta, we can cast it in the neater form:

$$\zeta^2\mathcal{R}_k^2(f^\star) \int_{-\infty}^{+\infty} d\phi\; \delta(\phi - f^\star)\delta(f - \phi - f^\star) \tag{E.19}$$

And further arrange it into:

$$\zeta^2\mathcal{R}_k^2(f^\star) \int_{-\infty}^{+\infty} d\phi\; \delta(\phi - f^\star)\delta((f - f^\star) - \phi) \tag{E.20}$$

Direct comparison with E.8 shows that the integral is actually the convolution of $\delta(f)$ with $\delta_{f^\star}(f) = \delta(f - f^\star)$, evaluated at $f - f^\star$.

$$\int_{-\infty}^{+\infty} d\phi\; \delta(\phi - f^\star)\delta((f - f^\star) - \phi) = \left[\delta \circledast \delta_{f^\star}\right] (f - f^\star) \tag{E.21}$$

But δ is the neutral element for convolution operator:

$$\left[\delta \circledast \delta_{f^\star}\right] (f - f^\star) = \delta_{f^\star}(f - f^\star) \tag{E.22}$$

$$= \delta(f - 2f^\star) \tag{E.23}$$

Now the integral E.16 has become:

$$\chi^2(k) \;=\; \zeta^2\mathcal{R}_k^2(f^\star)\int_0^T dt\int_{-\infty}^{+\infty} df\, e^{2\pi itf}\delta(f-2f^\star) \tag{E.24}$$

The sampling property of delta can be applied again:

$$\chi^2(k) \;=\; \zeta^2\mathcal{R}_k^2(f^\star)\int_0^T dt\, e^{4\pi itf^\star} \tag{E.25}$$

But as we are integrating the cyclic function $e^{4\pi itf^\star}$ over T which is a multiple of its period, we finally get:

$$\chi^2(k) \;=\; 0 \tag{E.26}$$

2. Solution for a sinusoid It might seem strange that if χ^2 evaluates zero for a delta it may not do so for a linear combination of delta, but in fact the operator described by $\chi^2[\mathcal{Z}]$ is not linear, due to the self-convolution integral. We shall try and seek a solution for a sinusoid signal, which maps in the frequency domain to:

$$\mathcal{Z}(f) \;=\; \zeta\delta(f-f^\star)+\zeta^*\delta(f+f^\star) \tag{E.27}$$

The variable ζ^* is the complex conjugate of ζ. As before, $f^\star$ is a frequency which gives a periodicity in the $(0,T)$ interval. The innermost integral in E.16 now expands to:

$$\begin{aligned}
&\int_{-\infty}^{+\infty} d\phi\mathcal{Z}(\phi)\cdot\mathcal{R}_k(\phi)\cdot\mathcal{Z}(f-\phi)\cdot\mathcal{R}_k(f-\phi) \;=\\
&\quad=\zeta^2\int_{-\infty}^{+\infty} d\phi\;\; \mathcal{R}_k(\phi)\mathcal{R}_k(f-\phi)\;\; \delta(\phi-f^\star)\delta(f-\phi-f^\star)\,+\\
&\quad+\zeta^{*2}\int_{-\infty}^{+\infty} d\phi\;\; \mathcal{R}_k(\phi)\mathcal{R}_k(f-\phi)\;\; \delta(\phi+f^\star)\delta(f-\phi+f^\star)\,+\\
&\quad+\zeta\zeta^*\int_{-\infty}^{+\infty} d\phi\;\; \mathcal{R}_k(\phi)\mathcal{R}_k(f-\phi)\;\; \delta(\phi-f^\star)\delta(f-\phi+f^\star)\,+\\
&\quad+\zeta^*\zeta\int_{-\infty}^{+\infty} d\phi\;\; \mathcal{R}_k(\phi)\mathcal{R}_k(f-\phi)\;\; \delta(\phi+f^\star)\delta(f-\phi-f^\star)
\end{aligned} \tag{E.28}$$

The first two integrals in the former equation are formally identical to the one in E.18 and thus evaluate both to zero. The last two integrals present the mixed products $\zeta\zeta^*$ and can be reduced to a sigle doubled integral with the substitution $\phi\to f-\phi$. In the following passages we also make use of the fact that $\mathrm{rect}_k(t)$ is a real and even function, and so $\mathcal{R}_k$ is also even and purely real.

$$\begin{aligned}
2\zeta\zeta^* \int_{-\infty}^{+\infty} d\phi \mathcal{R}_k(\phi)\mathcal{R}_k(f-\phi)\ \delta(\phi - f^\star)\delta(f-\phi+f^\star) &= \\
&= 2\zeta\zeta^*\mathcal{R}_k^2(f^\star) \int_{-\infty}^{+\infty} d\phi\ \ \delta(\phi - f^\star)\delta(f-\phi+f^\star) = \\
{\scriptstyle (\psi=\phi-f^\star)} \qquad &= \zeta\zeta^*\mathcal{R}_k^2(f^\star) \int_{-\infty}^{+\infty} d\phi\ \ \delta(\psi)\delta(f-\psi) = \\
&= 2\zeta\zeta^*\mathcal{R}_k^2(f^\star)\ \ (\delta \circledast \delta)(f) = \\
&= 2\zeta\zeta^*\mathcal{R}_k^2(f^\star)\ \ \delta(f)
\end{aligned} \tag{E.29}$$

It was used again the fact that δ is the neutral element for convolution. In this case equation E.16 gives:

$$\chi^2(k) = 2\zeta\zeta^*\mathcal{R}_k^2(f^\star) \int_0^T dt \int_{-\infty}^{+\infty} df\, e^{2\pi i t f}\delta(f) \tag{E.30}$$

This time the inverse Fourier transform evaluates to 1 (the antitrasform of $\delta(f)$) and the final result is:

$$\chi^2(k) = 2T\zeta\zeta^*\mathcal{R}_k^2(f^\star) \tag{E.31}$$

3. Generic *T* periodic real signal A generic real periodic signal with period T can be written as a sum of sinusoids (meaning both sine and cosine) with frequencies which are multiples of $1/T$. This corresponds in the Fourier domain to:

$$\mathcal{Z}(f) = \sum_{n=1}^{\infty} \zeta_n\delta(f - f_n^\star) + \zeta_n^*\delta(f + f_n^\star) \tag{E.32}$$

Where $f_n^\star = n/T$. We excluded $j = 0$ since $Z(t)$ was the residual signal, i.e. the signal minus its mean value, which is associated with the zeroth frequency Fourier component. Considering the last achievement for a single sinusoid we were tempted to state that in this case the result might be a combination of terms like the one in E.31; this proves in fact to be true, but recalling that $\chi^2[\mathcal{Z}]$ is nonlinear, we have first to prove that *interference terms* of the kind $\zeta_n\zeta_m$ or $\zeta_n\zeta_m^*$ with $m \neq n$ do annihilate themselves.

Inserting E.32 in E.16 results in a triple integral of a double summation, whose general term is very similar to E.28, exept for the ζ, ζ^* and $f^\star$ being replaced by different ζ_n, ζ_m, ζ_n^*, ζ_m^*, $f_n^\star$ and $f_m^\star$. If $m = n$ we fall back in the previous case and this ensures that at the end we will find a form such as:

$$\chi^2(k) = 2T\sum_{n=1}^{\infty} \zeta_n\zeta_n^*\mathcal{R}_k^2(f_n^\star) \quad + \quad \text{Interference} \tag{E.33}$$

We will prove now that interference terms are all null. The generic interference term is (analogous to E.28):

$$\begin{aligned}
\text{Interference term}_{n,m} \; = & \qquad\qquad\qquad\qquad (m \neq n) \\
= \zeta_n \zeta_m \int_{-\infty}^{+\infty} & d\phi \;\; \mathcal{R}_k(\phi)\mathcal{R}_k(f-\phi) \;\; \delta(\phi - f_n^\star)\delta(f-\phi-f_m^\star) \; + \\
+ \, \zeta_n^* \zeta_m^* \int_{-\infty}^{+\infty} & d\phi \;\; \mathcal{R}_k(\phi)\mathcal{R}_k(f-\phi) \;\; \delta(\phi + f_n^\star)\delta(f-\phi+f_m^\star) \; + \\
+ \, \zeta_n \zeta_m^* \int_{-\infty}^{+\infty} & d\phi \;\; \mathcal{R}_k(\phi)\mathcal{R}_k(f-\phi) \;\; \delta(\phi - f_n^\star)\delta(f-\phi+f_m^\star) \; + \\
+ \, \zeta_n^* \zeta_m \int_{-\infty}^{+\infty} & d\phi \;\; \mathcal{R}_k(\phi)\mathcal{R}_k(f-\phi) \;\; \delta(\phi + f_n^\star)\delta(f-\phi-f_m^\star)
\end{aligned} \tag{E.34}$$

Apart from the $\mathcal{R}_k$ functions, which are sampled by the delta and group up as $\mathcal{R}_k(f_n^\star)\mathcal{R}_k(f_m^\star)$, there are again two types of integral:

$$\int_{-\infty}^{+\infty} d\phi \;\; \delta(\phi - f_n^\star)\delta(f-\phi-f_m^\star) \tag{E.35}$$

$$\int_{-\infty}^{+\infty} d\phi \;\; \delta(\phi - f_n^\star)\delta(f-\phi+f_m^\star) \tag{E.36}$$

Both can be mapped by the substitution $\psi = \phi - f_n^\star$ into:

$$\int_{-\infty}^{+\infty} d\psi \;\; \delta(\psi)\delta(f-\psi-f_{n+m}^\star) \tag{E.37}$$

$$\int_{-\infty}^{+\infty} d\psi \;\; \delta(\psi)\delta(f-\psi-f_{n-m}^\star) \tag{E.38}$$

Where index algebra is possible since $f_n^\star = n/T$. These two integrals are the exploded forms of the convolutions:

$$\delta \circledast \delta_{f_{n+m}^\star} \;=\; \delta_{f_{n+m}^\star} \tag{E.39}$$

$$\delta \circledast \delta_{f_{n-m}^\star} \;=\; \delta_{f_{n-m}^\star} \tag{E.40}$$

Because $m \neq n$, both these delta give rise to non vanishing circular functions once inverse Fourier transformed, which are later cycled out to 0 by the unity period integral.

It has been proved that the χ^2 EFS curve for a periodic signal has the form:

$$\chi^2(k) \;=\; 2T \sum_{n=1}^{\infty} \zeta_n \zeta_n^* \mathcal{R}_k^2(f_n^\star) \tag{E.41}$$

As of equation 3.3, we first note that $\zeta_n \zeta_n^*$ is proportional to the n-th power spectrum component:

$$\zeta_n \zeta_n^* = P_n \tag{E.42}$$

The function $\mathcal{R}_k$ is not an unknown one: it can be proved by simple integration that it is:

$$\begin{aligned} \mathcal{R}_k(f) &= \frac{\sin(\pi f k)}{\pi f k} && \text{(E.43)} \\ &= \mathrm{sinc}(\pi f k) && \text{(E.44)} \end{aligned}$$

Thus we get:

$$\chi^2(k) = 2T \sum_{n=1}^{\infty} P_n \,\mathrm{sinc}^2(\pi f_n^{\star} k) \tag{E.45}$$

Which can be further reduced to:

$$\chi^2(k) = 2 \sum_{n=1}^{\infty} P_n \,\mathrm{sinc}^2\left(\frac{n\pi k}{T}\right) \tag{E.46}$$

That is, a combination of power-spectrum modulated sinc^2 functions. We shall now only replace k by its actual value $L/T\,\Delta T$:

$$\chi^2(\Delta T) = 2 \sum_{n=1}^{\infty} P_n \,\mathrm{sinc}^2\left(\frac{n\pi L \Delta T}{T^2}\right) \tag{E.47}$$

These two facts are notable:

1. If one power spectrum component is by far dominant, we recover expression E.31 and get a pure sinc^2 function.
2. As L increases, sinc^2 functions in E.47 get more and more narrowly peaked around $\Delta T = 0$, thus enabling a better resolution on the searched period.

In the real case, as L increases the period itself varies; if the shift developed by such variation reaches the phase bin size, we are rather convolving the LC with another sinc function, smoothing the EFS sinc^2 function. It is thus convenient to fold a suitable but not too much long observation to find the period in EFS procedures (see appendix D for details on maximum phasebins number and phase deviations during folding).

Finally, we recall that the above results are valid if and only if $\Delta T/T \ll 1$, such that the two periods can be confused in a single cycle integration, and also if bin fluctuations are all very similar and approximable by a constant.

Appendix F

Pulse template

The pulse profile used to fit folded lightcurves and determine the peak shift δ was created by modelling very accurate pulse data (high S/N ratio) obtained by IQUEYE with a set of 16 Lorentz curves. The parameters defining these functions are not used as fit parameters themselves, as this wouldn't give significant results. The resulting template is rather x- and y-translated (2 parameters) and y-scaled (1 parameter) to mach the folded lightcurve data.

Each Lorentz component has the form:

$$f_n(x) = d_n \cdot \frac{a_n^2}{a_n^2 + (x - h_n)^2} \tag{F.1}$$

The values for each component are given in table F.1. The template is built as:

$$f(x, x_1, z_1, k_1) = z_1 \left(\sum_{n=1}^{16} f_n(x - 0.3409 + x_1) \ + k_1 \right) \tag{F.2}$$

The constant translation 0.3409 is added in order to have x_1 as the main pulse maximum position. x_1, z_1 k_1 are used as free parameters during the fit.

№	d_n	a_n	h_n	№	d_n	a_n	h_n
1	1	0.0146996	0	9	0.1045030	0.0039061	-0.0040640
2	0.2175380	0.0146996	0.0295389	10	0.0094432	0.2093850	-0.0200141
3	0.1204380	0.0146996	0.0452724	11	-0.0088326	0.0630249	-0.2612050
4	-0.0322015	0.0156592	0.0948912	12	-0.0038865	0.0259154	-0.1534190
5	-0.0176647	0.0325165	0.1334170	13	0.0524991	0.0131649	-0.4084260
6	0.0128576	0.0531056	0.3555860	14	0.0462601	0.0517911	-0.4934550
7	0.3437950	0.0146996	0.0159706	15	0.2503360	0.0386609	-0.4007410
8	0.0274555	0.0146996	-0.0405742	16	0.0632930	0.0377745	-0.4453720

Table F.1: Parameters for the 16 Lorentz components building the pulse template.

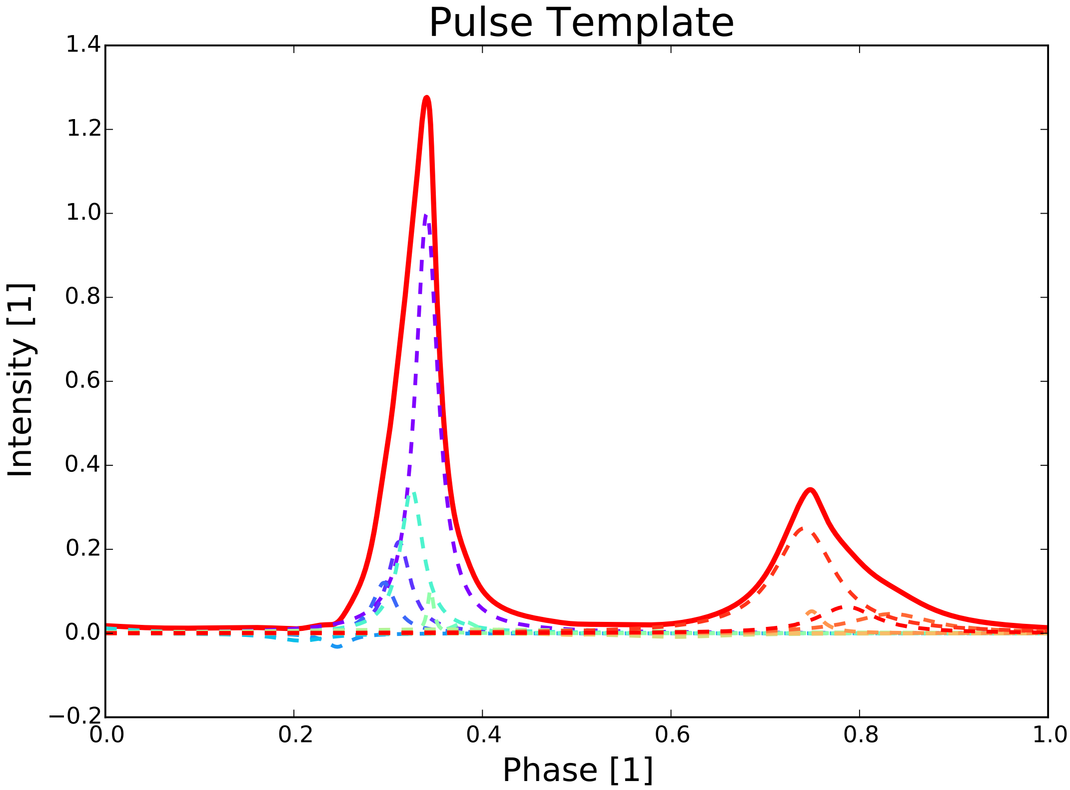

Figure F.1: The pulse template used for folded lightcurve fits (solid line), together with its 16 Lorentzian components (dashed).

Bibliography

[1] C. Barbieri, G. Naletto, T. Occhipinti, C. Facchinetti, E. Verroi, E. Giro, A. di Paola, S. Billotta, P. Zoccarato, P. Bolli, F. Tamburini, G. Bonanno, M. D'Onofrio, S. Marchi, G. Anzolin, I. Capraro, F. Messina, M. Belluso, C. Pernechele, M. Zaccariotto, L. Zampieri, V. da Deppo, S. Fornasier, and F. Pedichini. AquEYE, a single photon counting photometer for astronomy. *Journal of Modern Optics*, 56:261–272, January 2009.

[2] L. Zampieri, E. Verroi, G. Naletto, R. Mignani, C. Sigismondi, and C. Barbieri. Optical Observations of the Crab pulsar from March 2 through 4, 2013, with Aqueye at the Copernico telescope in Asiago (Cima Ekar Observatory). *The Astronomer's Telegram*, 4878:1, March 2013.

[3] L. Zampieri, G. Naletto, C. Barbieri, E. Verroi, M. Barbieri, G. Ceribella, M. D'Alessandro, G. Farisato, A. Di Paola, and P. Zoccarato. Aqueye+: a new ultrafast single photon counter for optical high time resolution astrophysics. In *Society of Photo-Optical Instrumentation Engineers (SPIE) Conference Series*, volume 9504 of *Society of Photo-Optical Instrumentation Engineers (SPIE) Conference Series*, May 2015.

[4] A. Messiah. *Quantum Mechanics*, volume 2. North-Holland Publishing Company, 1961.

[5] Pranab Ghosh. *Rotation and Accretion Powered Pulsars*. 10. World Sientific, 1 edition, 2007.

[6] N. Chamel, P. Haensel, J. L. Zdunik, and A. F. Fantina. On the Maximum Mass of Neutron Stars. *International Journal of Modern Physics E*, 22:30018, July 2013.

[7] P. B. Demorest, T. Pennucci, S. M. Ransom, M. S. E. Roberts, and J. W. T. Hessels. A two-solar-mass neutron star measured using Shapiro delay. *Nature*, 467:1081–1083, October 2010.

[8] J. Antoniadis, P. C. C. Freire, N. Wex, T. M. Tauris, R. S. Lynch, M. H. van Kerkwijk, M. Kramer, C. Bassa, V. S. Dhillon, T. Driebe, J. W. T. Hessels, V. M. Kaspi, V. I. Kondratiev, N. Langer, T. R. Marsh, M. A. McLaughlin, T. T. Pennucci, S. M.

Ransom, I. H. Stairs, J. van Leeuwen, J. P. W. Verbiest, and D. G. Whelan. A Massive Pulsar in a Compact Relativistic Binary. *Science*, 340:448, April 2013.

[9] LHCb Collaboration. Observation of $j/\psi p$ resonances consistent with pentaquark states in $\Lambda_b^0 \to j/\psi K^- p$ decays. *Phys. Rev. Lett.*, 115:072001, Aug 2015.

[10] Marco Velli Claudio Chiuderi. *Fisica del Plasma*. Springer, 1 edition, 2012.

[11] F. Pacini. Energy Emission from a Neutron Star. *Nature*, 216:567–568, November 1967.

[12] T. Gold. Rotating Neutron Stars as the Origin of the Pulsating Radio Sources. *Nature*, 218:731–732, May 1968.

[13] T. Gold. Rotating Neutron Stars and the Nature of Pulsars. *Nature*, 221:25–27, January 1969.

[14] P. Goldreich and W. H. Julian. Pulsar Electrodynamics. *Astrophysical Journal*, 157:869, August 1969.

[15] A. G. Lyne and R. N. Manchester. The shape of pulsar radio beams. *MNRAS*, 234:477–508, October 1988.

[16] A. Shearer and A. Golden. Why study pulsars optically? In W. Becker, H. Lesch, and J. Trümper, editors, *Neutron Stars, Pulsars, and Supernova Remnants*, page 44, 2002.

[17] R. P. Mignani. Multi-Wavelength Observations of Pulsars. In W. Lewandowski, O. Maron, and J. Kijak, editors, *Electromagnetic Radiation from Pulsars and Magnetars*, volume 466 of *Astronomical Society of the Pacific Conference Series*, page 3, December 2012.

[18] M. A. Livingstone, V. M. Kaspi, F. P. Gavriil, R. N. Manchester, E. V. G. Gotthelf, and L. Kuiper. New phase-coherent measurements of pulsar braking indices. *Astrophysics and Space Science*, 308:317–323, April 2007.

[19] F. C. Michel and W. H. Tucker. Pulsar-emission mechanisms. *Publications of the Astronomical Society of the Pacific*, 81:547, October 1969.

[20] R. N. Manchester, G. B. Hobbs, A. Teoh, and M. Hobbs. The Australia Telescope National Facility Pulsar Catalogue. *Publications of the Astronomical Society of the Pacific*, 129:1993–2006, April 2005.

[21] J. Aleksić, S. Ansoldi, L. A. Antonelli, P. Antoranz, A. Babic, P. Bangale, J. A. Barrio, J. Becerra González, W. Bednarek, E. Bernardini, B. Biasuzzi, A. Biland, O. Blanch, S. Bonnefoy, G. Bonnoli, F. Borracci, T. Bretz, E. Carmona, A. Carosi, P. Colin, E. Colombo, J. L. Contreras, J. Cortina, S. Covino, P. Da Vela, F. Dazzi, A. De Angelis, G. De Caneva, B. De Lotto, E. de Oña Wilhelmi, C. Delgado Mendez, M. Doert,

D. Dominis Prester, D. Dorner, M. Doro, S. Einecke, D. Eisenacher, D. Elsaesser, M. V. Fonseca, L. Font, K. Frantzen, C. Fruck, D. Galindo, R. J. García López, M. Garczarczyk, D. Garrido Terrats, M. Gaug, N. Godinović, A. González Muñoz, S. R. Gozzini, D. Hadasch, Y. Hanabata, M. Hayashida, J. Herrera, D. Hildebrand, J. Hose, D. Hrupec, W. Idec, V. Kadenius, H. Kellermann, K. Kodani, Y. Konno, J. Krause, H. Kubo, J. Kushida, A. La Barbera, D. Lelas, N. Lewandowska, E. Lindfors, S. Lombardi, M. López, R. López-Coto, A. López-Oramas, E. Lorenz, I. Lozano, M. Makariev, K. Mallot, G. Maneva, N. Mankuzhiyil, K. Mannheim, L. Maraschi, B. Marcote, M. Mariotti, M. Martínez, D. Mazin, U. Menzel, J. M. Miranda, R. Mirzoyan, A. Moralejo, P. Munar-Adrover, D. Nakajima, A. Niedzwiecki, K. Nilsson, K. Nishijima, K. Noda, N. Nowak, R. Orito, A. Overkemping, S. Paiano, M. Palatiello, D. Paneque, R. Paoletti, J. M. Paredes, X. Paredes-Fortuny, M. Persic, P. G. Prada Moroni, E. Prandini, S. Preziuso, I. Puljak, R. Reinthal, W. Rhode, M. Ribó, J. Rico, J. Rodriguez Garcia, S. Rügamer, A. Saggion, T. Saito, K. Saito, K. Satalecka, V. Scalzotto, V. Scapin, C. Schultz, T. Schweizer, S. N. Shore, A. Sillanpää, J. Sitarek, I. Snidaric, D. Sobczynska, F. Spanier, V. Stamatescu, A. Stamerra, T. Steinbring, J. Storz, M. Strzys, L. Takalo, H. Takami, F. Tavecchio, P. Temnikov, T. Terzić, D. Tescaro, M. Teshima, J. Thaele, O. Tibolla, D. F. Torres, T. Toyama, A. Treves, M. Uellenbeck, P. Vogler, R. M. Wagner, R. Zanin, D. Horns, J. Martín, and M. Meyer. Measurement of the Crab Nebula spectrum over three decades in energy with the MAGIC telescopes. *Journal of High Energy Astrophysics*, 5:30–38, March 2015.

[22] A. Shearer, B. Stappers, P. O'Connor, A. Golden, R. Strom, M. Redfern, and O. Ryan. Enhanced Optical Emission During Crab Giant Radio Pulses. *Science*, 301:493–495, July 2003.

[23] C. Germanà, L. Zampieri, C. Barbieri, G. Naletto, A. Čadež, M. Calvani, M. Barbieri, I. Capraro, A. Di Paola, C. Facchinetti, T. Occhipinti, A. Possenti, D. Ponikvar, E. Verroi, and P. Zoccarato. Aqueye optical observations of the Crab Nebula pulsar. *Astronomy and Astrophysics*, 548:A47, December 2012.

[24] L. Zampieri, A. Čadež, C. Barbieri, G. Naletto, M. Calvani, M. Barbieri, E. Verroi, P. Zoccarato, and T. Occhipinti. Optical phase coherent timing of the Crab nebula pulsar with Iqueye at the ESO New Technology Telescope. *MNRAS*, 439:2813–2821, April 2014.

[25] C. Barbieri, G. Naletto, L. Zampieri, E. Verroi, S. Gradari, S. Collins, and A. Shearer. Aqueye and Iqueye, Very-High-Time-Resolution Photon-Counting Photometers. In E. Griffin, R. Hanisch, and R. Seaman, editors, *IAU Symposium*, volume 285 of *IAU Symposium*, pages 280–282, April 2012.

[26] G. Naletto, C. Barbieri, T. Occhipinti, F. Tamburini, S. Billotta, S. Cocuzza, and D. Dravins. Very fast photon counting photometers for astronomical applications: from QuantEYE to AquEYE. In *Society of Photo-Optical Instrumentation Engineers*

(SPIE) Conference Series, volume 6583 of *Society of Photo-Optical Instrumentation Engineers (SPIE) Conference Series*, page 0, May 2007.

[27] C. Barbieri, T. Occhipinti, P. Zoccarato, C. Facchinetti, G. Naletto, E. Verroi, M. Zaccariotto, E. Giro, P. Bolli, G. Bonanno, A. di Paola, C. Pernechele, G. Anzolin, and F. Tamburini. First Results of AQUEYE, a Precursor Ultra Fast Photometer for the E-ELT. In *JENAM-2007, "Our Non-Stable Universe"*, pages 87–87, August 2007.

[28] C. Germanà, L. Zampieri, I. Capraro, C. Facchinetti, G. Naletto, T. Occhipinti, E. Verroi, P. Zoccarato, and C. Barbieri. Optical pulsations of the Crab Nebula pulsar with AquEYE. In *Polarimetry days in Rome: Crab status, theory and prospects*, page 31, 2008.

[29] G. Naletto, C. Barbieri, T. Occhipinti, I. Capraro, A. di Paola, C. Facchinetti, E. Verroi, P. Zoccarato, G. Anzolin, M. Belluso, S. Billotta, P. Bolli, G. Bonanno, V. da Deppo, S. Fornasier, C. Germanà, E. Giro, S. Marchi, F. Messina, C. Pernechele, F. Tamburini, M. Zaccariotto, and L. Zampieri. Iqueye, a single photon-counting photometer applied to the ESO new technology telescope. *Astronomy and Astrophysics*, 508:531–539, December 2009.

[30] G. B. Hobbs, R. T. Edwards, and R. N. Manchester. TEMPO2, a new pulsar-timing package - I. An overview. *MNRAS*, 369:655–672, June 2006.

[31] R. T. Edwards, G. B. Hobbs, and R. N. Manchester. TEMPO2, a new pulsar timing package - II. The timing model and precision estimates. *MNRAS*, 372:1549–1574, November 2006.

[32] G. Hobbs, R. Edwards, and R. Manchester. TEMPO2: a New Pulsar Timing Package. *Chinese Journal of Astronomy and Astrophysics Supplement*, 6(2):189–192, December 2006.

[33] R. W. Hellings. Relativistic effects in astronomical timing measurements. *The Astronomical Journal*, 91:650–659, March 1986.

[34] Leahy et al. On searches for pulsed emission with application to four globular cluster x-ray sources: NGC 1851, 6441, 6624, and 6712. *The Astrophysical Journal*, 266:160–170, March 2015.

[35] A. G. Lyne, R. S. Pritchard, and F. Graham-Smith. Twenty-Three Years of Crab Pulsar Rotational History. *MNRAS*, 265:1003, December 1993.

[36] A. G. Lyne, C. A. Jordan, F. Graham-Smith, C. M. Espinoza, B. W. Stappers, and P. Weltevrede. 45 years of rotation of the Crab pulsar. *MNRAS*, 446:857–864, January 2015.

[37] T. Oosterbroek, J. H. J. de Bruijne, D. Martin, P. Verhoeve, M. A. C. Perryman, C. Erd, and R. Schulz. Absolute timing of the Crab Pulsar at optical wavelengths

with superconducting tunneling junctions. *Astronomy and Astrophysics*, 456:283–286, September 2006.

[38] T. Oosterbroek, I. Cognard, A. Golden, P. Verhoeve, D. D. E. Martin, C. Erd, R. Schulz, J. A. Stüwe, A. Stankov, and T. Ho. Simultaneous absolute timing of the Crab pulsar at radio and optical wavelengths. *Astronomy and Astrophysics*, 488:271–277, September 2008.

[39] C. Germanà, L. Zampieri, I. Capraro, C. Facchinetti, G. Naletto, T. Occhipinti, E. Verroi, P. Zoccarato, and C. Barbieri. Crab Pulsar Observations with AquEYE. In J. Rodriguez and P. Ferrando, editors, *American Institute of Physics Conference Series*, volume 1126 of *American Institute of Physics Conference Series*, pages 370–372, May 2009.

[40] L. Zampieri, C. Germanà, C. Barbieri, G. Naletto, A. Čadež, I. Capraro, A. di Paola, C. Facchinetti, T. Occhipinti, D. Ponikvar, E. Verroi, and P. Zoccarato. The Crab pulsar seen with AquEYE at Asiago Cima Ekar observatory. *Advances in Space Research*, 47:365–369, January 2011.

[41] A. Shearer, S. Collins, G. Naletto, C. Barbieri, L. Zampieri, C. Germana, S. Gradari, E. Verroi, and B. Stappers. High-Time-Resolution Optical Observations of the Crab Pulsar. In W. Lewandowski, O. Maron, and J. Kijak, editors, *Electromagnetic Radiation from Pulsars and Magnetars*, volume 466 of *Astronomical Society of the Pacific Conference Series*, page 11, December 2012.

[42] A. H. Rots, K. Jahoda, and A. G. Lyne. Absolute Timing of the Crab Pulsar with the Rossi X-Ray Timing Explorer. *The Astrophysical Journal*, 605:L129–L132, April 2004.

[43] A. A. Abdo, M. Ackermann, M. Ajello, W. B. Atwood, M. Axelsson, L. Baldini, J. Ballet, G. Barbiellini, M. G. Baring, D. Bastieri, K. Bechtol, R. Bellazzini, B. Berenji, R. D. Blandford, E. D. Bloom, E. Bonamente, A. W. Borgland, J. Bregeon, A. Brez, M. Brigida, P. Bruel, T. H. Burnett, G. A. Caliandro, R. A. Cameron, F. Camilo, P. A. Caraveo, J. M. Casandjian, C. Cecchi, Ö. Çelik, A. Chekhtman, C. C. Cheung, J. Chiang, S. Ciprini, R. Claus, I. Cognard, J. Cohen-Tanugi, L. R. Cominsky, J. Conrad, C. D. Dermer, A. de Angelis, A. de Luca, F. de Palma, S. W. Digel, E. d. C. e. Silva, P. S. Drell, R. Dubois, D. Dumora, C. Espinoza, C. Farnier, C. Favuzzi, S. J. Fegan, E. C. Ferrara, W. B. Focke, M. Frailis, P. C. C. Freire, Y. Fukazawa, S. Funk, P. Fusco, F. Gargano, D. Gasparrini, N. Gehrels, S. Germani, G. Giavitto, B. Giebels, N. Giglietto, F. Giordano, T. Glanzman, G. Godfrey, I. A. Grenier, M.-H. Grondin, J. E. Grove, L. Guillemot, S. Guiriec, Y. Hanabata, A. K. Harding, M. Hayashida, E. Hays, R. E. Hughes, G. Jóhannesson, A. S. Johnson, R. P. Johnson, T. J. Johnson, W. N. Johnson, S. Johnston, T. Kamae, H. Katagiri, J. Kataoka, N. Kawai, M. Kerr, J. Knödlseder, M. L. Kocian, M. Kramer, F. Kuehn, M. Kuss, J. Lande, L. Latronico, S.-H. Lee, M. Lemoine-Goumard, F. Longo, F. Loparco, B. Lott, M. N. Lovellette, P. Lubrano, A. G. Lyne, A. Makeev, M. Marelli, M. N. Mazziotta, J. E. McEnery,

C. Meurer, P. F. Michelson, W. Mitthumsiri, T. Mizuno, A. A. Moiseev, C. Monte, M. E. Monzani, E. Moretti, A. Morselli, I. V. Moskalenko, S. Murgia, T. Nakamori, P. L. Nolan, J. P. Norris, A. Noutsos, E. Nuss, T. Ohsugi, N. Omodei, E. Orlando, J. F. Ormes, M. Ozaki, D. Paneque, J. H. Panetta, D. Parent, V. Pelassa, M. Pepe, M. Pesce-Rollins, M. Pierbattista, F. Piron, T. A. Porter, S. Rainò, R. Rando, P. S. Ray, M. Razzano, A. Reimer, O. Reimer, T. Reposeur, S. Ritz, L. S. Rochester, A. Y. Rodriguez, R. W. Romani, M. Roth, F. Ryde, H. F.-W. Sadrozinski, D. Sanchez, A. Sander, P. M. Saz Parkinson, J. D. Scargle, C. Sgrò, E. J. Siskind, D. A. Smith, P. D. Smith, G. Spandre, P. Spinelli, B. W. Stappers, M. S. Strickman, D. J. Suson, H. Tajima, H. Takahashi, T. Tanaka, J. B. Thayer, J. G. Thayer, G. Theureau, D. J. Thompson, S. E. Thorsett, L. Tibaldo, D. F. Torres, G. Tosti, A. Tramacere, Y. Uchiyama, T. L. Usher, A. Van Etten, V. Vasileiou, N. Vilchez, V. Vitale, A. P. Waite, E. Wallace, P. Wang, K. Watters, P. Weltevrede, B. L. Winer, K. S. Wood, T. Ylinen, and M. Ziegler. Fermi Large Area Telescope Observations of the Crab Pulsar And Nebula. *The Astrophysical Journal*, 708:1254–1267, January 2010.

[44] Matteo Frigo and Steven G. Johnson. The design and implementation of FFTW3. *Proceedings of the IEEE*, 93(2):216–231, 2005. Special issue on "Program Generation, Optimization, and Platform Adaptation".